Proteomic and functional mapping of cardiac NaV1.5 channel phosphorylation reveals multisite regulation of surface expression and gating

Maxime Lorenzini, Sophie Burel, Adrien Lesage, Emily Wagner, Camille Charrière, Pierre-Marie Chevillard, Bérangère Evrard, Dan Maloney, Kiersten M Ruff, Rohit Pappu, et al.

Proteomic and functional mapping of cardiac $Na_V1.5$ channel phosphorylation reveals multisite regulation of surface expression and gating

Maxime Lorenzini[a], Sophie Burel[a], Adrien Lesage[a], Emily Wagner[b], Camille Charrière[a], Pierre-Marie Chevillard[a], Bérangère Evrard[a], Dan Maloney[c], Kiersten M. Ruff[b], Rohit V. Pappu[b], Stefan Wagner[d], Jeanne M. Nerbonne[e,f], Jonathan R. Silva[b], R. Reid Townsend[f,g], Lars S. Maier[d] and Céline Marionneau[a†]

[a]Université de Nantes, CNRS, INSERM, l'institut du thorax, F-44000 Nantes, France; [b]Department of Biomedical Engineering, Washington University in Saint Louis, MO, USA; [c]Bioinformatics Solutions Inc., Waterloo, ON, Canada; [d]Department of Internal Medicine II, University Heart Center, University Hospital Regensburg, Regensburg, Germany; Departments of [e]Developmental Biology, [f]Medicine and [g]Cell Biology and Physiology, Washington University Medical School, Saint Louis, MO, USA.

[†]**Correspondence to:** Céline Marionneau, l'institut du thorax, INSERM UMR1087, CNRS UMR6291, IRS-Université de Nantes, 8 Quai Moncousu, BP 70721, 44007 Nantes Cedex 1, France, Tel: +33 2 28 08 01 63, Email: celine.marionneau@univ-nantes.fr

Running Title: Proteomic and functional mapping of cardiac $Na_V1.5$ channel phosphorylation

Abstract

Phosphorylation of $Na_V1.5$ channels regulates cardiac excitability, yet the phosphorylation sites regulating channel function and the underlying mechanisms remain largely unknown. Using a systematic quantitative phosphoproteomic approach, we analyzed $Na_V1.5$ channel complexes purified from non-failing and failing mouse left ventricles, and we identified 42 phosphorylation sites on $Na_V1.5$. Most sites are clustered, and three of these clusters are highly phosphorylated. Analyses of phosphosilent and phosphomimetic $Na_V1.5$ mutants revealed the roles of three phosphosites in regulating $Na_V1.5$ channel expression and gating. The phosphorylated serines-664 and -667 regulate the voltage-dependence of channel activation in a cumulative manner, whereas phosphorylation of the nearby serine-671, which is increased in failing hearts, decreases cell surface $Na_V1.5$ expression and peak Na^+ current. No additional roles could be assigned to the other clusters of phosphosites. Taken together, the results demonstrate that ventricular $Na_V1.5$ is highly phosphorylated, and that the phosphorylation-dependent regulation of $Na_V1.5$-encoded channels is highly complex, site-specific and dynamic.

Keywords: Cardiac $Na_V1.5$ channels; phosphoproteomics, native phosphorylation sites; phosphorylation clusters; heart failure

Abbreviations: A, alanine; E, glutamate; HEK-293, Human Embryonic Kidney 293 cells; I_{Na}, peak Na^+ current; I_{NaL}, late Na^+ current; IP, immunoprecipitation; mαNa_VPAN, anti-Na_V channel subunit mouse monoclonal antibody; MS, Mass Spectrometry; MS1, mass spectrum of peptide precursors; MS2 or MS/MS, fragmentation mass spectrum of peptides selected in narrow mass range (2 Da) from MS1 scan; Na_V, voltage-gated Na^+ channel; pS, phosphoserine; pT, phosphothreonine; S, serine; T, threonine; TAC, Transverse Aortic Constriction; TMT, Tandem Mass Tag.

Introduction

Voltage-gated Na^+ (Na_V) channels are key determinants of myocardial excitability, and defects in Na_V channel expression or functioning in the context of inherited or acquired cardiac disease increase propensity to develop lethal arrhythmias (1). Ventricular Na_V channels, composed primarily of the $Na_V1.5$ channel pore-forming subunit, in association with several accessory/regulatory proteins, generate the transient, peak Na^+ current (I_{Na}) responsible for the action potential upstroke and rapid intercellular conduction. While cardiac myocyte Na_V channels inactivate quickly, there is a finite probability (~0.5%) of channels remaining open, resulting in the late component of the Na^+ current (I_{NaL}), which contributes to determining action potential duration. In the ventricular myocardium, the $Na_V1.5$ protein is subject to many post-translational modifications, each of which fine-tunes channel expression and functioning in various physiological and disease contexts. Among the eleven different post-translational modifications previously shown to regulate cardiac $Na_V1.5$ channels, phosphorylation at serine, threonine and tyrosine residues is certainly the best characterized (reviewed in (2), (3-5)).

A role for phosphorylation in regulating cardiac $Na_V1.5$ channels was first suggested in a pioneering study demonstrating that β-adrenergic receptors couple to Na_V channels not only through a direct G-protein pathway, but also through an indirect, Protein Kinase A (PKA)-dependent pathway (6). The involvement of several additional kinases and phosphatases in regulating both I_{Na} and/or I_{NaL} later spotlighted the functional relevance of cardiac $Na_V1.5$ channel phosphorylation. Perhaps most strikingly, progress in mass spectrometry (MS)-based phosphoproteomic analyses recently buttressed the field by revealing the existence of multiple phosphorylation sites on native ventricular (7,8) and heterologously-expressed (9) $Na_V1.5$ channels. Yet, little is known about the roles and detailed molecular mechanisms that underlie phosphorylation-dependent regulations of cardiac $Na_V1.5$ channels.

Phosphorylation of $Na_V1.5$ channels has also recently been suggested as an arrhythmogenic mechanism in heart failure (10-15). The Na_V channel defects associated with heart failure are most often characterized by increased I_{NaL} and/or decreased I_{Na}, contributing to action potential prolongation and conduction slowing, respectively (10,14,16-19). The increase in I_{NaL} has reportedly been linked to the activation of kinases, mainly the Ca^{2+}/Calmodulin-dependent protein Kinase II (CaMKII) (10,13-15), and several studies have focused on identifying the CaMKII-dependent $Na_V1.5$ phosphorylation sites (7,9,20,21). Notably, increased CaMKII-dependent $Na_V1.5$ phosphorylation at serine-571 has been reported and suggested to increase I_{NaL} in non-ischemic human heart failure (12) and in animal models of heart disease (11,12,14). Nevertheless, $Na_V1.5$ channel phosphorylation may not be the sole mechanism involved in the observed pathophysiological defects, as other evidence suggests roles for upregulation of the neuronal $Na_V1.1$ (18,22), $Na_V1.6$ (18) or $Na_V1.8$ (23) channels. Intensive investigations were also undertaken to understand the causes of the reduced I_{Na}, yet the detailed underlying molecular mechanisms remain unclear. While most studies failed to detect any changes in $Na_V1.5$ transcript or total protein expression in failing human hearts (24) or in animal models of heart failure (17,19), several mechanisms have been suggested to contribute to reduced I_{Na}, including the generation of a C-terminal truncation splicing variant switch in $Na_V1.5$ transcripts (25,26), elevated NADH and reactive oxygen species production (27), or increased intracellular Ca^{2+} concentration and subsequent increased expression of the E3 ubiquitin ligase Nedd4-2 (28). In line with reduced I_{Na}, a recent study using high-resolution imaging and functional techniques showed a reduction in $Na_V1.5$ cluster size and a corresponding decreased number of open channels at the lateral membranes of ventricular myocytes from mice subjected to Transverse Aortic Constriction (TAC), without any changes in $Na_V1.5$ transcript or total protein expression (29).

In this study, we investigated the patterns of phosphorylation of native mouse left ventricular $Na_V1.5$ channels and the roles of identified phosphorylation sites in regulating $Na_V1.5$ channel expression and functioning. Using quantitative MS-based phosphoproteomic analyses, we identified and quantified *in situ* the native phosphorylation sites of the $Na_V1.5$ in a mouse model of pressure overload-induced heart failure produced by TAC. By analyzing the expression and the functional properties of phosphosilent and phosphomimetic $Na_V1.5$ mutant channels in human embryonic kidney (HEK-293)

cells, as well as simulating the consequences of phosphorylation on $Na_V1.5$ peptide segment expansion, we identified phosphorylation hot spots for regulation of both channel cell surface expression and gating.

Results

Purification and characterization of Na_V channel complexes from Sham and TAC mouse left ventricles

Na_V channel complexes from four Sham-operated and five TAC mouse left ventricles were purified by immunoprecipitation (IP) using an anti-Na_VPAN mouse monoclonal (mαNa_VPAN) antibody, and characterized using the quantitative isobaric tandem mass tag (TMT)-based analysis. As illustrated in **Figure 1 - Table Supplement 1**, and consistent with previous findings (14), the echocardiographic analysis confirmed increased left ventricular masses (LVM/BW ratios), reduced ejection fractions, but unaltered left ventricular end-diastolic diameters (LVID;d) five weeks after the TAC surgery, demonstrating left ventricular concentric hypertrophy and systolic contractile dysfunction or heart failure in the TAC animals. Western blot analyses of total lysates showed similar total $Na_V1.5$ protein expression in Sham and TAC left ventricles, which resulted in similar $Na_V1.5$ immunoprecipitation yields in the nine samples (**Figure 1 - Figure Supplement 1A**). Isolated Na_V channel complexes were then digested with trypsin, and peptide mixtures were labeled with different TMT tags and combined in the same TMT set for multiplexed MS/MS analysis. As illustrated in **Table 1**, the $Na_V1.5$ protein was the most represented protein in the mαNa_VPAN-IPs, with 310 unique and $Na_V1.5$-specific peptides identified and 56% amino acid sequence coverage (70% with the transmembrane domains removed, **Figure 2**).

Consistent with the homogenous yields in the $Na_V1.5$ immunoprecipitation, the relative abundance of the $Na_V1.5$ peptides detected by MS in the nine samples was similar, and used for normalization of each single protein and peptide abundance (**Figure 1 - Figure Supplement 1B**). Accordingly, the distribution of normalized abundance ratios of $Na_V1.5$ peptides (in $\log_2$) in TAC, *versus* Sham, mαNa_VPAN-IPs was centered on zero (**Figure 1 - Figure Supplement 1C**). Altogether, therefore, these observations attest to a high reproducibility across biological replicates, and a low technical variability inherent to experimental procedures. Of note, and as described previously (30), two $Na_V1.5$ peptides differing by the presence or absence of a glutamine (Q) at position-1080 were detected (**Table 1 & Figure 2**), reflecting the expression of at least two distinct $Na_V1.5$ splice variants in mouse left ventricles; Q1080del corresponding to the commonly reported hH1C variant. Interestingly, these analyses also allowed the identification of eight additional Na_V channel pore-forming subunits, among which $Na_V1.4$ is the most abundant, with 86 unique $Na_V1.4$-specific peptides detected (**Table 1**). In addition, several previously identified $Na_V1.5$ channel associated/regulatory proteins, including calmodulin, the VY variant of Fibroblast growth factor Homologous Factor 2 (FHF2-VY) and ankyrin-G, were detected, with no significant differences in abundance between Sham and TAC mαNa_VPAN-IPs (**Table 1**).

Identification and quantification of 42 $Na_V1.5$ phosphorylation sites in Sham and TAC mouse left ventricles

The phosphoproteomic analysis of the mαNa_VPAN-IPs from Sham and TAC mouse left ventricles allowed the unambiguous identification of 42 native phosphorylation sites in the $Na_V1.5$ protein, 22 of which have never, to our knowledge, been previously described in native cardiac tissues (**Figures 1A** & **2**). **Table 2** lists the phosphopeptides enabling the best phosphorylation site assignment(s) for each phosphorylation site; and corresponding MS/MS spectra are presented in **Table 2 - Figure Supplement 1**. Interestingly, the vast majority of these phosphorylation sites are clustered, with the first intracellular linker loop of $Na_V1.5$ revealed as a hot spot for phosphorylation, with a total of 21 sites identified. Further label-free quantitative analysis of the areas of extracted MS1 peptide ion chromatograms revealed large differences in the relative abundances of the individual phosphopeptides, and the existence of three highly phosphorylated clusters at positions S457 to S460, S483 to T486, and S664 to S671 (**Figure 1B**). In addition, and in contrast to the other phosphorylation sites, the phosphorylated peptides assigning these three phosphorylation clusters are more abundant than their non-phosphorylated counterparts, suggesting that these sites are mostly phosphorylated in native $Na_V1.5$ channels in wild-type mouse left ventricles. Looking into the detailed quantification of single

phosphorylation sites inside each of these clusters, however, major differences in phosphopeptide abundance are evident (**Figure 1 - Figure Supplement 2**). This is the case, for example, of phosphorylation at S664 or S667, which is about 10-fold more abundant than at residues T670 or S671.

To determine whether phosphorylation of $Na_V1.5$ is regulated in heart failure, the relative abundance of each $Na_V1.5$ phosphopeptide in TAC, *versus* Sham, mαNa_VPAN-IPs was calculated using the relative abundance of TMT reporter ions. As illustrated in **Figure 1C**, peptides exhibiting phosphorylation(s) on serine-671 (S671) alone or in combination with serines-664 (S664 + S671) or -667 (S667 + S671) are significantly more abundant in the TAC, compared with the Sham, mαNa_VPAN-IPs. The relative abundances of their non-phosphorylated counterparts, however, are similar in Sham and TAC mαNa_VPAN-IPs (data not shown). Additionally, none of the other $Na_V1.5$ phosphopeptides showed any significant differences in the Sham and TAC mαNa_VPAN-IPs (**Table 2**). In addition to $Na_V1.5$, four phosphorylation sites on $Na_V1.4$ and one on $Na_V1.3$ could also be detected (**Table 2 - Table Supplement 1 & Figure Supplement 1**). Taken together, these quantitative phosphoproteomic analyses identified 42 native phosphorylation sites on $Na_V1.5$, among which three clusters of phosphorylation in the first loop of the channel are highly phosphorylated, and one serine at position-671 shows increased phosphorylation in TAC left ventricles.

Functional mapping of $Na_V1.5$ channel phosphorylation clusters

The identification of several clusters of phosphorylation sites on $Na_V1.5$ suggests that these sites may be involved in the coordinated regulation of channel expression and/or function. Out of the eight clusters of phosphorylation identified in the mouse $Na_V1.5$ protein, seven are conserved in the human $Na_V1.5$ protein sequence; only the mouse T1105 is not conserved (**Figure 3 - Figure Supplement 1**). In order to investigate the functional roles of these (seven) phosphorylation clusters, phosphosilent and phosphomimetic $Na_V1.5$ channel constructs in the human $Na_V1.5$ hH1C cDNA sequence were generated, transiently expressed in HEK-293 cells, and characterized in whole-cell voltage-clamp recordings. In the phosphosilent constructs, mutations were introduced to replace serines/threonines with alanines, whereas in the phosphomimetic constructs, mutations were introduced to substitute glutamates for serines/threonines, to mimic phosphorylation.

As illustrated in **Figure 3B**, these whole-cell voltage-clamp analyses demonstrated that the voltage-dependence of activation of $Na_V1.5$-S664-671A phosphosilent channels is significantly ($p<0.001$) shifted towards depolarized potentials, compared to WT channels (see distributions, detailed properties and statistics in **Figure 3 - Figure Supplement 2A & Table Supplement 1**). The activation curve of the $Na_V1.5$-S664-671E phosphomimetic channel was also significantly ($p<0.001$) shifted, although to a lesser extent, when compared with the phosphosilent channel. Together, therefore, these findings suggest that the S664-671 cluster is phosphorylated in HEK-293 cells, and that disruption of phosphorylation at these sites shifts the voltage-dependence of channel activation towards depolarized potentials. In addition, the time to peak Na^+ current (**Figure 3D**), as well as the inactivation time constants, τ_{fast} and τ_{slow} (**Figures 3E & 3F**), were shifted towards depolarized potentials until reaching full activation at ~0 mV. The peak Na^+ current density of the $Na_V1.5$-S664-671E phosphomimetic channel was significantly ($p<0.05$) reduced compared to the WT channel, whereas no significant changes were observed with the $Na_V1.5$-S664-671A phosphosilent channel (**Figure 3C,** see distributions at -20 mV and statistics in **Figure 3 - Figure Supplement 2B & Table Supplement 1**). In contrast, the voltage-dependence of steady-state inactivation (**Figure 3B**) and the kinetic of recovery from inactivation (**Figure 3 - Figure Supplement 2D & Table Supplement 1**) of both S664-671 phosphomutant channels were not changed. Additionally, and to our surprise, no differences in current densities, or in the kinetics or voltage-dependences of current activation and inactivation, or in the kinetics of recovery from inactivation were observed for any of the six other heterologously-expressed (in HEK-293 cells) paired phosphosilent or phosphomimetic $Na_V1.5$ channels (**Figure 3 - Figure Supplement 2 & Table Supplement 1**). Taken together, therefore, these analyses revealed a key role for phosphorylation at S664-671 in regulating the voltage-dependence of $Na_V1.5$

channel activation and peak Na^+ current density, whereas regulation mediated by the other phosphorylation sites investigated most likely involve more complex mechanisms.

Phosphorylation at S664 and S667 shifts the voltage-dependence of current activation towards hyperpolarized potentials whereas phosphorylation at S671 decreases the peak Na^+ current density

To decipher the respective contributions of the S664, S667, T670 and S671 phosphorylation sites in regulating the voltage-dependence of current activation and peak Na^+ current density, each of these serines/threonine was mutated individually to alanine or glutamate, and the densities and properties of Na^+ currents from single phosphosilent or phosphomimetic channels were examined in transiently transfected HEK-293 cells. These analyses showed that the voltage-dependences of activation of the $Na_V1.5$-S664 (**Figure 4A**) and $Na_V1.5$-S667 (**Figure 4B**) phosphomutant channels are significantly ($p<0.001$) shifted towards depolarized potentials, compared to the WT channels, whereas no changes were observed with the $Na_V1.5$-T670 or $Na_V1.5$-S671 phosphomutant channels (**Figures 4C & 4D**, see detailed properties and statistics in **Figure 4 - Table Supplement 1**). Of note, the ~6 mV shifts observed with the single $Na_V1.5$-S664 and $Na_V1.5$-S667 phosphomutant channels were two-fold smaller than the ~10 mV shift obtained with the quadruple $Na_V1.5$-S664-671A phosphosilent channel, suggesting that the effects at S664 and S667 are additive. Additionally, these analyses revealed that sole the $Na_V1.5$-S671E phosphomimetic channel shows a significant ($p<0.05$) decrease in peak Na^+ current density (**Figure 4H**), whereas none of the other single phosphomutant channels showed any significant differences (**Figures 4E, 4F & 4G**).

Because phosphorylation at S671 was found to be increased in the TAC, compared with the Sham, mαNa_VPAN-IPs (**Figure 1C**), and because it was previously suggested that phosphorylation of $Na_V1.5$ may mediate increased I_{NaL} in heart failure (10-15), additional voltage-clamp experiments were designed to test whether phosphorylation at S671 regulates I_{NaL}. These analyses showed that none of the single mutations at S671, or quadruple mutations at S664-671 affect TTX-sensitive I_{NaL} density in HEK-293 cells (**Figure 4 - Figure Supplement 1**). Altogether, therefore, these analyses suggest that phosphorylation at S664 and S667 shifts the voltage-dependence of current activation towards hyperpolarized potentials in a cumulative manner, whereas phosphorylation at S671 decreases the peak Na^+ current density.

Phosphorylation at S671 decreases the cell surface expression of $Na_V1.5$ channels

Additional cell surface biotinylation experiments in transiently transfected HEK-293 cells were designed to determine whether phosphorylation at S671 regulates the cell surface expression of the $Na_V1.5$ channel protein. Interestingly, these experiments revealed that the cell surface expression of the $Na_V1.5$-S671E phosphomimetic channel is significantly ($p<0.001$) decreased, compared with the WT or the $Na_V1.5$-S671A phosphosilent channels, whereas no differences in total $Na_V1.5$ protein expression were observed (**Figures 5A & 5B**). Importantly, the decrease observed with the phosphomimetic mutant, compared with the phosphosilent mutant, suggests that not only this channel locus, but most probably phosphorylation at this particular site, underlies the observed decrease in cell surface expression. Together with the electrophysiological findings, therefore, these biochemical analyses demonstrate a key role for S671 in regulating the cell surface expression of $Na_V1.5$, and suggest that phosphorylation at this site decreases the cell surface expression of $Na_V1.5$-encoded channels.

Simulated consequences of phosphorylation on the first intracellular linker loop of $Na_V1.5$

Like many heavily phosphorylated protein segments (31,32), the first two intracellular linker loops of $Na_V1.5$ are predicted to be intrinsically disordered. Conformational heterogeneity is one of the defining hallmarks of intrinsically disordered regions (IDRs). Heterogeneity is manifest in the amplitude of fluctuations of overall size, shape, and local secondary structural preferences. There is growing recognition of sequence-specificity whereby the ensembles accessible to an IDR are governed by the amino acid composition, extent of phosphorylation, and patterning of residues within the linear sequence.

These sequence-ensemble relationships can be uncovered using all atom simulations. Given the disparate timescales and length scales involved, a robust and efficient approach is to use Markov Chain Metropolis Monte Carlo (MC) simulations based on the ABSINTH implicit solvent model as implemented in the CAMPARI simulation (33-35). Here, we used simulations to quantify sequence-ensemble relationships for the first intracellular linker loop of human $Na_V1.5$ containing the phosphorylation clusters S457-460, S483-486, S497-499, and S664-671 identified by mass spectrometry. For our simulations, we used segments between thirty and forty residues in length, containing each cluster in an approximately central position (441-480 for S457-460, 465-501 for S483-486, 481-515 for S497-499, 651-684 for S664-671). For each cluster, we performed simulations for the WT sequence, as well as phosphomimetic mutations where serine(s)/threonine(s) are replaced with glutamate(s). The results of simulations were analyzed using the device of internal scaling plots. These plots quantify the variation of ensemble-averaged distances between residues i and j as a function of sequence separation |j-i|. Multiple pairs of residues contribute to a given sequence separation |j-i|. The internal scaling profiles can be calibrated against reference profiled that pertain to two kinds of random-coil ensembles. These are designated as EV for excluded volume, which pertains to profiles extracted for self-avoiding walks, and FRC for Flory random coil, which pertains to profiles extracted Flory random coils. Details of these reference ensembles have been published elsewhere.

Simulations of the 441-480 segment showed that the conformational preferences of the unphosphorylated (WT) peptide are akin to those of the FRC reference (**Figure 6A**). This implies that sequence encodes a conformational averaging whereby the peptide-solvent and peptide-peptide interactions are mutually compensatory, thereby giving rise to an ensemble that is maximally heterogeneous. Introduction of phosphomimetic substitutions S457E, S459E and/or S460E did not have a large effect on the ensemble-averaged internal scaling profiles when compared to the unmodified sequence. We obtained similar results for the 465-501 segment, which is also largely unaffected by the introduction of the phosphomimetic mutation(s) of the S483-486 cluster (**Figure 6B**). Conversely, the 481-515 and 651-684 segments were noticeably sensitive to the addition of the negative charges (**Figures 6C & 6D**). When unphosphorylated, these segments preferred conformations that are considerably more compact than the FRC reference. Upon the introduction of cumulative phosphomimetic mutations, these segments gradually expanded in the direction of the EV limit.

Taken together, the results suggest that the intrinsic conformational preferences of the WT sequence dictate the extent of responsiveness of the conformational ensemble to multisite phosphorylation. Sequence stretches that have an intrinsic preference for FRC-like conformations are relatively insensitive to phosphomimetic substitutions of serine/threonine residues. This insensitivity has been quantified for IDRs that undergo multisite phosphorylation (36). In contrast, sequences that have an intrinsic preference for compact conformations become responsive to phosphomimetic substitutions. This would appear to derive from the increased fraction of charged residues (which engenders preferential solvation) and electrostatic repulsions (34). The fraction of charged residues (FCR) and the net charge per residue (NCPR) are known to be direct determinants of the conformational preferences of IDRs (37). Both the 441-480 and 465-501 segments have a higher FCR than the 481-515 and 651-684 segments. The addition of a single negative charge would lead to a greater percent increase in the FCR of the 481-515 and 651-684 segments than it would for the 441-480 and 464-501 segments. As the latter are already expanded, additional charges do not have a large impact on the conformational preference. The more compact starting point of the former allows the phosphomimetic mutations to have a greater effect. While the results for three of the clusters were consistent with the experimental data, those for the S497-499 cluster present an apparent inconsistency. These observations suggest that the ability of this segment to expand due to the addition of charge is not connected to channel gating. Together with the electrophysiological analyses, therefore, these simulations suggest that the effect of phosphorylation at S664 and S667 on the voltage-dependence of channel activation is mediated by the expansion of the area containing the phosphorylation sites, and that this expansion is likely to regulate channel activation allosterically.

Discussion

The results presented here provide a novel, detailed phosphorylation map of the native mouse left ventricular $Na_V1.5$ channel protein, and identify the functional roles of three of these phosphorylation sites in regulating the expression and gating properties of $Na_V1.5$-encoded channels. The highly phosphorylated S664 and S667 shift the voltage-dependence of channel activation towards hyperpolarized potentials in an additive manner, whereas phosphorylation at S671, which is increased in TAC mouse left ventricles, decreases $Na_V1.5$ cell surface expression and peak Na^+ current density. No additional roles could be assigned to the other clusters of $Na_V1.5$ phosphorylation sites, suggesting additional complexity in the mechanisms mediating the phosphorylation-dependent regulation of cardiac $Na_V1.5$ channels.

Phosphorylation map of native mouse left ventricular $Na_V1.5$ channels

The present phosphoproteomic analysis confidently identified a total of 42 native phosphorylation sites in the $Na_V1.5$ channel protein purified from mouse left ventricles, of which 22 are novel. Seventeen of these sites were also found to be phosphorylated in heterologously-expressed $Na_V1.5$ channels (9), suggesting that about half of this phosphorylation pattern is conserved among species (mouse and human) and cellular systems (native channels in left ventricles and recombinant channels in HEK-293 cells), whereas the other half may be associated with more specific and/or localized regulation. Among the sites identified, only six were previously suggested to be the targets for specific kinases using *in silico* and/or *in vitro* analyses: S36 and S525 were attributed to the regulation by PKA, S484 and S664 were assigned to the Serum- and Glucocorticoid-inducible Kinase 3 (SGK3), and S516 and S571 were ascribed to CaMKII (reviewed in (2)). In marked contrast, several previously described phosphorylation sites were not detected in the present study, including the PKA-dependent S528, the CaMKII-associated T594, the Protein Kinase C (PKC)-dependent S1503, the Adenosine Monophosphate-activated Protein Kinase (AMPK)-dependent T101 (38), and the six Fyn-dependent tyrosines (39,40).

Strikingly, and consistent with previous studies from our laboratory (7,8) and the Bers group (9), the results obtained and presented here again revealed that the first intracellular linker loop of $Na_V1.5$ is a hotspot for phosphorylation, with a total of 21 sites identified. Comparisons of the relative abundances of the phosphopeptides identified three highly abundant (and highly phosphorylated) clusters of phosphorylation sites in the first intracellular linker loop of $Na_V1.5$ in mouse left ventricles. The simplest interpretation of this finding is that these three phosphorylation clusters, at positions S457 to S460, S483 to T486, and S664 to S671, are likely involved in regulating the basal and/or gating properties of native cardiac $Na_V1.5$ channels. Conversely, the other phosphorylation sites, with lower stoichiometries, may play spatially- or temporally-distinct roles in the physiological or more pathophysiological regulation of channel expression or gating. This suggestion is highlighted for residue S671, for example, which is substantially (10-fold) less phosphorylated than the nearby S664 and S667 residues in WT mouse left ventricles, but is (2-fold) upregulated in TAC left ventricles. Remarkably, this mass spectrometry analysis also revealed that the vast majority of identified phosphorylation sites (at least 26) are clustered, suggesting concomitant phosphorylation and roles in regulating channel expression and/or function. Unexpectedly, however, except for S664, S667 and S671, no apparent effects of phosphomimetic or phosphosilent mutations were observed on heterologously-expressed (in HEK-293 cells) $Na_V1.5$ current densities or biophysical properties, suggesting a greater complexity than anticipated in the mechanisms contributing to phosphorylation-dependent regulation of $Na_V1.5$ channels.

Phosphorylation at S664 and S667 shifts the voltage-dependence of $Na_V1.5$ channel activation towards hyperpolarized potentials

The electrophysiological analyses presented here identified key roles of S664 and S667 in regulating the voltage-dependence of $Na_V1.5$ channel activation. Indeed, the data demonstrate that the voltage-dependence of activation of quadruple phosphosilent channels at positions S664-671 is shifted towards depolarized potentials, compared to WT channels, whereas phosphomimetic channels display a smaller shift. These findings are consistent with WT channels being phosphorylated at S664 and S667 in

HEK-293 cells, as previously reported (9), and suggest that disruption of phosphorylation at these sites impact channel gating. Confounding this simple interpretation of the data is the fact that glutamate substitution only partially mimics phosphorylation.

Further analyses of the roles of each of the four phosphorylation sites in this cluster revealed the specific involvement of S664 and S667 in regulating gating, whereas modifying T670 or S671 was without effects. Single glutamate mutations at S664 and S667, however, produce the same effects as the single phosphosilent channels. These findings could be attributed to the fact that the side chain of the glutamate only has a single negative charge and a small hydrated shell, which is quite distinct from the covalently attached phosphate group characterized by a doubly negative charge and a large hydrated shell (41). It is likely, therefore, that one glutamate (in single phosphomimetic channels) is not sufficient to mimic phosphorylation at this locus, and that two glutamates (in the quadruple phosphomimetic channel) only partially mimic phosphorylation. The fact that the shifts induced by the single phosphosilent mutations are half the shift generated by the quadruple mutation further supports this hypothesis, and suggests that regulation involving these two sites is cumulative and most likely concomitant. Nevertheless, further investigations, aimed at demonstrating the role of phosphorylation, rather than any other structural determinants associated with this locus, are certainly warranted. In this regard, our findings are also in accordance with previous data reporting the role of SGK3 in shifting the voltage-dependence of channel activation towards more hyperpolarized potentials in *Xenopus* oocytes, whereas the opposite effect was observed with the $Na_V1.5$-S664A phosphosilent channel (42). Although the involvement of SGK3 and S664 in a shared regulation was not directly shown in this previous study, it is tempting to speculate that SGK3 may constitute the kinase phosphorylating S664 and S667 and mediating this regulation.

The effects of phosphorylation were also analyzed using all-atom simulations approach to determine how the introduction of negative charges affects the conformational ensemble of the segments containing the phosphorylation clusters identified by mass spectrometry. These simulations demonstrate that the introduction of negative charges at positions S497-S499 and S664-671 could expand the structure of the containing segments, whereas no effects are likely with the segments containing the S457-460 and S483-486 phosphorylation clusters. Furthermore, for both of the affected segments, the expansion likely gradually increases with the cumulative addition of charges. Interestingly, the simulation findings are consistent with the additive roles of S664 and S667 in regulating the voltage-dependence of channel activation observed in the electrophysiological analyses. Consistent with the proximity of the S664-671 phosphorylation cluster to the DII voltage-sensing domain (DII-VSD) of $Na_V1.5$, which is tightly linked to channel activation (43), our findings suggest that phosphorylation at S664 and S667 regulates channel activation through the expansion of the C-terminal extremity of the first intracellular linker loop of the channel. However, no effects on channel gating were observed with the S497-499 phosphomimetic mutant, even though the simulation showed an effect on its ability to expand. This result suggests that the expansion of this segment, which is more distal to the DII-VSD, does not regulate channel gating.

Phosphorylation at S671 decreases $Na_V1.5$ channel cell surface expression and peak Na^+ current density

The functional analyses also demonstrate that mimicking phosphorylation at S671 decreases the expression of the $Na_V1.5$ protein at the cell surface, as well as peak Na^+ current density in HEK-293 cells. These results suggest that S671 is not phosphorylated in HEK-293 cells, which is in agreement with the previously published mass spectrometric analyses (9). While the phosphomimetic mutation greatly decreases the cell surface expression of $Na_V1.5$, the phosphosilent mutation also reduces $Na_V1.5$ surface expression, albeit to a much smaller extent. These confounding results suggest that the regulation mediated by this locus highly depends on structural changes, and that the phosphomimetic mutation affects the cell surface expression of the channel in part through a change in the structure of the locus. One could further suggest that the greater effect of the phosphomimetic channel may be caused by additional attributes common to the phosphate group and the glutamate side chain. Together, therefore,

these findings highlight the novel role of this locus, and of phosphorylation at this site, in regulating the cell surface expression of $Na_V1.5$ channels.

Interestingly, the mass spectrometric analyses also revealed that phosphorylation at this site is increased in the left ventricles of TAC mice, suggesting a role in mediating the Na_V channel defects associated with heart failure. Because previous studies have suggested that CaMKII-dependent phosphorylation of $Na_V1.5$ may constitute one of the molecular mechanisms mediating the increased late Na^+ current in heart failure (10-15), this finding prompted us to examine the late Na^+ current generated by the phosphosilent and phosphomimetic $Na_V1.5$ mutants at position-671. Our results herein appeared negative, although it cannot be excluded that this regulation may require a specific molecular and cellular environment which is not recapitulated in HEK-293 cells. Additionally, and to our surprise, no changes in phosphorylation at S571 were observed in our TAC model, in contrast with previous findings in nonischemic human heart failure (12) and in several animal models of heart disease (11,12,14). These seemingly disparate findings may reflect technical and/or experimental differences, including differences in the models used and/or stages of disease.

The results presented here raise the interesting and novel possibility that increased phosphorylation at S671 participates in decreasing the peak Na^+ current often observed in heart failure. Consistent with this suggestion, a recent study by the Remme group, using superresolution microscopy, showed a reduction in the size of $Na_V1.5$ clusters in TAC ventricular myocytes without any changes in $Na_V1.5$ transcript or total protein expression (29). Although further studies will be required to determine directly whether these observations are causally linked to increased phosphorylation at S671, the results here provide new hints towards understanding the molecular basis of the decreased peak Na^+ current in heart failure.

Altogether, the results presented here demonstrate that native mouse ventricular $Na_V1.5$ is highly phosphorylated, and that the mechanisms mediating the phosphorylation-dependent regulation of $Na_V1.5$-encoded channels are site-specific, complex, dynamic, and lead to diverse physiological and/or pathological consequences on both channel gating and expression.

Materials and methods

Statement on the use of murine tissue

All investigations conformed to directive 2010/63/EU of the European Parliament, to the Guide for the Care and Use of Laboratory Animals published by the US National Institutes of Health (NIH Publication No. 85-23, revised 1985) and to local institutional guidelines.

Animal model of heart failure

Heart failure was induced by transverse aortic constriction (TAC) as described previously (14). Eight-week-old male C57/BL6J mice were anesthetized using intraperitoneal injections of medetomidine (0.5 mg/kg), midazolam (5 mg/kg) and fentanyl (0.05 mg/kg body weight). A horizontal incision (1-1.5 cm) at the jugulum was used to display the transverse aorta, and a 27-gauge needle was tied against the aorta using a 6.0 non-absorbable suture. After removal of the 27-gauge needle, the skin was closed, and the mice were kept on a heating plate until recovered from the anesthesia. Sham animals underwent the same procedure except for the banding of the transverse aorta. At the end of the surgery, anesthesia was antagonized using intraperitoneal injections of atipamezol (2.5 mg/kg), flumazenil (0.5 mg/kg) and buprenorphine (0.1 mg/kg body weight). For analgesia, metamizole (1.33 mg/ml) was added to the drinking water 2 days before surgery, and supplied for 7 days after operation. In addition, buprenorphine (60 µg/kg body weight) was administered s.c. 1 hr before surgery. A TAC with a mean gradient of less than 5 mmHg was deemed insufficient to induce heart failure and, if observed, the animal was excluded from later analysis. Mice were sacrificed 5 weeks after TAC by cervical dislocation, and left ventricles were harvested, flash-frozen and stored for further analyses.

Mouse echocardiography

Transthoracic echocardiography was performed blinded before and 5 weeks after TAC using a Vevo3100 system (VisualSonics, Toronto, Canada) equipped with a 30-MHz center frequency transducer, as described previously (14). The animals were initially anesthetized with 3% isoflurane, while temperature-, respiration-, and electrocardiogram-controlled anesthesia was maintained with 1.5% isoflurane. Two-dimensional cine loops with frame rates of >200 frames/sec of a long axis view and a short axis view at mid-level of the papillary muscles, as well as M-mode loops of the short axis view were recorded. Thicknesses of the anterior (LVAW) and posterior (LVPW) walls of the left ventricle, the inner diameter of the left ventricle (LVID), and the area of the left ventricular cavity were measured in systole (s) and diastole (d) from the short axis view according to standard procedures (44). Maximal left ventricular length was measured from the long axis view. Systolic and diastolic left ventricular volumes (LV vol) were calculated using the area-length method, and the ejection fraction (EF) was derived. Left ventricular mass (LVM) was calculated from anterior and posterior wall thicknesses using Vevo LAB Software (VisualSonics). PW Doppler ultrasound was used to assess mean gradients (MG) 3 days after the TAC procedure.

Immunoprecipitation of Na_V channel complexes

Flash-frozen left ventricles from 4 Sham and 5 TAC mice were homogenized individually in ice-cold lysis buffer containing 20 mM HEPES (pH 7.4), 150 mM NaCl, 0.5% amidosulfobetaine, 1X complete protease inhibitor cocktail tablet, 1 mM phenylmethylsulfonyl fluoride (PMSF), 0.7 µg/ml pepstatin A (Thermo Fisher Scientific, Waltham, MA) and 1X Halt phosphatase inhibitor cocktail (Thermo Fisher Scientific) as described previously (8). All reagents were from Sigma (Saint Louis, MO) unless otherwise noted. After 15-min rotation at 4°C, 8 mg of the soluble protein fractions were pre-cleared with 200 µL of protein G-magnetic Dynabeads (Thermo Fisher Scientific) for 1 hr, and subsequently used for immunoprecipitations (IP) with 48 µg of an anti-Na_VPAN mouse monoclonal antibody (mαNa_VPAN, Sigma, #S8809), raised against the SP19 epitope (45) located in the third intracellular linker loop and common to all Na_V channel pore-forming subunits. Prior to the IP, antibodies

were cross-linked to 200 µl of protein G-magnetic Dynabeads using 20 mM dimethyl pimelimidate (Thermo Fisher Scientific) (46). Protein samples and antibody-coupled beads were mixed for 2 hrs at 4°C. Magnetic beads were then collected, washed rapidly four times with ice-cold lysis buffer, and isolated protein complexes were eluted from the beads in 1X SDS sample buffer (Bio-Rad Laboratories, Hercules, CA) at 60°C for 10 min. Ninety-nine percent of the immunoprecipitated mouse left ventricular Na_V channel protein complexes were analyzed by MS, and the remaining one percent was used to verify IP yields by western blotting using a rabbit polyclonal anti-$Na_V1.5$ antibody (Rb$\alpha Na_V1.5$, 1:1000, Alomone labs, Jerusalem, Israel, #ASC-005).

Peptide preparation and isobaric labeling for LC-MS

The IP eluates were thawed on ice, reduced, and denatured by heating for 10 min at 95ºC. The Cys residues were alkylated with iodoacetamide (10 mM) for 45 min at room temperature in the dark. The peptides were prepared using a modification (47) of the filter-aided sample preparation method (48). After the addition of 300 µL of 100 mM Tris buffer (pH 8.5) containing 8 M urea (UT) and vortexing, the samples were transferred to YM-30 filter units (Millipore, MRCF0R030) and spun for 14 min at 10,000 rcf (Eppendorf, Model No. 5424). The filters were washed with 200 µl of UT buffer, and the spin-wash cycle was repeated twice. The samples were then exchanged into digest buffer with the addition of 200 µL of 50 mM Tris buffer, pH 8.0, followed by centrifugation (10,000 rcf for 10 min). After transferring the upper filter units to new collection tubes, 80 µL of digest buffer was added, and the samples were digested with trypsin (1 µg) for 4 h at 37ºC. The digestion was continued overnight after adding another aliquot of trypsin. The filter units were then spun for 10 min (10,000 rcf) in an Eppendorf microcentrifuge. The filter was washed with 50 µL of Tris buffer (100 mM, pH 8.0), followed by centrifugation. The digests were extracted three times with 1 ml of ethyl acetate, and acidified to 1% trifluoroacetic acid (TFA) using a 50% aqueous solution. The pH was < 2.0 by checking with pH paper. The solid phase extraction of the peptides was performed using porous graphite carbon micro-tips (49). The peptides were eluted with 60% acetonitrile in 0.1% TFA, and pooled for drying in a Speed-Vac (Thermo Scientific, Model No. Savant DNA 120 concentrator) after adding TFA to 5%. The peptides were dissolved in 20 µL of 1% acetonitrile in water. An aliquot (10%) was removed for quantification using the Pierce Quantitative Fluorometric Peptide Assay kit (Thermo Scientific, Cat. No. 23290). The remainder of the peptides from each IP samples (~0.5-3.5 µg) and 1.16 µg of reference pool peptide were transferred into a new 0.5 mL Eppendorf tube, dried in the Speed-Vac, and dissolved in 12 µL of HEPES buffer (100 mM, pH 8.0, Sigma, H3537).

The samples were labeled with tandem mass tag reagents (TMT11, Thermo Scientific) according to manufacturer's protocol. The labeled samples were pooled, dried, and resuspended in 120 µL of 1% formic acid (FA). The TMT11 labeled sample was desalted as described above for the unlabeled peptides. The eluates were transferred to autosampler vials (Sun-Sri, Cat. No. 200046), dried, and stored at -80ºC for capillary liquid chromatography interfaced to a mass spectrometer (nano-LC-MS).

Nano-LC-MS

The samples in formic acid (1%) were loaded (2.5 µL) onto a 75 µm i.d. × 50 cm Acclaim® PepMap 100 C18 RSLC column (Thermo-Fisher Scientific) on an EASY *nano*-LC (Thermo Fisher Scientific). The column was equilibrated using constant pressure (700 bar) with 20 µL of solvent A (0.1% FA). The peptides were eluted using the following gradient program with a flow rate of 300 nL/min and using solvents A and B (acetonitrile with 0.1% FA): solvent A containing 5% B for 1 min, increased to 25% B over 87 min, to 35% B over 40 min, to 70% B in 6 min and constant 70% B for 6 min, to 95% B over 2 min and constant 95% B for 18 min. The data were acquired in data-dependent acquisition (DDA) mode. The MS1 scans were acquired with the Orbitrap™ mass analyzer over m/z = 375 to 1500 and resolution set to 70,000. Twelve data-dependent high-energy collisional dissociation spectra (MS2) were acquired from each MS1 scan with a mass resolving power set to 35,000, a range of m/z = 100 - 1500, an isolation width of 2 Th, and a normalized collision energy setting of 32%. The maximum injection time

was 60 ms for parent-ion analysis and 120 ms for product-ion analysis. The ions that were selected for MS2 were dynamically excluded for 20 sec. The automatic gain control (AGC) was set at a target value of 3e6 ions for MS1 scans and 1e5 ions for MS2. Peptide ions with charge states of one or ≥ 7 were excluded for higher-energy collision-induced dissociation (HCD) acquisition.

MS data analysis

Peptide identification from raw MS data was performed using PEAKS Studio 8.5 (Bioinformatics Solutions Inc., Waterloo, Canada) (50). The Uni-mouse-Reference-20131008 protein database was used for spectral matching. The precursor and product ion mass tolerances were set to 20 ppm and 0.05 Da, respectively, and the enzyme cleavage specificity was set to trypsin, with a maximum of three missed cleavages allowed. Carbamidomethylation (Cys) and TMT tags (Lys and/or peptide N-terminus) were treated as fixed modifications, while oxidation (Met), pyro-glutamination (Gln), deamidation (Asn and/or Gln), methylation (Lys and/or Arg), dimethylation (Lys and/or Arg), acetylation (Lys) and phosphorylation (Ser, Thr and/or Tyr) were considered variable modifications. The definitive annotation of each $Na_V1.5$ phosphopeptide-spectrum match was obtained by manual verification and interpretation. The phosphorylation site assignments were based on the presence or absence of the unphosphorylated and phosphorylated b- and y-ions flanking the site(s) of phosphorylation, ions referred to as site-discriminating ions throughout this study. When site-discriminating ions were not all detected, the assignment of phosphorylation sites was narrowed down to several possibilities by elimination (for example, pS1056 and/or pT1058). Representative MS/MS spectra, PEAKS -10lgP scores, mass errors of parent ions (in ppm) and charge state confirmations of site-discriminating b- and y-ions are presented in **Table 2, Table 2 - Table Supplement 1 & Figure Supplement 1**.

The protein and peptide relative abundances in TAC, *versus* Sham, mαNa_VPAN-IPs were calculated using quantification of TMT reporter ions. Reporter ion intensities in each TMT channel were normalized to the mean reporter ion intensities of $Na_V1.5$-derived peptides (normalization to spike) to correct for differences in IP yields and technical variabilities. Normalization factors are presented in **Figure 1 - Figure Supplement 1B**. Quantification values of each peptide-spectrum match were exported into Excel, and the mean peptide abundance ratios were calculated from the abundance ratios of all manually verified peptide-spectrum matches assigning to the phosphorylation site(s) of interest. Label-free quantitative analysis of the areas of extracted MS1 chromatograms of phosphorylated and non-phosphorylated peptide ions covering the phosphorylation site(s) of interest was used to evaluate the proportion of phosphorylated to non-phosphorylated peptides at each position, as well as the relative abundances of phosphopeptides.

Plasmids

The $Na_V1.5$ phosphomutant constructs were generated by mutating the serine(s)/threonine(s) to alanine(s) (A) or glutamate(s) (E) by site-directed mutagenesis of a pCI-$Na_V1.5$ plasmid containing the human $Na_V1.5$ hH1C cDNA (30) (NCBI Reference Sequence NM_000335) using the QuikChange II XL Site-Directed Mutagenesis kit (Agilent, Sant Clara, CA) or the Q5 Site-Directed Mutagenesis kit (New England Biolabs, Ipswich, MA). The mutated constructs were then digested with restriction endonucleases to excise the mutated fragments, which were then subcloned into the original pCI-$Na_V1.5$ plasmid. The human $Na_V\beta1$ (NM_001037, a gift from A. L. George) cDNAs was subcloned into pRc/CMV. All constructs were sequenced to ensure that no unintentional mutations were introduced.

Culture and transient transfections

Human Embryonic Kidney 293 (HEK-293) cells were maintained in Dulbecco's Modified Eagle's Medium (DMEM, Thermo Fisher Scientific), supplemented with 10% fetal bovine serum, 100 U/ml penicillin and 100 μg/ml streptomycin, in 37°C, 5% CO_2: 95% air incubator. Cells were transiently transfected at 70-80% confluence in 35 mm dishes with 0.6 μg of the WT or phosphomutant $Na_V1.5$ plasmid and 1.2 μg of the $Na_V\beta1$ plasmid using 2 μL of Lipofectamine 2000 (Thermo Fisher Scientific)

following the manufacturer's instructions. For whole-cell recordings, transfections also contained 0.2 µg of the pEGFP plasmid (Enhanced Green Fluorescent Protein plasmid, Clontech), and EGFP expression served as a marker of transfection. The absolute amounts of the various constructs were calculated and the empty pcDNA3.1 plasmid was used as a filler plasmid to keep the total DNA constant at 2 µg in each transfection.

Electrophysiological recordings

Whole-cell Na_V currents were recorded at room temperature from transiently transfected HEK-293 cells using an Axopatch 200A amplifier (Axon Instruments, Molecular Devices, San Jose, CA) 48 hours after transfection. Voltage-clamp protocols were applied using the pClamp 10.2 software package (Axon Instruments) interfaced to the electrophysiological equipment using a Digidata 1440A digitizer (Axon Instruments). Current signals were filtered at 10 kHz prior to digitization at 50 kHz and storage. Patch-clamp pipettes were fabricated from borosilicate glass (OD: 1.5 mm, ID: 0.86 mm, Sutter Instrument, Novato, CA) using a P-97 micropipette puller (Sutter Instrument), coated with wax, and fire-polished to a resistance between 1.5 and 2.5 MΩ when filled with internal solution. The internal solution contained (in mM): NaCl 5, CsF 115, CsCl 20, HEPES 10, EGTA 10 (pH 7.35 with CsOH, ~300 mosM). The external solution contained (in mM): NaCl 10 (NaCl 20 for analysis of single phosphomutants), CsCl 103, TEA-Cl (tetraethylammonium chloride) 25, HEPES 10, Glucose 5, $CaCl_2$ 1, $MgCl_2$ 2 (pH 7.4 with CsOH, ~300 mosM). All chemicals were purchased from Sigma. After establishing the whole-cell configuration, three minutes were allowed to ensure stabilization of voltage-dependence of activation and inactivation properties, at which time 25 ms voltage steps to ± 10 mV from a holding potential (HP) of -70 mV were applied to allow measurement of whole-cell membrane capacitances, input and series resistances. Only cells with access resistance < 7 MΩ were used, and input resistances were typically > 5 GΩ. After compensation of series resistance (80%), the membrane was held at a HP of -120 mV, and the voltage-clamp protocols were carried out as indicated below. Leak currents were always < 200 pA at HP (-120 mV), and were corrected offline. Cells exhibiting peak current amplitudes < 500 or > 5000 pA were excluded from analyses of biophysical properties because of leak or voltage-clamp issues, respectively, but conserved in analyses of peak current density to avoid bias in evaluation of current densities.

Data were compiled and analyzed using ClampFit 10.2 (Axon Instruments), Microsoft Excel, and Prism (GraphPad Software, San Diego, CA). Whole-cell membrane capacitances (Cm) were determined by analyzing the decays of capacitive transients elicited by brief (25 ms) voltage steps to ± 10 mV from the HP (-70 mV). Input resistances were calculated from the steady-state currents elicited by the same ±10 mV steps (from the HP). Series resistances were calculated by dividing the decay time constants of the capacitive transients (fitted with single exponentials) by the Cm. To determine peak Na^+ current-voltage relationships, currents were elicited by 50-ms depolarizing pulses to potentials ranging from -80 to +40 mV (presented at 5-s intervals in 5-mV increments) from a HP of -120 mV. Peak current amplitudes were defined as the maximal currents evoked at each voltage. Current amplitudes were leak-corrected, normalized to the Cm, and current densities are presented.

To analyze voltage-dependence of current activation properties, conductances (G) were calculated, and conductance-voltage relationships were fitted with the Boltzmann equation $G = G_{max} / (1 + \exp(-(V_m - V_{1/2}) / k))$, in which $V_{1/2}$ is the membrane potential of half-activation and k is the slope factor. The time courses of inactivation of macroscopic currents were fitted with bi-exponential functions, $I(t) = A_{fast} \times \exp(-t/\tau_{fast}) + A_{slow} \times \exp(-t/\tau_{slow}) + A_0$, in which A_{fast} and A_{slow} are the amplitudes of the fast and slow inactivating current components, respectively, and τ_{fast} and τ_{slow} are the decay time constants of A_{fast} and A_{slow}, respectively. A standard two-pulse protocol was used to examine the voltage-dependences of steady-state inactivation. From a HP of -120 mV, 1-s conditioning pulses to potentials ranging from -120 to -45 mV (in 5-mV increments) were followed by 20-ms test depolarizations to -20 mV (interpulse intervals were 5-s). Current amplitudes evoked from each conditioning voltage were measured and normalized to the maximal current (I_{max}) evoked from -120 mV, and normalized currents were plotted as a function of the conditioning voltage. The resulting steady-state inactivation curves were fitted with the Boltzmann equation $I = I_{max} / (1 + \exp((V_m - V_{1/2}) / k))$, in which $V_{1/2}$ is the membrane potential of half-

inactivation and k is the slope factor. To examine the rates of recovery from inactivation, a three-pulse protocol was used. Cells were first depolarized to -20 mV (from a HP of -120 mV) to inactivate the channels, and subsequently repolarized to -120 mV for varying times (ranging from 1 to 200 ms), followed by test depolarizations to -20 mV to assess the extent of recovery (interpulse intervals were 5-s). The current amplitudes at -20 mV, measured following each recovery period, were normalized to the maximal current amplitude and plotted as function of the recovery time. The resulting plot was fitted with a single exponential function $I(t) = A \times (1 - \exp(-t / \tau_{rec}))$ to determine the recovery time constant. For each of these biophysical properties, data from individual cells were first fitted and then averaged.

The currents generated on expression of each phosphosilent and phosphomimetic $Na_V1.5$ mutant were recorded and compared to currents generated by the $Na_V1.5$-WT construct obtained on the same days of patch-clamp analyses. The densities and properties of $Na_V1.5$-WT currents in each data set were similar, and for the sake of clarity, a single representative $Na_V1.5$-WT channel data set was chosen and presented in **Figure 3 - Figure Supplement 2 and Table Supplement 1 and Figure 4 - Table Supplement 1**.

In experiments aimed at recording the tetrodotoxin (TTX)-sensitive late Na^+ current, cells were bathed in external solution containing (in mM): NaCl 120, TEA-Cl 25, HEPES 10, Glucose 5, $CaCl_2$ 1, $MgCl_2$ 2 (pH 7.4 with CsOH, ~300 mosM). Repetitive 350-ms test pulses to -20 mV from a HP of -120 mV (at 5-s intervals) were applied to cells to record Na^+ currents in the absence of TTX. Cells were then superfused locally with the external solution supplemented with 30 μM TTX (Bio-Techne SAS, Rennes, France). Only cells exhibiting peak current amplitudes > 4000 pA were used (those with peak currents < 4000 pA did not show measurable late Na^+ current), and cells with difference in leak current amplitudes before and after TTX application > 5 pA at -20 mV (calculated from leak currents at -120 mV) were excluded from analyses. TTX-sensitive currents from individual cells were determined by offline digital subtraction of average leak-subtracted currents obtained from 5 recordings in the absence and in the presence of TTX after achieving steady state. The amplitude of TTX-sensitive late Na^+ current was defined as the steady-state current amplitude (A_0) obtained by fitting the inactivation decay of macroscopic TTX-sensitive current with the double exponential function $I(t) = A_{fast} \times \exp(-t/\tau_{fast}) + A_{slow} \times \exp(-t/\tau_{slow}) + A_0$. For each cell, the TTX-sensitive late Na^+ current amplitude was normalized to the peak Na^+ current amplitude, and expressed as a percentage of the peak Na^+ current.

Cell surface biotinylation and western blot analyses

Surface biotinylation of HEK-293 cells was completed as described previously (51). Briefly, cells were incubated with the cleavable EZ-Link Sulfo-NHS-SS-Biotin (0.5 mg/ml, Thermo Fisher Scientific) in ice-cold PBS (pH 7.4) for 30 min at 4°C. Free biotin was quenched with Tris-saline (10 mM Tris (pH 7.4), 120 mM NaCl), and detergent-soluble cell lysates were prepared. Biotinylated cell surface proteins were affinity-purified using NeutrAvidin-conjugated agarose beads (Thermo Fisher Scientific), and purified cell surface proteins were analyzed by western blot using the mαNa_VPAN antibody (1:2000, Sigma, #S8809), the anti-transferrin receptor mouse monoclonal antibody (TransR, 1:1000, Thermo Fisher Scientific), and the anti-glyceraldehyde 3-phosphate dehydrogenase mouse monoclonal antibody (GAPDH, 1:100000, Santa Cruz Biotechnology). Bound primary antibodies were detected using horseradish peroxidase-conjugated goat anti-mouse secondary antibodies (Cell Signaling Technology, Inc., Danvers, MA), and protein signals were visualized using the SuperSignal West Dura Extended Duration Substrate (Thermo Fisher Scientific). Bands corresponding to $Na_V1.5$ were normalized to bands corresponding to TransR from the same sample. $Na_V1.5$ phosphomutant protein expression (total or cell surface) is expressed relative to $Na_V1.5$-WT protein expression (total or cell surface).

Molecular simulations

Molecular simulations were performed with the CAMPARI software package (35), using the ABSINTH implicit solvation model (52) and parameters from the OPLS-AA forcefield. Markov Chain Metropolis Monte Carlo moves sampled the conformational space of each protein segment. To mimic a 5

mM NaCl concentration, neutralizing and excess Na^+ and Cl^- ions were modeled explicitly with the protein segments in spherical droplets of (5 x number of residues) Å radius. Ten simulation runs were performed for each sequence construct, and the average of these ten runs was then plotted. The simulations denoted as EV (Excluded Volume) and FRC (Flory Random Coil) are reference models. In the EV limit, the only interactions considered are the pairwise repulsions. In the FRC limit, conformations are constructed by randomly sampling residue-specific backbone dihedral angles. Three EV and three FRC simulation runs were performed for each protein segment, and the averages were plotted.

Statistical analyses

Results are expressed as means ± SEM. Data were first tested for normality using the D'Agostino and Pearson normality test. Depending on the results of normality tests, statistical analyses were then performed using the Mann-Whitney nonparametric test, the Kruskal-Wallis one-way ANOVA followed by the Dunn's post-hoc test, or the one-way ANOVA followed by the Dunnett's post-hoc test, as indicated in Figures and Tables. All these analyses, as well as plots and graphs were performed using Prism (GraphPad Software).

Acknowledgements: This work was supported by the *Agence Nationale de la Recherche* [ANR-15-CE14-0006-01 and ANR-16-CE92-0013-01 to CM], the Deutsche Forschungsgemeinschaft (DFG) [Ma 1982/5-1 to LSM], and the National Institutes of Health [R01-HL148803 to CM, RVP and JRS; R01-HL034161 and R01-HL142520 to JMN; and 5R01NS056114 to RVP]. The mass spectrometric experiments were performed at the Washington University Proteomics Shared Resource (WU-PSR). The WU-PSR is supported in part by the WU Institute of Clinical and Translational Sciences (NCATS UL1 TR000448), the Mass Spectrometry Research Resource (NIGMS P41 GM103422) and the Siteman Comprehensive Cancer Center Support Grant (NCI P30 CA091842). ML was supported by a *Groupe de Réflexion sur la Recherche Cardiovasculaire-Société Française de Cardiologie* predoctoral fellowship [SFC/GRRC2018]. SB was supported by a Lefoulon-Delalande postdoctoral fellowship. The expert technical assistance of Petra Erdmann-Gilmore, Yiling Mi and Rose Connors is gratefully acknowledged. The content of the research reported is solely the responsibility of the authors and does not necessarily represent the official view of the funding agencies.

Competing Interests: The authors declare that they have no conflicts of interest with the contents of this article.

Author Contributions: CM designed the study and wrote the paper. CM, DM, JMN, RRT and LSM designed, performed and/or analyzed the mass spectrometry experiments. ML, SB, AL, CC, PMC, BE, JMN and CM designed, performed and/or analyzed the functional analyses. EW, KMR, RVP and JRS designed, performed and/or analyzed the modeling analyses. SW and LSM provided the Sham/TAC mice and performed mouse echocardiography. All authors reviewed the results and approved the final version of the manuscript.

References

1. Remme, C. A., and Bezzina, C. R. (2010) Sodium channel (dys)function and cardiac arrhythmias. *Cardiovasc Ther* **28**, 287-294
2. Marionneau, C., and Abriel, H. (2015) Regulation of the cardiac Na channel Na1.5 by post-translational modifications. *J Mol Cell Cardiol* **82**, 36-47
3. Pei, Z., Xiao, Y., Meng, J., Hudmon, A., and Cummins, T. R. (2016) Cardiac sodium channel palmitoylation regulates channel availability and myocyte excitability with implications for arrhythmia generation. *Nat Commun* **7**, 12035
4. Plant, L. D., Xiong, D., Romero, J., Dai, H., and Goldstein, S. A. N. (2020) Hypoxia Produces Pro-arrhythmic Late Sodium Current in Cardiac Myocytes by SUMOylation of NaV1.5 Channels. *Cell Rep* **30**, 2225-2236 e2224
5. Yu, P., Hu, L., Xie, J., Chen, S., Huang, L., Xu, Z., Liu, X., Zhou, Q., Yuan, P., Yan, X., Jin, J., Shen, Y., Zhu, W., Fu, L., Chen, Q., Yu, J., Hu, J., Cao, Q., Wan, R., and Hong, K. (2018) O-GlcNAcylation of cardiac Nav1.5 contributes to the development of arrhythmias in diabetic hearts. *Int J Cardiol* **260**, 74-81
6. Schubert, B., VanDongen, A. M., Kirsch, G. E., and Brown, A. M. (1989) Beta-adrenergic inhibition of cardiac sodium channels by dual G-protein pathways. *Science* **245**, 516-519
7. Burel, S., Coyan, F. C., Lorenzini, M., Meyer, M. R., Lichti, C. F., Brown, J. H., Loussouarn, G., Charpentier, F., Nerbonne, J. M., Townsend, R. R., Maier, L. S., and Marionneau, C. (2017) C-terminal phosphorylation of NaV1.5 impairs FGF13-dependent regulation of channel inactivation. *J Biol Chem* **292**, 17431-17448
8. Marionneau, C., Lichti, C. F., Lindenbaum, P., Charpentier, F., Nerbonne, J. M., Townsend, R. R., and Merot, J. (2012) Mass Spectrometry-Based Identification of Native Cardiac Nav1.5 Channel alpha Subunit Phosphorylation Sites. *J Proteome Res* **11**, 5994-6007
9. Herren, A. W., Weber, D. M., Rigor, R. R., Margulies, K. B., Phinney, B. S., and Bers, D. M. (2015) CaMKII Phosphorylation of Na(V)1.5: Novel in Vitro Sites Identified by Mass Spectrometry and Reduced S516 Phosphorylation in Human Heart Failure. *J Proteome Res* **14**, 2298-2311
10. Aiba, T., Barth, A. S., Hesketh, G. G., Hashambhoy, Y. L., Chakir, K., Tunin, R. S., Greenstein, J. L., Winslow, R. L., Kass, D. A., and Tomaselli, G. F. (2013) Cardiac resynchronization therapy improves altered Na channel gating in canine model of dyssynchronous heart failure. *Circ Arrhythm Electrophysiol* **6**, 546-554
11. Glynn, P., Musa, H., Wu, X., Unudurthi, S. D., Little, S., Qian, L., Wright, P. J., Radwanski, P. B., Gyorke, S., Mohler, P. J., and Hund, T. J. (2015) Voltage-Gated Sodium Channel Phosphorylation at Ser571 Regulates Late Current, Arrhythmia, and Cardiac Function In Vivo. *Circulation* **132**, 567-577
12. Koval, O. M., Snyder, J. S., Wolf, R. M., Pavlovicz, R. E., Glynn, P., Curran, J., Leymaster, N. D., Dun, W., Wright, P. J., Cardona, N., Qian, L., Mitchell, C. C., Boyden, P. A., Binkley, P. F., Li, C., Anderson, M. E., Mohler, P. J., and Hund, T. J. (2012) Ca2+/Calmodulin-Dependent Protein Kinase II-Based Regulation of Voltage-Gated Na+ Channel in Cardiac Disease. *Circulation* **126**, 2084-2094
13. Maltsev, V. A., Reznikov, V., Undrovinas, N. A., Sabbah, H. N., and Undrovinas, A. (2008) Modulation of late sodium current by Ca2+, calmodulin, and CaMKII in normal and failing dog cardiomyocytes: similarities and differences. *Am J Physiol Heart Circ Physiol* **294**, H1597-1608
14. Toischer, K., Hartmann, N., Wagner, S., Fischer, T. H., Herting, J., Danner, B. C., Sag, C. M., Hund, T. J., Mohler, P. J., Belardinelli, L., Hasenfuss, G., Maier, L. S., and Sossalla, S. (2013) Role of late sodium current as a potential arrhythmogenic mechanism in the progression of pressure-induced heart disease. *J Mol Cell Cardiol* **61**, 111-122

15. Wagner, S., Dybkova, N., Rasenack, E. C., Jacobshagen, C., Fabritz, L., Kirchhof, P., Maier, S. K., Zhang, T., Hasenfuss, G., Brown, J. H., Bers, D. M., and Maier, L. S. (2006) Ca2+/calmodulin-dependent protein kinase II regulates cardiac Na+ channels. *J Clin Invest* **116**, 3127-3138
16. Maltsev, V. A., Silverman, N., Sabbah, H. N., and Undrovinas, A. I. (2007) Chronic heart failure slows late sodium current in human and canine ventricular myocytes: implications for repolarization variability. *Eur J Heart Fail* **9**, 219-227
17. Valdivia, C. R., Chu, W. W., Pu, J., Foell, J. D., Haworth, R. A., Wolff, M. R., Kamp, T. J., and Makielski, J. C. (2005) Increased late sodium current in myocytes from a canine heart failure model and from failing human heart. *J Mol Cell Cardiol* **38**, 475-483
18. Xi, Y., Wu, G., Yang, L., Han, K., Du, Y., Wang, T., Lei, X., Bai, X., and Ma, A. (2009) Increased late sodium currents are related to transcription of neuronal isoforms in a pressure-overload model. *Eur J Heart Fail* **11**, 749-757
19. Zicha, S., Maltsev, V. A., Nattel, S., Sabbah, H. N., and Undrovinas, A. I. (2004) Post-transcriptional alterations in the expression of cardiac Na+ channel subunits in chronic heart failure. *J Mol Cell Cardiol* **37**, 91-100
20. Ashpole, N. M., Herren, A. W., Ginsburg, K. S., Brogan, J. D., Johnson, D. E., Cummins, T. R., Bers, D. M., and Hudmon, A. (2012) Ca2+/Calmodulin-dependent Protein Kinase II (CaMKII) Regulates Cardiac Sodium Channel NaV1.5 Gating by Multiple Phosphorylation Sites. *J Biol Chem* **287**, 19856-19869
21. Hund, T. J., Koval, O. M., Li, J., Wright, P. J., Qian, L., Snyder, J. S., Gudmundsson, H., Kline, C. F., Davidson, N. P., Cardona, N., Rasband, M. N., Anderson, M. E., and Mohler, P. J. (2010) A beta(IV)-spectrin/CaMKII signaling complex is essential for membrane excitability in mice. *J Clin Invest* **120**, 3508-3519
22. Mishra, S., Reznikov, V., Maltsev, V. A., Undrovinas, N. A., Sabbah, H. N., and Undrovinas, A. (2014) Contribution of sodium channel neuronal isoform Nav1.1 to late sodium current in ventricular myocytes from failing hearts. *J Physiol*
23. Dybkova, N., Ahmad, S., Pabel, S., Tirilomis, P., Hartmann, N., Fischer, T. H., Bengel, P., Tirilomis, T., Ljubojevic, S., Renner, A., Gummert, J., Ellenberger, D., Wagner, S., Frey, N., Maier, L. S., Streckfuss-Bomeke, K., Hasenfuss, G., and Sossalla, S. (2018) Differential regulation of sodium channels as a novel proarrhythmic mechanism in the human failing heart. *Cardiovasc Res* **114**, 1728-1737
24. Kaab, S., Dixon, J., Duc, J., Ashen, D., Nabauer, M., Beuckelmann, D. J., Steinbeck, G., McKinnon, D., and Tomaselli, G. F. (1998) Molecular basis of transient outward potassium current downregulation in human heart failure: a decrease in Kv4.3 mRNA correlates with a reduction in current density. *Circulation* **98**, 1383-1393
25. Noyes, A. M., Zhou, A., Gao, G., Gu, L., Day, S., Andrew Wasserstrom, J., and Dudley, S. C. (2017) Abnormal sodium channel mRNA splicing in hypertrophic cardiomyopathy. *Int J Cardiol* **249**, 282-286
26. Shang, L. L., Pfahnl, A. E., Sanyal, S., Jiao, Z., Allen, J., Banach, K., Fahrenbach, J., Weiss, D., Taylor, W. R., Zafari, A. M., and Dudley, S. C., Jr. (2007) Human heart failure is associated with abnormal C-terminal splicing variants in the cardiac sodium channel. *Circ Res* **101**, 1146-1154
27. Liu, M., Gu, L., Sulkin, M. S., Liu, H., Jeong, E. M., Greener, I., Xie, A., Efimov, I. R., and Dudley, S. C., Jr. (2013) Mitochondrial dysfunction causing cardiac sodium channel downregulation in cardiomyopathy. *J Mol Cell Cardiol* **54**, 25-34
28. Luo, L., Ning, F., Du, Y., Song, B., Yang, D., Salvage, S. C., Wang, Y., Fraser, J. A., Zhang, S., Ma, A., and Wang, T. (2017) Calcium-dependent Nedd4-2 upregulation mediates degradation of the cardiac sodium channel Nav1.5: implications for heart failure. *Acta Physiol (Oxf)* **221**, 44-58
29. Rivaud, M. R., Agullo-Pascual, E., Lin, X., Leo-Macias, A., Zhang, M., Rothenberg, E., Bezzina, C. R., Delmar, M., and Remme, C. A. (2017) Sodium Channel Remodeling in Subcellular Microdomains of Murine Failing Cardiomyocytes. *J Am Heart Assoc* **6**

30. Makielski, J. C., Ye, B., Valdivia, C. R., Pagel, M. D., Pu, J., Tester, D. J., and Ackerman, M. J. (2003) A ubiquitous splice variant and a common polymorphism affect heterologous expression of recombinant human SCN5A heart sodium channels. *Circ Res* **93**, 821-828
31. Iakoucheva, L. M., Radivojac, P., Brown, C. J., O'Connor, T. R., Sikes, J. G., Obradovic, Z., and Dunker, A. K. (2004) The importance of intrinsic disorder for protein phosphorylation. *Nucleic Acids Res* **32**, 1037-1049
32. Wright, P. E., and Dyson, H. J. (2015) Intrinsically disordered proteins in cellular signalling and regulation. *Nat Rev Mol Cell Biol* **16**, 18-29
33. Das, R. K., and Pappu, R. V. (2013) Conformations of intrinsically disordered proteins are influenced by linear sequence distributions of oppositely charged residues. *Proc Natl Acad Sci U S A* **110**, 13392-13397
34. Mao, A. H., Crick, S. L., Vitalis, A., Chicoine, C. L., and Pappu, R. V. (2010) Net charge per residue modulates conformational ensembles of intrinsically disordered proteins. *Proc Natl Acad Sci U S A* **107**, 8183-8188
35. Vitalis, A., and Pappu, R. V. (2009) Methods for Monte Carlo simulations of biomacromolecules. *Annu Rep Comput Chem* **5**, 49-76
36. Martin, E. W., Holehouse, A. S., Grace, C. R., Hughes, A., Pappu, R. V., and Mittag, T. (2016) Sequence Determinants of the Conformational Properties of an Intrinsically Disordered Protein Prior to and upon Multisite Phosphorylation. *J Am Chem Soc* **138**, 15323-15335
37. Holehouse, A. S., and Pappu, R. V. (2018) Collapse Transitions of Proteins and the Interplay Among Backbone, Sidechain, and Solvent Interactions. *Annu Rev Biophys*
38. Liu, X., Chen, Z., Han, Z., Liu, Y., Wu, X., Peng, Y., Di, W., Lan, R., Sun, B., Xu, B., and Xu, W. (2019) AMPK-mediated degradation of Nav1.5 through autophagy. *FASEB J* **33**, 5366-5376
39. Ahern, C. A., Zhang, J. F., Wookalis, M. J., and Horn, R. (2005) Modulation of the cardiac sodium channel NaV1.5 by Fyn, a Src family tyrosine kinase. *Circ Res* **96**, 991-998
40. Iqbal, S. M., Aufy, M., Shabbir, W., and Lemmens-Gruber, R. (2018) Identification of phosphorylation sites and binding pockets for modulation of NaV 1.5 channel by Fyn tyrosine kinase. *FEBS J* **285**, 2520-2530
41. Hunter, T. (2012) Why nature chose phosphate to modify proteins. *Philos Trans R Soc Lond B Biol Sci* **367**, 2513-2516
42. Boehmer, C., Wilhelm, V., Palmada, M., Wallisch, S., Henke, G., Brinkmeier, H., Cohen, P., Pieske, B., and Lang, F. (2003) Serum and glucocorticoid inducible kinases in the regulation of the cardiac sodium channel SCN5A. *Cardiovasc Res* **57**, 1079-1084
43. Varga, Z., Zhu, W., Schubert, A. R., Pardieck, J. L., Krumholz, A., Hsu, E. J., Zaydman, M. A., Cui, J., and Silva, J. R. (2015) Direct Measurement of Cardiac Na+ Channel Conformations Reveals Molecular Pathologies of Inherited Mutations. *Circ Arrhythm Electrophysiol* **8**, 1228-1239
44. Gao, S., Ho, D., Vatner, D. E., and Vatner, S. F. (2011) Echocardiography in Mice. *Curr Protoc Mouse Biol* **1**, 71-83
45. Vassilev, P. M., Scheuer, T., and Catterall, W. A. (1988) Identification of an intracellular peptide segment involved in sodium channel inactivation. *Science* **241**, 1658-1661
46. Schneider, C., Newman, R. A., Sutherland, D. R., Asser, U., and Greaves, M. F. (1982) A one-step purification of membrane proteins using a high efficiency immunomatrix. *J Biol Chem* **257**, 10766-10769
47. Erde, J., Loo, R. R., and Loo, J. A. (2014) Enhanced FASP (eFASP) to increase proteome coverage and sample recovery for quantitative proteomic experiments. *J Proteome Res* **13**, 1885-1895
48. Wisniewski, J. R., Zougman, A., Nagaraj, N., and Mann, M. (2009) Universal sample preparation method for proteome analysis. *Nat Methods* **6**, 359-362
49. Chen, Z. W., Fuchs, K., Sieghart, W., Townsend, R. R., and Evers, A. S. (2012) Deep amino acid sequencing of native brain GABAA receptors using high-resolution mass spectrometry. *Mol Cell Proteomics* **11**, M111 011445

50. Zhang, J., Xin, L., Shan, B., Chen, W., Xie, M., Yuen, D., Zhang, W., Zhang, Z., Lajoie, G. A., and Ma, B. (2012) PEAKS DB: de novo sequencing assisted database search for sensitive and accurate peptide identification. *Mol Cell Proteomics* **11**, M111 010587
51. Marionneau, C., Carrasquillo, Y., Norris, A. J., Townsend, R. R., Isom, L. L., Link, A. J., and Nerbonne, J. M. (2012) The sodium channel accessory subunit Navbeta1 regulates neuronal excitability through modulation of repolarizing voltage-gated K(+) channels. *J Neurosci* **32**, 5716-5727
52. Vitalis, A., and Pappu, R. V. (2009) ABSINTH: a new continuum solvation model for simulations of polypeptides in aqueous solutions. *J Comput Chem* **30**, 673-699

Figure Legends

Figure 1. Localization and quantification of 42 MS-identified $Na_V1.5$ phosphorylation sites in mαNa_VPAN-IPs from Sham and TAC mouse left ventricles. (**A**) Schematic representation of phosphorylation sites on the $Na_V1.5$ protein (UniProt reference sequence K3W4N7). Two phosphorylation site locations are possible at amino acids S1056-T1058. (**B**) The areas of extracted MS1 ion chromatograms, corresponding to MS2 spectra assigning phosphorylated (in red) and non-phosphorylated (in white) $Na_V1.5$ peptides at indicated phosphorylation site(s), in mαNa_VPAN-IPs from Sham and TAC left ventricles are indicated. (**C**) Distributions and mean ± SEM relative abundances of individual $Na_V1.5$ phosphopeptides allowing assignments of indicated phosphorylation site(s), in TAC LV (n=5, in black), *versus* Sham LV (n=4, in white), mαNa_VPAN-IPs, were obtained using TMT reporter ion intensities. The relative abundances of $Na_V1.5$ phosphopeptides exhibiting phosphorylation(s) on serine-671 (S671, n=12 peptides) alone, or in combination with serines-664 (S664 + S671, n=9 peptides) or -667 (S667 + S671, n=7 peptides) are increased (**p<0.01, ***p<0.001, Mann-Whitney test) in TAC LV, *versus* Sham LV, mαNa_VPAN-IPs.

Figure 1 - Figure Supplement 1. Immunoprecipitation yields and relative quantification of $Na_V1.5$ peptide abundances from Sham and TAC mouse left ventricles. (**A**) Representative western blots of total lysates and mαNa_VPAN-IPs from Sham and TAC left ventricles probed with the anti-$Na_V1.5$ rabbit polyclonal (Rb$\alpha Na_V1.5$) and anti-GAPDH mouse monoclonal antibodies. (**B**) Normalization factors used in MS1 and MS2 analyses to correct for technical variabilities in $Na_V1.5$ protein abundance in mαNa_VPAN-IPs from Sham and TAC left ventricles. (**C**) Distribution of TAC/Sham $\log_2$ normalized ratios of $Na_V1.5$ peptide-spectrum matches. Both biochemical (**A**) and mass spectrometry (**B, C**) analyses of $Na_V1.5$ immunoprecipitation yields and peptide relative abundance demonstrate low technical variability.

Figure 1 - Figure Supplement 2. Relative abundances of phosphorylated $Na_V1.5$ peptides at indicated phosphorylation site(s) in mαNa_VPAN-IPs from Sham and TAC mouse left ventricles. Values correspond to the areas of extracted MS1 ion chromatograms corresponding to MS2 spectra assigning phosphorylated peptides at indicated phosphorylation site(s). The brackets indicate the subgroups of phosphorylation sites analyzed in **Figure 1B**. Independent quantification of S459 and S460 phosphorylated peptides was not possible because localization of the phosphorylation site in most of the phosphorylated peptides could not be discriminated.

Figure 2. $Na_V1.5$ amino acid sequence coverage and localization of 42 $Na_V1.5$ phosphorylation sites in mαNa_VPAN-IPs from Sham and TAC mouse left ventricles. Covered sequence and MS-identified phosphorylation sites are highlighted in yellow and red, respectively; transmembrane segments (S1-S6) in each domain (I-IV) are in bold and underlined in black; and loops I, II and III correspond to interdomains I-II, II-III and III-IV, respectively. Two peptides differing by the presence or absence of a glutamine (Q) at position-1080 were detected, reflecting the expression of two $Na_V1.5$ variants (the Q1080 variant corresponds to UniProt reference sequence K3W4N7; and the Q1080del variant corresponds to Q9JJV9). Two phosphorylation site locations are possible at amino acids S1056-T1058 (in green).

Figure 3. Phosphorylation at positions S664-671 regulates the voltage-dependence of current activation and peak Na^+ current density. (**A**) Representative whole-cell voltage-gated Na^+ currents recorded forty-eight hours following transfection of HEK-293 cells with $Na_V1.5$-WT + $Na_V\beta1$ (black), $Na_V1.5$-S664-671A + $Na_V\beta1$ (blue) or $Na_V1.5$-S664-671E + $Na_V\beta1$ (red) using the protocols illustrated in each panel. Scale bars are 1 nA and 2 ms. (**B**) Voltage-dependences of current activation and steady-state inactivation. The voltage-dependence of current activation is shifted towards depolarized potentials in cells expressing the $Na_V1.5$-S664-671A or $Na_V1.5$-S664-671E mutants, compared to cells expressing

$Na_V1.5$-WT. (**C**) Mean ± SEM peak Na^+ current (I_{Na}) densities plotted as a function of test potential. The peak I_{Na} density is reduced in cells expressing the $Na_V1.5$-S664-671E mutant, compared to cells expressing $Na_V1.5$-WT. Mean ± SEM times to peak (**D**), and fast (τ_{fast}, **E**) and slow (τ_{slow}, **F**) inactivation time constants plotted as a function of test potential. The time to peak, τ_{fast} and τ_{slow} are higher in cells expressing the $Na_V1.5$-S664-671A or $Na_V1.5$-S664-671E mutants, compared to cells expressing $Na_V1.5$-WT. Current densities, time- and voltage-dependent properties, as well as statistical comparisons across groups, are provided in **Figure 3 - Figure Supplement 2 & Table Supplement 1**.

Figure 3 - Figure Supplement 1. Conservation of phosphorylation sites in mouse and human $Na_V1.5$. The mouse (Reference sequence NP_001240789.1) and human (NP_000326.2) $Na_V1.5$ sequences are aligned, and phosphorylation sites identified on the mouse sequence and conserved in human are highlighted in red. Two phosphorylation site locations are possible at amino acids S1056-T1058 (in green). Transmembrane segments (S1-S6) in each domain (I-IV) are in bold and underlined in black; loops I, II and III correspond to interdomains I-II, II-III and III-IV, respectively. The seven phosphorylation clusters analyzed electrophysiologically are boxed in red.

Figure 3 - Figure Supplement 2. Distributions and mean ± SEM membrane potentials for half-activation (**A**) and half-inactivation (**C**), peak Na^+ current (I_{Na}) densities (**B**), and time constants of recovery from inactivation (**D**) of WT and mutant $Na_V1.5$ channels. Currents were recorded as described in the legend to **Figure 3**. The I_{Na} densities presented were determined from analyses of records obtained on depolarizations to -20 mV (HP=-120 mV). $^{\#}p<0.05$ *versus* $Na_V1.5$-WT; one-way ANOVA followed by the Dunnett's post-hoc test. $^{***}p<0.001$ *versus* $Na_V1.5$-WT; Kruskal-Wallis followed by the Dunn's post-hoc test. Current densities, time- and voltage-dependent properties, as well as statistical comparisons across groups, are provided in **Figure 3 - Table Supplement 1**.

Figure 4. Phosphorylation at S664 and S667 regulates the voltage-dependence of current activation, whereas phosphorylation at S671 regulates the peak Na^+ current density. Currents were recorded as described in the legend to **Figure 3**. The voltage-dependence of current activation is shifted towards more depolarized potentials in cells expressing $Na_V1.5$-S664A (**A**), $Na_V1.5$-S664E (**A**), $Na_V1.5$-S667A (**B**) or $Na_V1.5$-S667E (**B**), compared to cells expressing $Na_V1.5$-WT, whereas no significant differences are observed with the $Na_V1.5$-T670 (**C**) or $Na_V1.5$-S671 (**D**) phosphomutants. (**E to H**) The mean ± SEM peak Na^+ current (I_{Na}) densities are plotted as a function of test potential. The peak I_{Na} density is reduced in cells expressing $Na_V1.5$-S671E (**H**), compared to cells expressing $Na_V1.5$-WT, whereas no significant differences are observed with the other phosphomutants. Current densities, time- and voltage-dependent properties, as well as statistical comparisons across groups, are provided in **Figure 4 - Table Supplement 1**.

Figure 4 - Figure Supplement 1. Distributions and mean ± SEM TTX-sensitive late Na^+ current (I_{NaL}) densities of quadruple S664-671 (**A**) and simple S671 (**B**) $Na_V1.5$ phosphomutants. TTX-sensitive I_{NaL} were evoked during prolonged depolarizations (350 ms at -20 mV, HP=-120 mV) forty-eight hours after transfection of HEK-293 cells with WT (black), phosphosilent (blue) and phosphomimetic (red) $Na_V1.5$ channels and $Na_V\beta1$. No significant differences between mutant and WT channels were observed.

Figure 5. Phosphorylation at S671 regulates the cell surface expression of $Na_V1.5$. (**A**) Representative western blots of total (left panel) and cell surface (right panel) $Na_V1.5$ from HEK-293 cells transiently transfected with $Na_V1.5$-WT + $Na_V\beta1$, $Na_V1.5$-S671A + $Na_V\beta1$ or $Na_V1.5$-S671E + $Na_V\beta1$. Samples were probed in parallel with the anti-transferrin receptor (TransR) and anti-glyceraldehyde 3-phosphate dehydrogenase (GAPDH) antibodies. (**B**) Mean ± SEM total and cell surface $Na_V1.5$ protein expression in transiently transfected HEK-293 cells (n=12 in 6 different experiments). Expression of $Na_V1.5$ in each sample was first normalized to the TransR protein in the same blot and then expressed relative to $Na_V1.5$ protein expression (total or cell surface) in cells transfected with $Na_V1.5$-WT + Navβ1. Relative (mean ±

SEM) $Na_V1.5$ cell surface expression is different (***p<0.001, one-way ANOVA followed by the Dunnett's post-hoc test) in cells expressing $Na_V1.5$-WT, $Na_V1.5$-S671A and $Na_V1.5$-S671E channels.

Figure 6. Simulations of phosphorylation of segments of the first intracellular linker loop of $Na_V1.5$. The sequential distance between pair of residues is on the x-axis, and the average spatial distance between a pair of residues separated by the specified sequential distance is on the y-axis. <Rij> is the average simulated spatial distance between all residue pairs separated in the amino acid sequence by |j-i| residues. The WT sequences are plotted in black. Phosphorylation is simulated by single or multiple replacement of serines/threonines with glutamates (E), and resulting simulations are plotted in gradation of reds. The Flory Random Coil (FRC, in blue) and Excluded Volume (EV, in purple) limits are plotted for reference (see text). (**A**) Sequence 441-480 contains the phosphosites S457, S459 and S460; (**B**) sequence 465-501 contains the phosphosites S483, S484 and T486; (**C**) sequence 481-515 contains the phosphosites S497 and S499; and (**D**) sequence 651-684 contains the phosphosites S664, S667, T670 and S671.

Table 2 - Figure Supplement 1. Representative MS/MS spectra of singly or doubly phosphorylated $Na_V1.5$, $Na_V1.4$ and $Na_V1.3$ tryptic peptides (listed in **Table 2 & Table 2 - Table Supplement 1**). The presence of the b- (highlighted in blue) and y- (in red) ion series describing the amino acid sequences, and of the unphosphorylated and phosphorylated site-discriminating ions unambiguously supported the assignments of the indicated phosphorylation site(s). The PEAKS -10lgP peptide scores and the mass errors of parent ions (in ppm) for each phosphopeptide are indicated at the top of each page. The charge state confirmations of site-discriminating ions are presented in **Table 2 & Table 2 - Table Supplement 1**.

Table 1. Proteins identified in immunoprecipitated Na_v channel complexes from Sham and TAC mouse left ventricles using MS

Protein	UniProt accession number	Number of exclusive unique peptides	% Amino acid sequence coverage	TAC/Sham ratio
$Na_v1.5$ (Q1080) $Na_v1.5$ (Q1080del)	K3W4N7 Q9JJV9	310	56%	1.0
$Na_v1.4$	G3X8T7	86	40%	0.8
$Na_v1.3$	A2ASI5	24	17%	0.9
$Na_v1.8$	Q6QIY3	13	9%	0.9
$Na_v1.7$	Q62205	3	2%	0.7
$Na_v1.9$	Q9R053	1	1%	1.2
$Na_v1.1$	A2APX8	1	0.5%	1.3
$Na_v1.2$	B1AWN6	1	0.5%	1.2
$Na_v1.6$	F6U329	1	0.6%	1.0
Navβ4	Q7M729	11	44%	0.7
Navβ1	P97952	9	41%	1.0
Navβ2	Q56A07	6	37%	0.8
Calmodulin	Q3UKW2	12	53%	0.8
FHF2-VY	P70377	37	84%	0.8
FHF4	P70379	1	7%	0.7
Ankyrin-G	G5E8K5	47	32%	1.0
Ankyrin-R	Q02357	2	2%	1.0
Ankyrin-B	S4R245	1	0.4%	0.8
Dystrophin	P11531	88	29%	0.9
α-1-syntrophin	A2AKD7	20	53%	0.8
β-2-syntrophin	Q61235	19	35%	0.9
α-actinin-2	Q9JI91	50	60%	0.5
Caveolin-1	P49817	6	39%	0.8
Caveolin-2	Q9WVC3	3	28%	0.9
Caveolin-3	P51637	2	11%	0.8
Vinculin	Q64727	25	29%	0.7
N-cadherin	P15116	13	24%	0.8
Plakophilin-2	Q9CQ73	13	20%	0.7
Plakophilin-1	P97350	5	8%	0.8
Telethonin	O70548	5	44%	0.8
Desmoglein-2	O55111	13	19%	0.7
Flotillin-1	O08917	22	59%	0.9
Flotillin-2	Q60634	21	54%	0.8
14-3-3 zeta/delta	P63101	5	27%	0.9
14-3-3 epsilon	P62259	3	17%	1.0
14-3-3 gamma	P61982	3	14%	1.0
14-3-3 beta/alpha	Q9CQV8	1	6%	1.1
14-3-3 sigma	O70456	1	3%	0.9
Slmap	Q3URD3	1	1%	1.1
αB-crystallin	P23927	14	71%	0.7
Cx43	P23242	15	50%	0.7
Kir2.1	P35561	3	11%	0.8
CaMKIIγ	Q923T9	11	26%	0.8
CaMKIIδ	E9Q1T1	2	6%	1.1
CaMKIIα	P11798	2	4%	0.8
CaMKIIβ	Q5SVI2	1	3%	0.9
PKA, catalytic subunit, α	P05132	2	9%	1.0
PKAβ-2	Q6PAM0	1	4%	1.1
PKCβ	P68404	2	3%	1.6
Fyn	P39688	1	2%	1.1
PP2A-C	P63330	1	3%	1.1

The numbers of exlusive unique peptides, the percent (%) amino acid sequence coverages and the fold change abundance ratios in TAC LV (n=5) *versus* Sham LV (n=4) mαNa_vPAN-IPs for each identified protein are presented. No significant differences in protein abundance were observed between TAC and Sham IPs. Abbreviations: Na_v, voltage-gated Na^+ channel; FHF, Fibroblast growth factor Homologous Factor; Slmap, sarcolemmal membrane-associated protein; Cx, connexin; Kir, inward rectifier K^+ channel; CaMKII, Ca^{2+}/Calmodulin-dependent protein Kinase II; PKA, Protein Kinase A; PKC, Protein Kinase C. PP2A-C, Catalytic subunit of Protein Phosphatase 2A.

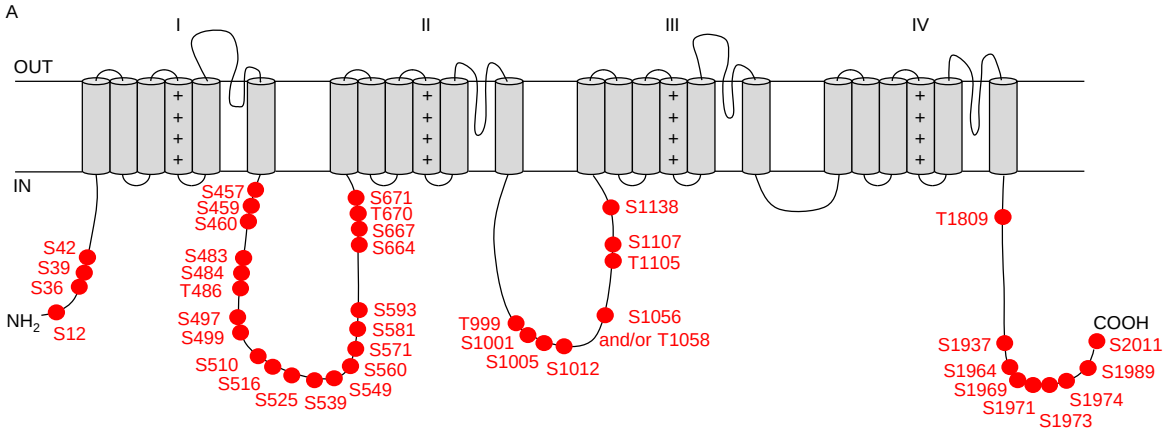

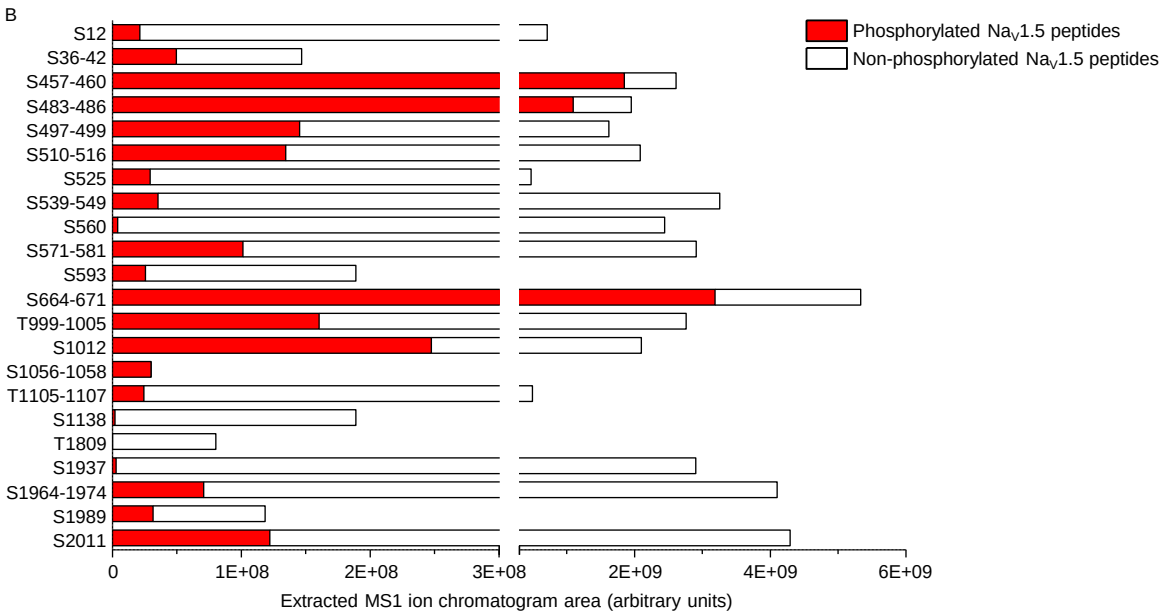

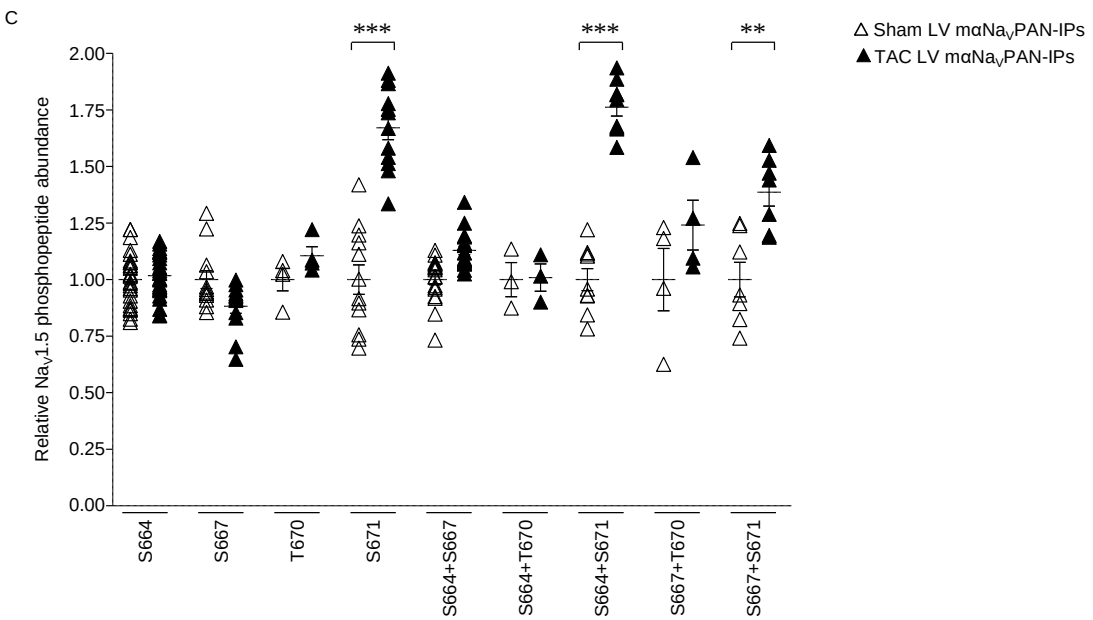

Figure 1.

Figure 1 - Table Supplement 1. Echocardiographic parameters of Sham and TAC mice before and 5 weeks after surgery

	Before surgery			After surgery			Sham before/after surgery	TAC before/after surgery
	Sham (n=4)	TAC (n=5)	*p* value	Sham (n=4)	TAC (n=5)	*p* value	*p* value	*p* value
BW (g)	27.1 ± 1.0	26.9 ± 0.7	0.905	28.8 ± 0.9	29.3 ± 0.6	0.905	0.200	0.095
HR (bpm)	455 ± 14	468 ± 20	0.905	472 ± 9	479 ± 4	0.556	0.343	0.421
LVAW;d (mm)	0.87 ± 0.05	0.91 ± 0.05	0.730	1.10 ± 0.03	1.04 ± 0.05	0.556	0.029	0.151
LVID;d (mm)	3.97 ± 0.15	3.74 ± 0.10	0.190	3.98 ± 0.23	4.03 ± 0.12	0.905	1.000	0.151
LVPW;d (mm)	0.82 ± 0.02	0.73 ± 0.04	0.176	0.78 ± 0.05	1.05 ± 0.06	0.032	0.686	0.012
LVM (mg)	99.1 ± 6.5	87.7 ± 4.9	0.286	120.2 ± 7.8	138.3 ± 9.6	0.286	0.114	0.008
LVM/BW (mg/g)	3.7 ± 0.2	3.2 ± 0.1	0.286	4.2 ± 0.2	4.7 ± 0.3	0.190	0.343	0.008
LV vol;d (µl)	69.3 ± 6.0	60.1 ± 4.0	0.190	70.2 ± 9.3	71.8 ± 5.1	0.905	1.000	0.151
SV (µl)	42.3 ± 4.7	39.7 ± 4.5	0.556	43.8 ± 5.5	29.3 ± 2.1	0.063	0.686	0.095
CO (mL/min)	19.2 ± 2.1	18.5 ± 2.1	0.905	20.6 ± 2.6	14.0 ± 1.0	0.063	0.686	0.095
EF (%)	60.9 ± 3.6	65.4 ± 3.5	0.730	62.5 ± 1.2	40.8 ± 0.9	0.016	1.000	0.008
MG (mmHg)	N/A	N/A	N/A	1.1 ± 0.2	12.1 ± 2.7	0.016	N/A	N/A

All values are means ± SEM. *p* values were obtained using the Mann-Whitney test. Abbreviations: BW, body weight; HR, heart rate; LVAW;d, LV anterior wall thickness at end-diastole; LVID;d, LV inner diameter at end-diastole; LVPW;d, LV posterior wall thickness at end-diastole; LVM, LV mass; LVM/BW, LV mass to body weight ratio; LV vol;d, LV volume at end-diastole; SV, stroke volume; CO, cardiac output; EF, ejection fraction; MG, mean gradient; bpm, beats per minute.

A

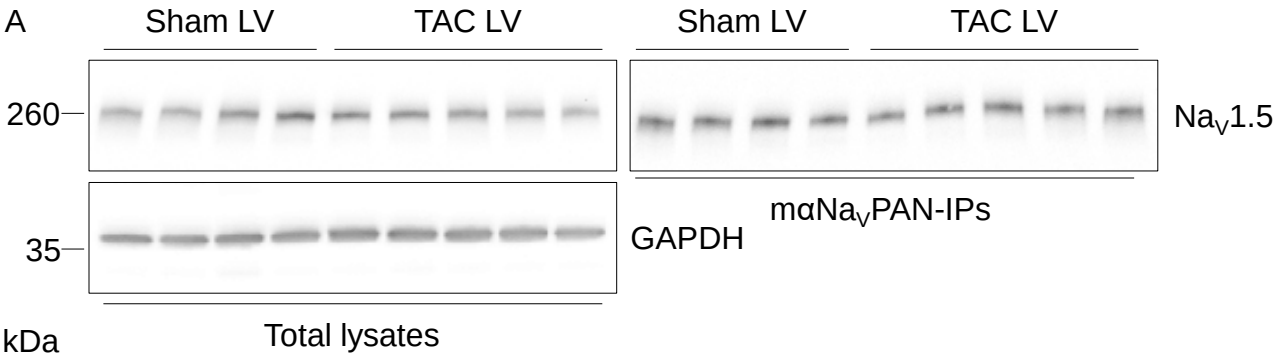

B

Sample	Channel	Normalization factor
Sham LV 2	TMT10-127N	1.04
Sham LV 6	TMT10-127C	0.99
Sham LV 9	TMT10-128N	1.15
Sham LV 10	TMT10-128C	0.99
TAC LV 3	TMT10-129N	1.17
TAC LV 4	TMT10-129C	1.00
TAC LV 5	TMT10-130N	1.26
TAC LV 7	TMT10-130C	1.08
TAC LV 8	TMT10-131	1.22

C

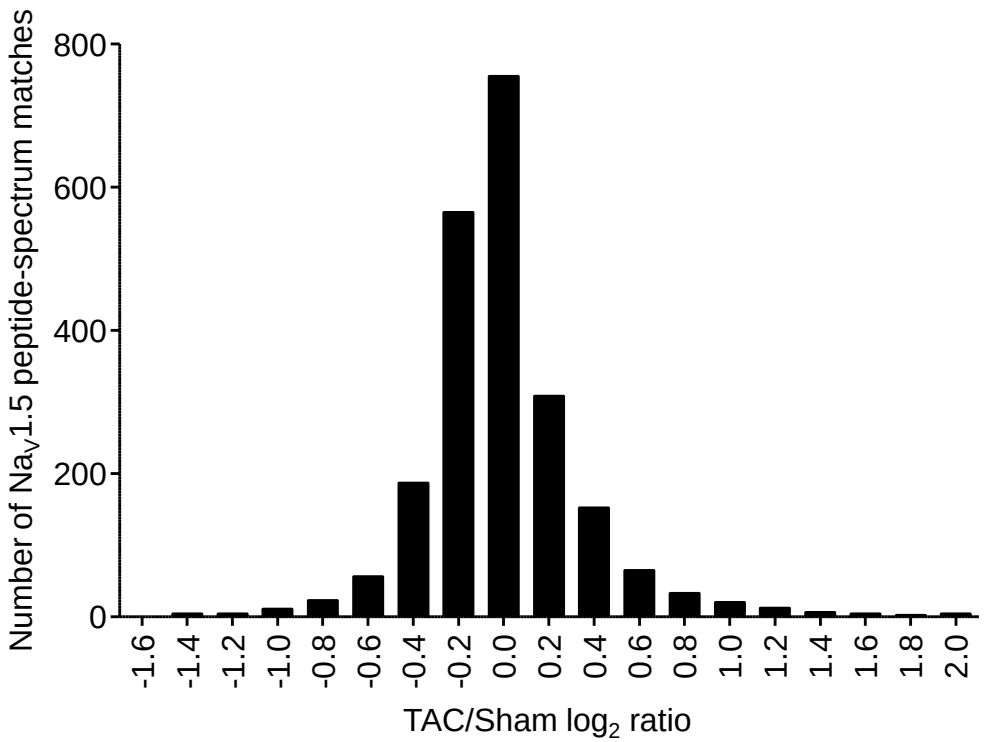

Figure 1 - Figure Supplement 1.

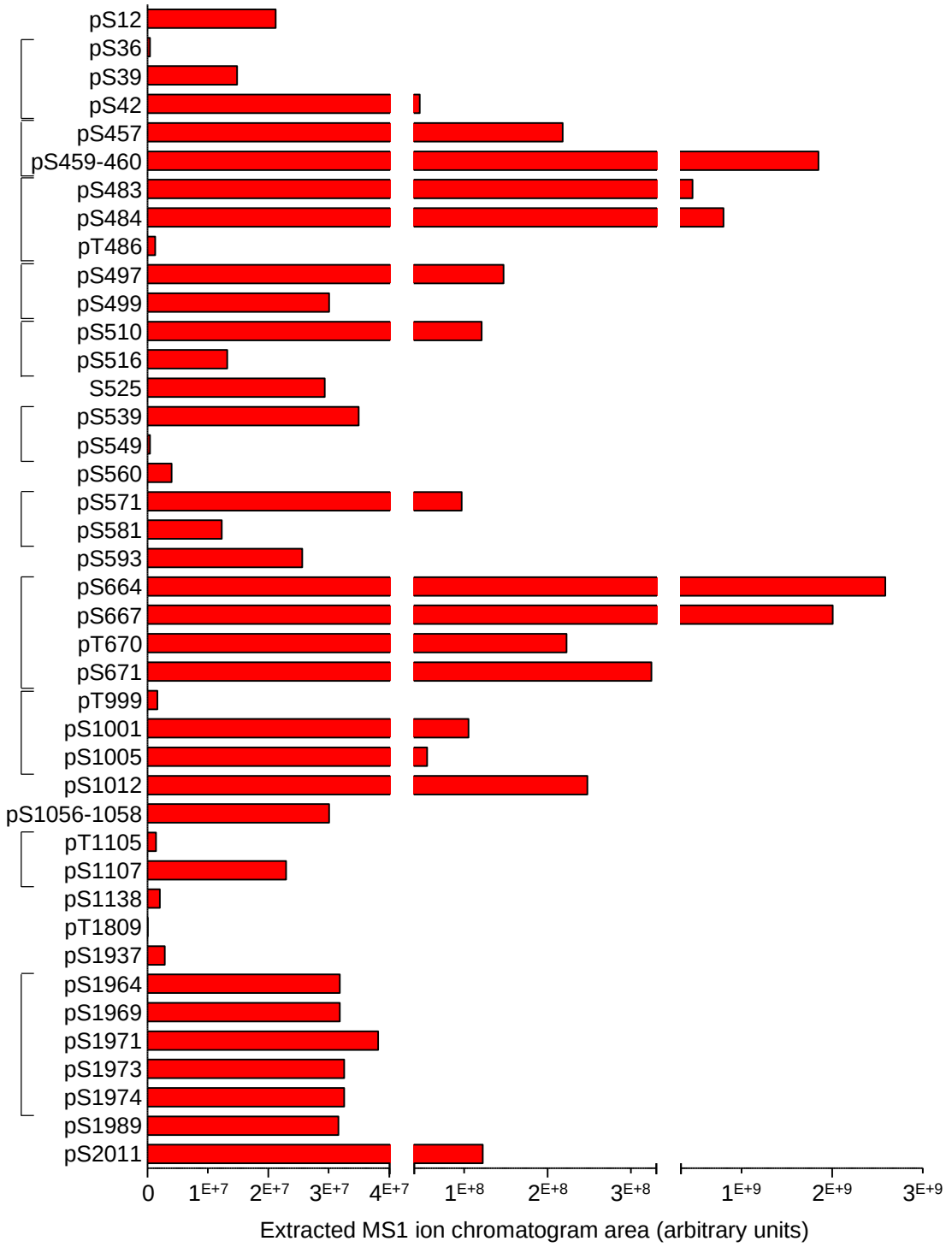

Figure 1 - Figure Supplement 2.

Table 2. Phosphorylation sites, phosphopeptides and site-discriminating ions identified in immunoprecipitated $Na_v1.5$ proteins from Sham and TAC mouse left ventricles using MS

Phosphorylation site(s)	Phosphopeptide sequence	*m/z* (charge)	-10lgP score	b ion	Phospho b ion	y ion	Phospho y ion	TAC/Sham ratio
S12	9-GTS(pS)FRR	560.279 (+2)	21.6	b3 (+1)	(-)	y3	(-)	1.2 (n=1)
S36	35-G(pS)ATSQESR	616.279 (+2)	32.1	b1	(-)	y7	(-)	1.3 (n=1)
S42	35-GSATSQE(pS)REGLPEEEAPRPQLDLQASK	887.947 (+4)	73.1	b7 (+1)	(-)	y19 (+2)	y21 (+2)	1.5 ± 0.03 (n=3)
S39 + S42	35-GSAT(pS)QE(pS)REGLPEEEAPRPQLDLQASK	907.937 (+4)	68.4	b4 (+1)	(-)	y19 (+2)	y21	1.2 ± 0.12 (n=2)
S457 (+ S459 or S460)	452-GVDTV(pS)RSSLEMSPLAPVTNHER	957.782 (+3)	77.1	b5 (+1)	b7(-98) (+2)	y14 (+1)	(-)	1.1 ± 0.09 (n=10)
S459 + S460	452-GVDTVSR(pS)(pS)LEMSPLAPVTNHER	958.117 (+3)	41.5	b7 (+2)	b11 (+2)	y12 (+1)	(-)	1.2 (n=1)
S460	459-S(pS)LEMSPLAPVTNHER	1039.003 (+2)	61.2	b1 (+1)	b4 (+1)	y14 (+1)	(-)	1.0 ± 0.05 (n=18)
S483	481-RL(pS)SGTEDGGDDRLPK	561.038 (+4)	52.4	b2	b3	y13 (+2)	(-)	1.0 ± 0.03 (n=10)
S484	482-LS(pS)GTEDGGDDR	759.319 (+2)	45.7	b2	(-)	y9 (+1)	(-)	1.2 ± 0.07 (n=12)
T486	484-SG(pT)EDGGDDRLPK	628.973 (+3)	21.9	b1	b5	y8 (+2)	(-)	1.2 (n=1)
S483 + S484	480-KRL(pS)(pS)GTEDGGDDRLPK	536.476 (+5)	63	b3	(-)	y12 (+2)	(-)	1.3 ± 0.04 (n=19)
S497	482-LSSGTEDGGDDRLPK(pS)DSEDGPR	732.845 (+4)	60.2	b12 (+2)	(-)	y7 (+1)	y12	1.3 ± 0.07 (n=7)
S483 + S497	481-RL(pS)SGTEDGGDDRLPK(pS)DSEDGPR	791.862 (+4)	40.1	b2	b3 (-98)	y6 (+1)	y12 (+2)	0.7 (n=1)
S484 + S497	482-LS(pS)GTEDGGDDRLPK(pS)DSEDGPR	1003.448 (+3)	54.8	b2 (+1)	b3	y7 (+1)	y12 (+2)	1.7 ± 0.04 (n=2)
S499	497-SD(pS)EDGPR	586.245 (+2)	42	b2	b5	y4 (+1)	y6	1.4 ± 0.17 (n=3)
S510	505-ALNQL(pS)LTHGLSR	573.643 (+3)	51.8	b4 (+1)	(-)	y7 (+1)	(-)	0.9 ± 0.03 (n=3)
S516	505-ALNQLSLTHGL(pS)R	573.644 (+3)	46.7	b9	(-)	y1 (+1)	(-)	0.9 (n=1)
S525	524-S(pS)RGSIFTFR	489.584 (+3)	40.7	b1 (+1)	(-)	y8 (+2)	(-)	0.8 ± 0.09 (n=3)
S539	536-DQG(pS)EADFADDENSTAGESESHR	921.701 (+3)	70.9	b3 (+1)	b5 (+1)	y14 (+1)	(-)	1.5 ± 0.09 (n=9)
S549	534-RRDQGSEADFADDEN(pS)TAGESESHR	769.579 (+4)	55.3	b15 (+2)	(-)	y9 (+1)	(-)	3.2 (n=1)
S560	559-T(pS)LLVPWPLR	745.921 (+2)	30.2	b1	b4	y8 (+1)	(-)	1.0 (n=1)
S571	569-RP(pS)TQGQPGFGTSAPGHVLNGK	911.466 (+3)	55.2	b1 (+1)	b7 (+1), b7 (+2)	y19	(-)	0.8 ± 0.03 (n=19)
S581	569-RPSTQGQPGFGT(pS)APGHVLNGK	683.856 (+4)	48.5	b12 (+2)	(-)	y8 (+2)	(-)	0.9 (n=1)
S593	591-RN(pS)TVDCNGVVSLLGAGDAEATSPGSHLLR	841.660 (+4)	71.7	b2	b3	y16 (+1)	(-)	0.8 ± 0.05 (n=4)
S664	662-AL(pS)AVSVLTSALEELEESHRK	936.506 (+3)	60.6	b2 (+1)	b5 (+1)	y18 (+2)	(-)	1.0 ± 0.04 (n=28)
S667	662-ALSAV(pS)VLTSALEELEESHR	817.416 (+3)	64.1	b5 (+1)	b7 (+1)	y13 (+1)	(-)	0.9 ± 0.06 (n=12)
T670	662-ALSAVSVL(pT)SALEELEESHRK	702.629 (+4)	54.3	b7 (+1)	(-)	y12 (+2)	(-)	1.1 ± 0.1 (n=4)
S671	662-ALSAVSVLT(pS)ALEELEESHRK	702.629 (+4)	63.2	b9 (+2)	b10 (+2)	y11 (+2)	(-)	1.7 ± 0.17 (n=12)***
S664 + S667	662-AL(pS)AV(pS)VLTSALEELEESHRK	886.771 (+3)	58.8	b2	b3	y15 (+2)	y18	1.1 ± 0.05 (n=18)
S664 + T670	662-AL(pS)AVSVL(pT)SALEELEESHR	844.072 (+3)	59.3	b2 (+1)	b5 (+1), b8 (+1)	y11 (+1)	(-)	1.0 ± 0.14 (n=3)
S664 + S671	662-AL(pS)AVSVLT(pS)ALEELEESHR	844.072 (+3)	58.3	b2 (+1)	b5 (+1), b9 (+2)	y10 (+1)	(-)	1.8 ± 0.13 (n=9)***
S667 + T670	662-ALSAV(pS)VL(pT)SALEELEESHRK	722.621 (+4)	54.1	b5 (+1)	b8	y12 (+2)	(-)	1.2 ± 0.37 (n=4)
S667 + S671	662-ALSAV(pS)VLT(pS)ALEELEESHR	844.073 (+3)	60.5	b5 (+1)	b8 (+1), b9	y10 (+1)	(-)	1.4 ± 0.17 (n=7)**
T999	993-KPAALA(pT)HSQLPSCIAAPR	824.114 (+3)	48.8	b6 (+1)	(-)	y12 (+1)	(-)	0.8 (n=1)
S1001	1001-(pS)QLPSCIAAPR	503.591 (+3)	32.6	(-)	b2 (+1)	y8 (+1)	(-)	1.0 ± 0.11 (n=4)
S1005	993-KPAALATHSQLP(pS)CIAAPRSPPPPEVEKAPPAR	702.389 (+6)	71.4	b11 (+2)	(-)	y18 (+2)	y21 (+2)	0.8 ± 0.16 (n=2)
S1012	1012-(pS)PPPPEVEK	759.405 (+2)	42.3	(-)	b1 (+1)	y8 (+1)	(-)	0.9 ± 0.03 (n=17)
S1056 and/or T1058	1030-FEEDKRPGQGTPGDTEPVCVPIAVAESDTDDQEEDEENSLGT EEEESSK (1 Phospho)	1230.559 (+5)	57.3	b24 (+2)	(-)	y11 (+1)	(-)	1.8 ± 0.04 (n=5)
T1105	1097-AWSQVSET(pT)SSEAEASTSQADWQQER	1070.132 (+3)	64.3	b8 (+1)	b9	y12 (+1)	(-)	1.1 (n=1)
S1107	1097-AWSQVSETTS(pS)EAEASTSQADWQQER	1070.135 (+3)	69.9	b10 (+1)	b15 (+1)	y14 (+1)	(-)	1.2 (n=1)
S1138	1136-ED(pS)YSEGSTADMTNTADLLEQIPDLGEDVKDPEDCFTEGCVR	1312.582 (+4)	44.7	(-)	b3 (+1)	y23 (+2)	(-)	1.3 ± 0.01 (n=2)
T1809	1809-(pT)QFIEYLALSDFADALSEPLR	903.451 (+3)	54.8	(-)	b1, b2 (+1)	y14 (+1)	(-)	0.8 (n=1)
S1937	1933-QQAG(pS)SGLSDEDAPER	978.430 (+2)	60.1	b4 (+1)	(-)	y11 (+1)	(-)	1.3 (n=1)
S1964	1964-(pS)GPLSSSSISSTSFPPSYDSVTR	885.752 (+3)	50.3	(-)	b1 (+1), b4 (+1)	y14 (+1)	(-)	1.2 ± 0.11 (n=3)
S1969	1964-SGPLS(pS)SSISSTSFPPSYDSVTR	885.753 (+3)	56.9	b5	b6 (+2)	y14 (+1)	(-)	1.0 ± 0.04 (n=3)
S1971	1963-RSGPLSSS(pS)ISSTSFPPSYDSVTR	937.787 (+3)	48.5	b8 (+1)	(-)	y14 (+1)	(-)	0.9 ± 0.09 (n=3)
S1973	1964-SGPLSSSSI(pS)STSFPPSYDSVTR	885.750 (+3)	61.8	b9 (+1)	b10 (+2)	y13	(-)	0.9 ± 0.02 (n=6)
S1974	1964-SGPLSSSSIS(pS)TSFPPSYDSVTR	885.750 (+3)	61.8	b10	(-)	y12 (+1)	(-)	0.9 ± 0.03 (n=2)
S1989	1987-AT(pS)DNLPVR	641.324 (+2)	37.7	b2	b5	y6 (+1)	(-)	0.8 ± 0.07 (n=2)
S2011	2002-SEDLADFPP(pS)PDRDR	675.975 (+3)	38.8	b7 (+1)	(-)	y5 (+2)	y8	1.0 ± 0.05 (n=15)

The site-discriminating ions observed in MS/MS spectra of each annotated $Na_v1.5$ (UniProt reference sequence K3W4N7) phosphopeptide support the assignment of the indicated phosphorylation site(s). The -10lgP scores attest quality of peptide identification. The manually verified charge state of unphosphorylated and phosphorylated site-discriminating b and y ions is reported in parentheses. The (-) symbol indicates that the ion was not detected. Mean ± SEM phosphopeptide abundance ratios in TAC LV (n=5) *versus* Sham LV (n=4) mαNa_vPAN-IPs were calculated from n phosphopeptide(s). **, $p < 0.01$; ***, $p < 0.001$, Mann-Whitney test.

Table 2 - Table Supplement 1. Phosphorylation sites, phosphopeptides and site-discriminating ions identified in co-immunoprecipitated Na_V α subunits from Sham and TAC mouse left ventricles using MS

Na_V α subunit	Phosphorylation site(s)	Phosphopeptide sequence	*m/z* (charge)	-10lgP	b ion	Phospho b ion	y ion	Phospho y ion	TAC/Sham ratio
$Na_V1.4$	S522 + S525	512-GPPRPSCSAE(pS)AI(pS)DAMEELEEAHQK	861.889 (+4)	48.1	b10 (+2)	b12	y11	(-)	1.0 ± 0.01 (n=2)
$Na_V1.4$	S525	512-GPPRPSCSAESAI(pS)DAMEELEEAHQK	841.893 (+4)	60.3	b13 (+2)	b15 (+2)	y10 (+2)	(-)	1.0 ± 0.07 (n=2)
$Na_V1.4$	S900	899-S(pS)IEMDHLNFINNPYLTIHVPIASEESDLEMPTEEET DTFSEPEDIK	1486.948 (+4)	54.2	b1	b2	(-)	(-)	1.3 (n=1)
$Na_V1.4$	S1819	1790-EKDSTEDAGPTTEVTAPSSSDTALTPPPP(pS)PPPP SSPPQGQTVRPGVK	927.474 (+6)	52.0	(-)	(-)	y18 (+2)	y19 (+2)	0.7 ± 0.17 (n=2)
$Na_V1.3$	S658	656-AM(pS)IASILTNTMEELEESR	817.386 (+3)	64.0	b2	b5	(-)	(-)	0.7 (n=1)

The site-discriminating ions observed in MS/MS spectra of each annotated $Na_V1.4$ and $Na_V1.3$ phosphopeptide support the assignment of the indicated phosphorylation site(s). The -10lgP scores attest quality of peptide identification. The manually verified charge state of unphosphorylated and phosphorylated site-discriminating b and y ions is reported in parentheses. The (-) symbol indicates that the ion was not detected. Mean ± SEM phosphopeptide abundance ratios in TAC LV (n=5) *versus* Sham LV (n=4) mαNa_VPAN-IPs were calculated from n phosphopeptide(s). No significant differences between TAC and Sham IPs were observed.

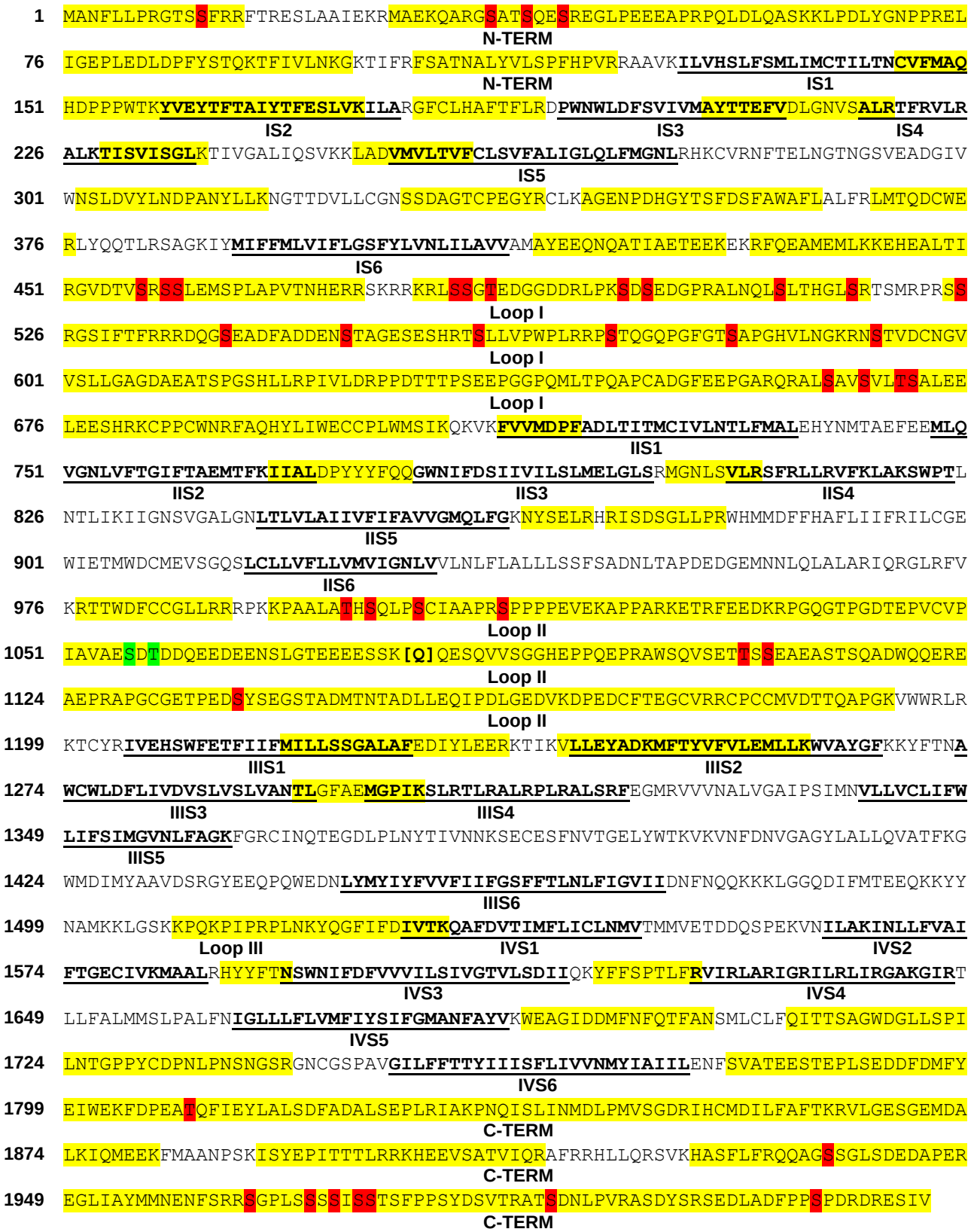

Figure 2.

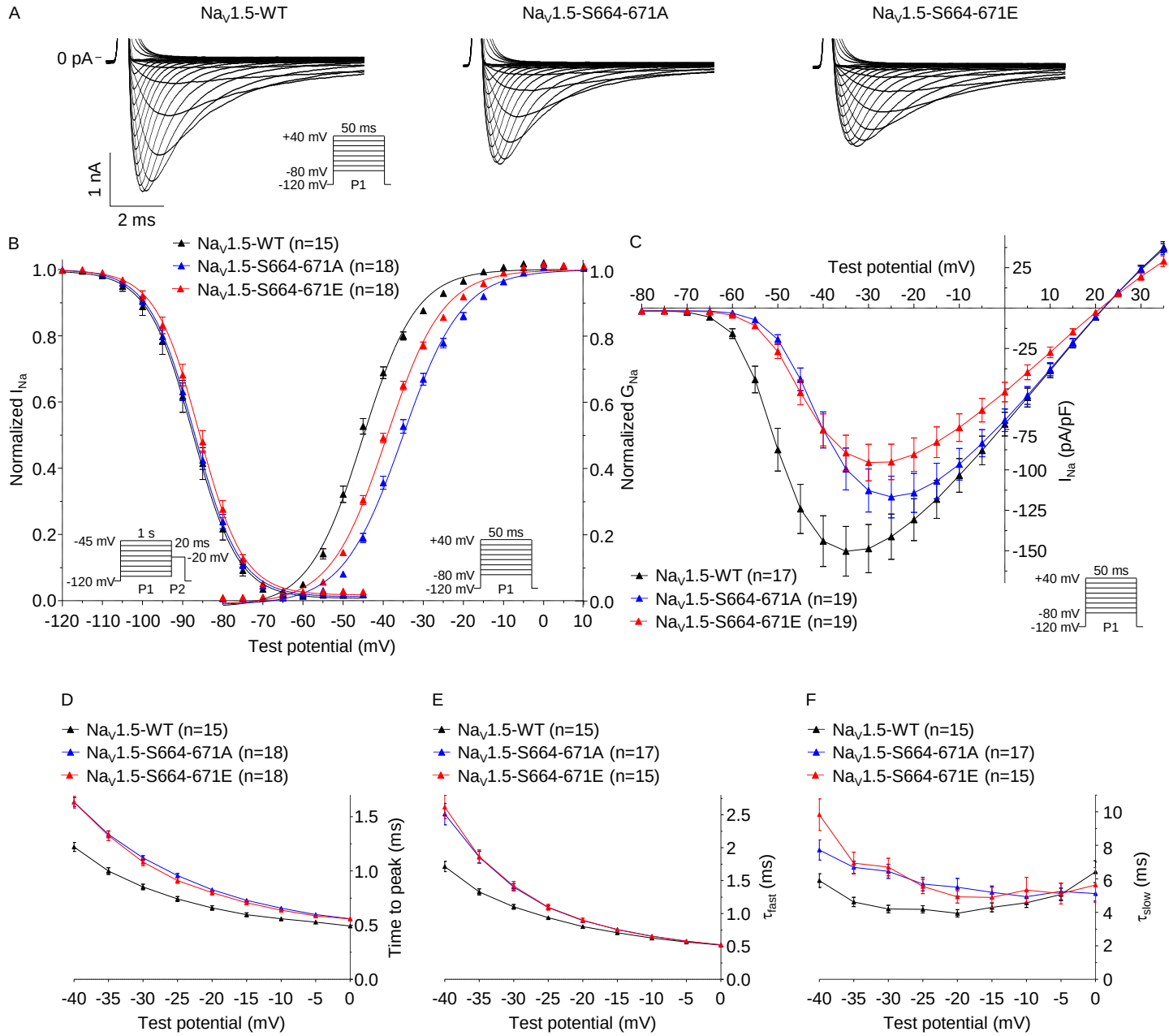

Figure 3.

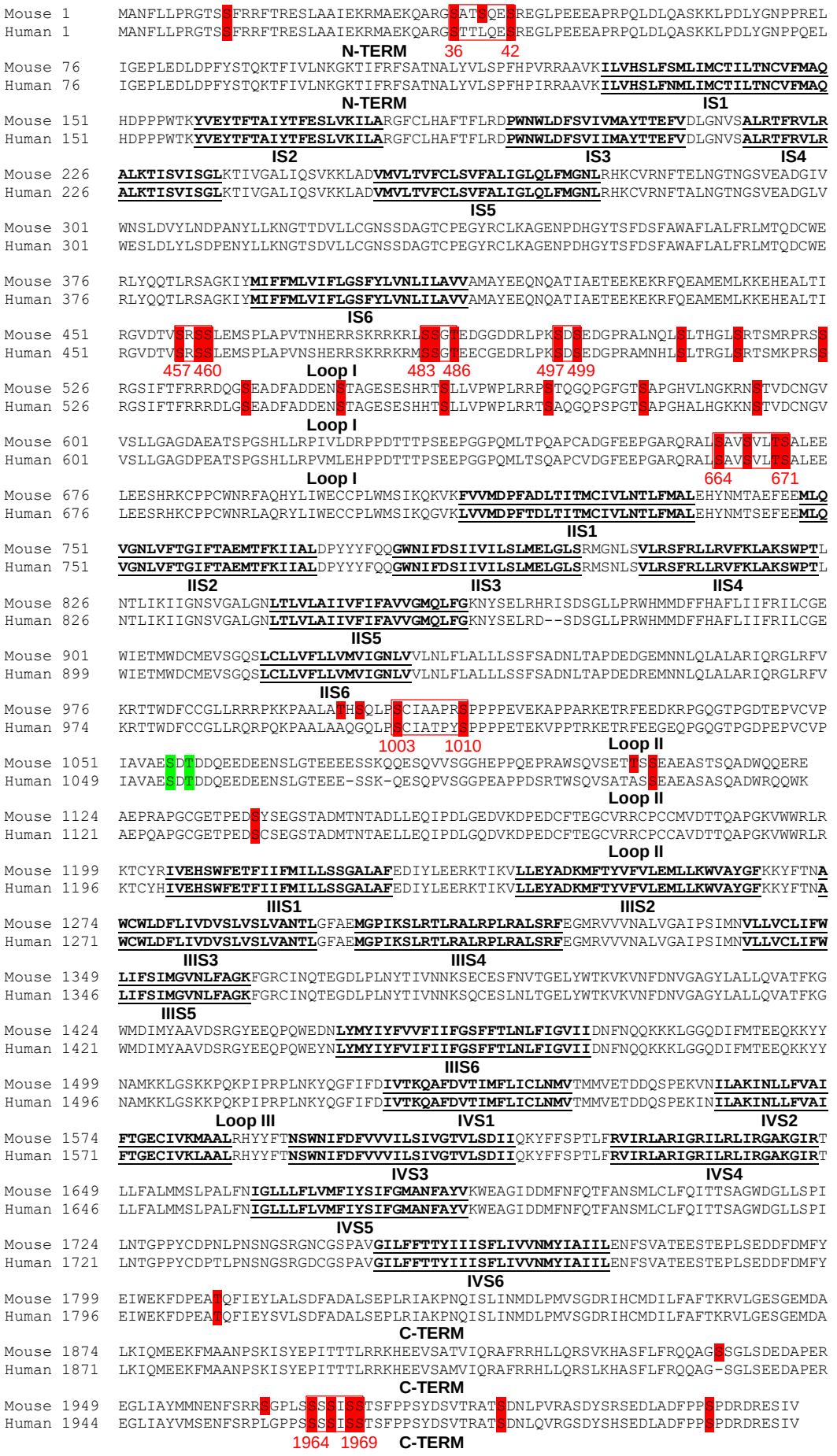

Figure 3 - Figure Supplement 1.

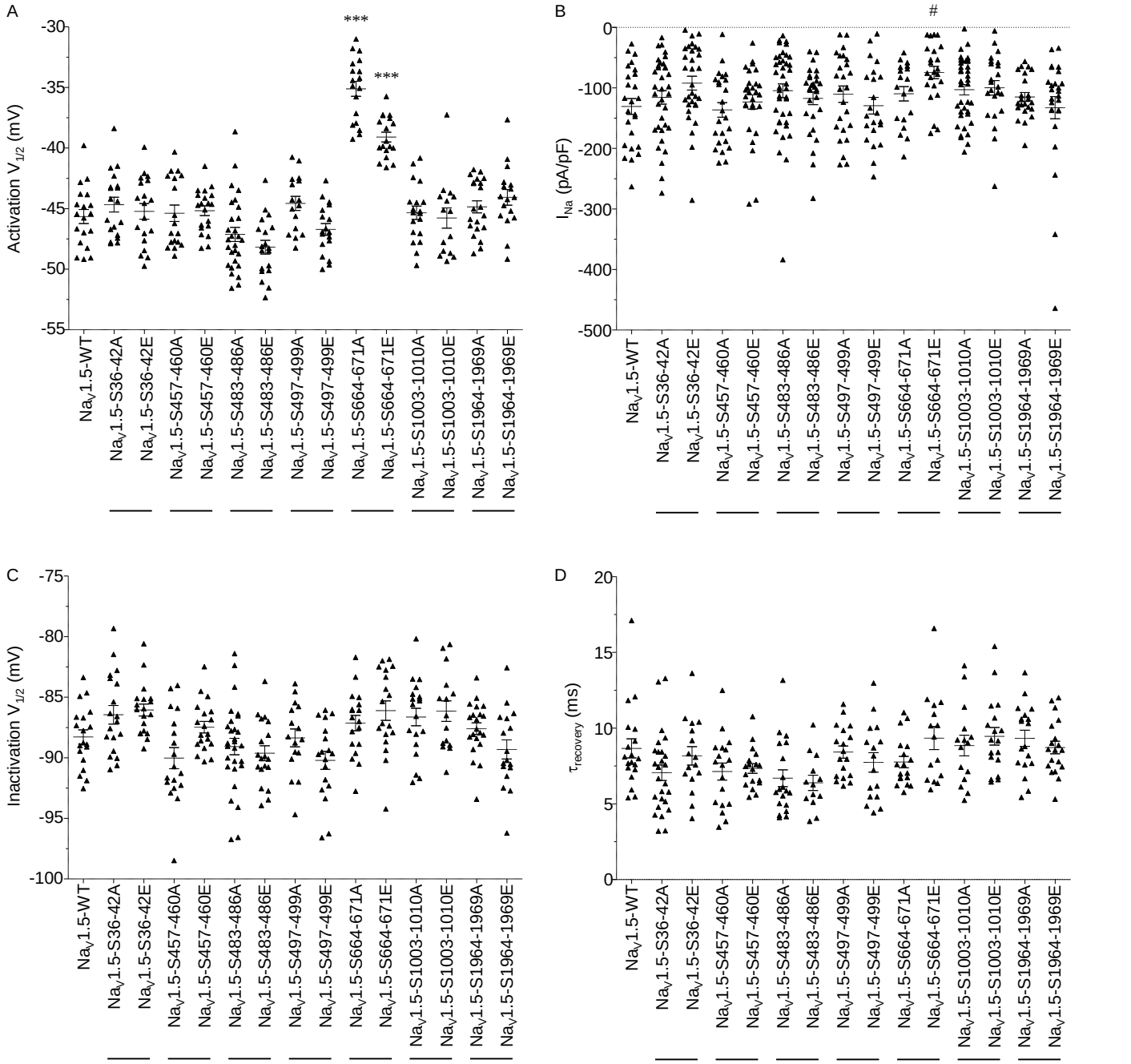

Figure 3 - Figure Supplement 2.

Figure 3 - Table Supplement 1. Current densities and properties of $Na_V1.5$ channels mutant for the phosphorylation clusters in transiently transfected HEK293 cells

	I_{Na} (pA/pF)	Time to peak (ms)	Time course of inactivation			Voltage-dependence of activation		Voltage-dependence of inactivation		Recovery from inactivation
			τ_{fast} (ms)	τ_{slow} (ms)	A_{fast}/A_{slow}	$V_{1/2}$ (mV)	k (mV)	$V_{1/2}$ (mV)	k (mV)	τ_{rec} (ms)
$Na_V1.5$-WT	-130.8 ± 13.1 (25)	0.60 ± 0.01 (19)	0.72 ± 0.02 (18)	3.6 ± 0.2 (18)	15.5 ± 1.0 (18)	-45.7 ± 0.6 (19)	6.8 ± 0.2 (19)	-88.3 ± 0.6 (19)	4.9 ± 0.1 (19)	8.7 ± 0.6 (19)
$Na_V1.5$-S36-42A	-115.7 ± 11.2 (35)	0.63 ± 0.02 (19)	0.75 ± 0.02 (19)	3.6 ± 0.2 (19)	13.3 ± 1.0 (19)	-44.7 ± 0.6 (19)	6.7 ± 0.1 (19)	-86.5 ± 0.8 (19)	4.9 ± 0.1 (19)	7.1 ± 0.6 (18)
$Na_V1.5$-S36-42E	-92.2 ± 11.4 (31)	0.59 ± 0.02 (19)	0.72 ± 0.02 (17)	3.5 ± 0.2 (17)	13.6 ± 1.9 (17)	-45.2 ± 0.6 (19)	6.6 ± 0.1 (19)	-86.1 ± 0.5 (19)	4.6 ± 0.1 (19)	7.3 ± 0.3 (18)
$Na_V1.5$-S457-460A	-136.5 ± 12.1 (24)	0.60 ± 0.01 (18)	0.75 ± 0.02 (18)	4.6 ± 0.4 (18)	15.6 ± 1.2 (18)	-45.4 ± 0.7 (18)	7.0 ± 0.2 (18)	-90.0 ± 0.9 (18)	5.2 ± 0.1 (18)	9.3 ± 0.5 (18)
$Na_V1.5$-S457-460E	-123.3 ± 11.6 (28)	0.60 ± 0.02 (20)	0.74 ± 0.02 (19)	3.7 ± 0.2 (19)	17.5 ± 1.8 (19)	-45.2 ± 0.4 (20)	6.8 ± 0.1 (20)	-87.5 ± 0.5 (19)	4.7 ± 0.1 (19)	8.7 ± 0.4 (19)
$Na_V1.5$-S483-486A	-104.7 ± 11.3 (40)	0.61 ± 0.02 (28)	0.61 ± 0.02 (26)	3.2 ± 0.1 (26)	12.7 ± 1.0 (26)	-47.1 ± 0.6 (28)	6.3 ± 0.2 (28)	-89.1 ± 0.7 (28)	5.0 ± 0.1 (28)	7.1 ± 0.5 (26)
$Na_V1.5$-S483-486E	-117.4 ± 10.4 (29)	0.55 ± 0.02 (19)	0.59 ± 0.02 (16)	2.9 ± 0.2 (16)	14.2 ± 1.2 (16)	-48.2 ± 0.6 (19)	6.3 ± 0.2 (19)	-89.6 ± 0.6 (19)	4.8 ± 0.1 (19)	8.2 ± 0.6 (16)
$Na_V1.5$-S497-499A	-110.5 ± 13.5 (25)	0.62 ± 0.02 (16)	0.76 ± 0.03 (12)	4.6 ± 0.4 (12)	18.0 ± 1.4 (12)	-44.6 ± 0.6 (16)	7.1 ± 0.1 (16)	-88.4 ± 0.7 (16)	4.8 ± 0.1 (16)	8.8 ± 0.7 (15)
$Na_V1.5$-S497-499E	-129.5 ± 13.8 (22)	0.56 ± 0.01 (18)	0.70 ± 0.02 (17)	3.8 ± 0.2 (17)	16.7 ± 1.0 (17)	-46.7 ± 0.5 (18)	7.2 ± 0.1 (18)	-90.2 ± 0.7 (18)	4.9 ± 0.1 (18)	9.5 ± 0.6 (18)
$Na_V1.5$-S664-671A	-109.8 ± 11.8 (19)	0.83 ± 0.02*** (18)	0.89 ± 0.02** (17)	5.5 ± 0.5* (17)	18.1 ± 1.2 (17)	-35.1 ± 0.6*** (18)	7.3 ± 0.1 (18)	-87.1 ± 0.6 (18)	5.4 ± 0.1 (18)	8.4 ± 0.4 (18)
$Na_V1.5$-S664-671E	-74.5 ± 10.2$^{\#}$ (23)	0.80 ± 0.02*** (18)	0.90 ± 0.03* (15)	4.9 ± 0.4 (15)	18.8 ± 1.9 (15)	-39.1 ± 0.4*** (18)	7.0 ± 0.1 (18)	-86.1 ± 0.8 (18)	5.1 ± 0.1 (18)	7.7 ± 0.6 (16)
$Na_V1.5$-S1003-1010A	-103.0 ± 8.5 (38)	0.62 ± 0.01 (19)	0.76 ± 0.02 (19)	4.2 ± 0.2 (19)	7.4 ± 0.7 (19)	-45.3 ± 0.5 (19)	6.5 ± 0.2 (19)	-86.6 ± 0.7 (19)	6.0 ± 0.2 (19)	6.7 ± 0.6 (19)
$Na_V1.5$-S1003-1010E	-99.9 ± 11.9 (23)	0.61 ± 0.01 (15)	0.74 ± 0.02 (15)	3.9 ± 0.1 (15)	7.8 ± 0.6 (15)	-45.8 ± 0.8 (15)	6.5 ± 0.2 (15)	-86.2 ± 0.8 (15)	5.6 ± 0.2 (15)	6.4 ± 0.5 (13)
$Na_V1.5$-S1964-1969A	-115.0 ± 7.4 (23)	0.63 ± 0.01 (21)	0.77 ± 0.02 (20)	4.1 ± 0.2 (20)	15.8 ± 0.9 (20)	-44.9 ± 0.5 (21)	6.6 ± 0.2 (21)	-87.6 ± 0.5 (21)	5.1 ± 0.1 (21)	7.8 ± 0.4 (18)
$Na_V1.5$-S1964-1969E	-132.8 ± 18.3 (26)	0.66 ± 0.02 (17)	0.81 ± 0.02 (15)	4.0 ± 0.2 (15)	13.9 ± 0.8 (15)	-44.1 ± 0.6 (17)	7.2 ± 0.2 (17)	-89.3 ± 0.8 (17)	4.9 ± 0.1 (17)	9.3 ± 0.8 (15)

The peak Na^+ current density (I_{Na}), time to peak, and time course of inactivation properties presented were determined from analyses of records obtained on depolarizations to -20 mV (HP=-120 mV). All values are means ± SEM. The number of cells analyzed is provided in parentheses. $^{\#}p<0.05$ *versus* $Na_V1.5$-WT; one-way ANOVA followed by the Dunnett's post-hoc test. *$p<0.05$, **$p<0.01$, ***$p<0.001$ *versus* $Na_V1.5$-WT; Kruskal-Wallis followed by the Dunn's post-hoc test.

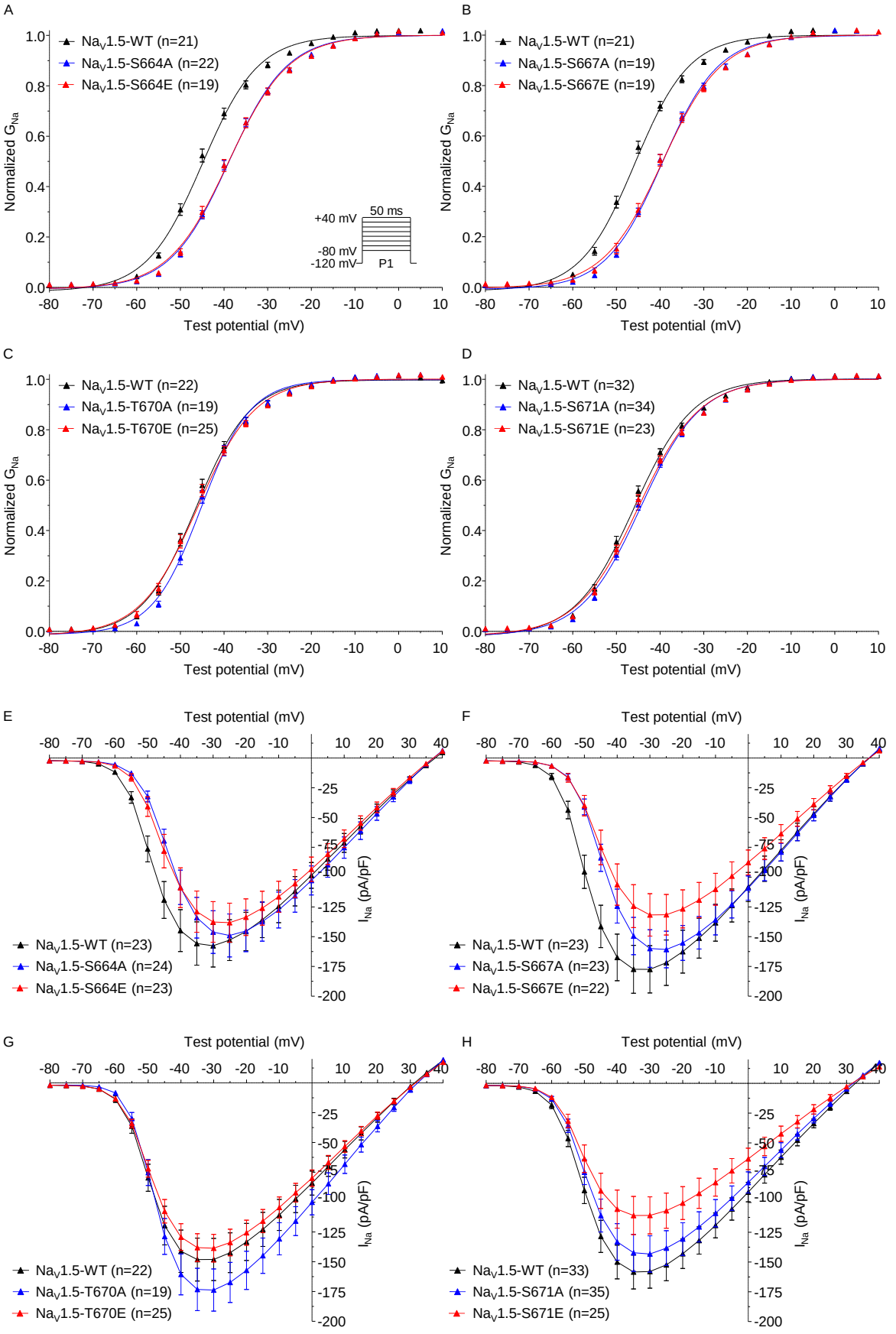

Figure 4.

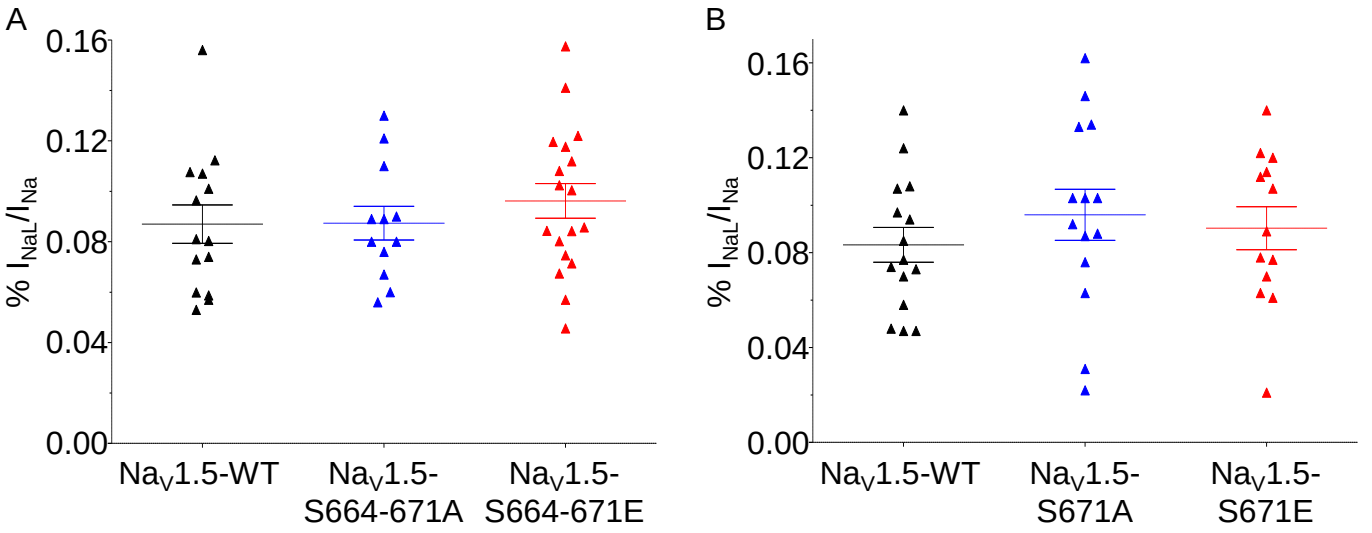

Figure 4 - Figure Supplement 1.

Figure 4 - Table Supplement 1. Current densities and properties of $Na_V1.5$ channels mutant for S664, S667, T670 and S671 in transiently transfected HEK293 cells

	I_{Na} (pA/pF)	Time to peak (ms)	Time course of inactivation			Voltage-dependence of activation		Voltage-dependence of inactivation		Recovery from inactivation
			τ_{fast} (ms)	τ_{slow} (ms)	A_{fast}/A_{slow}	$V_{1/2}$ (mV)	k (mV)	$V_{1/2}$ (mV)	k (mV)	τ_{rec} (ms)
$Na_V1.5$-WT	-162.5 ± 18.0 (23)	0.62 ± 0.02 (21)	0.75 ± 0.02 (19)	3.3 ± 0.2 (19)	13.8 ± 1.5 (19)	-45.7 ± 0.6 (21)	6.0 ± 0.2 (21)	-85.0 ± 0.6 (21)	4.7 ± 0.1 (21)	6.0 ± 0.4 (17)
$Na_V1.5$-S664A	-145.2 ± 17.4 (24)	0.75 ± 0.01* (22)	0.82 ± 0.02 (21)	4.1 ± 0.2 (21)	16.7 ± 1.4 (21)	-38.9 ± 0.5*** (22)	6.6 ± 0.1 (22)	-84.0 ± 0.7 (22)	4.8 ± 0.1 (22)	6.6 ± 0.6 (22)
$Na_V1.5$-S664E	-133.6 ± 15.4 (23)	0.73 ± 0.02 (19)	0.79 ± 0.03 (14)	3.3 ± 0.2 (14)	11.7 ± 1.1 (14)	-39.0 ± 0.6*** (19)	6.7 ± 0.1 (19)	-83.4 ± 0.8 (19)	4.7 ± 0.1 (19)	6.1 ± 0.5 (19)
$Na_V1.5$-S667A	-155.3 ± 14.6 (23)	0.75 ± 0.02 (19)	0.78 ± 0.03 (16)	3.9 ± 0.2 (16)	14.1 ± 1.0 (16)	-39.4 ± 0.5*** (19)	6.3 ± 0.2 (19)	-83.7 ± 0.6 (19)	4.9 ± 0.1 (19)	6.0 ± 0.4 (16)
$Na_V1.5$-S667E	-126.7 ± 16.0 (22)	0.76 ± 0.02* (19)	0.81 ± 0.02 (14)	4.0 ± 0.2 (14)	14.9 ± 1.3 (14)	-39.5 ± 0.7*** (19)	6.6 ± 0.1 (19)	-83.8 ± 0.9 (19)	4.7 ± 0.1 (19)	6.7 ± 0.7 (19)
$Na_V1.5$-T670A	-157.2 ± 16.0 (19)	0.63 ± 0.02 (19)	0.64 ± 0.02 (18)	3.0 ± 0.2 (18)	11.2 ± 1.5 (18)	-45.1 ± 0.6 (19)	5.4 ± 0.2 (19)	-86.9 ± 0.9 (16)	4.8 ± 0.1 (16)	8.4 ± 0.6 (14)
$Na_V1.5$-T670E	-125.7 ± 10.5 (25)	0.59 ± 0.02 (25)	0.70 ± 0.02 (22)	3.5 ± 0.4 (22)	14.3 ± 1.9 (22)	-46.2 ± 0.7 (25)	6.3 ± 0.2 (25)	-87.7 ± 1.0 (20)	4.6 ± 0.1 (20)	9.8 ± 1.0 (20)
$Na_V1.5$-S671A	-130.7 ± 13.7 (35)	0.54 ± 0.02 (34)	0.59 ± 0.02 (25)	2.3 ± 0.1 (25)	10.3 ± 0.9 (25)	-44.4 ± 0.5 (34)	6.5 ± 0.1 (34)	-84.9 ± 0.6 (32)	4.5 ± 0.1 (32)	5.6 ± 0.3 (30)
$Na_V1.5$-S671E	-100.6 ± 13.8# (25)	0.52 ± 0.01 (23)	0.65 ± 0.02 (11)	2.7 ± 0.3 (11)	9.9 ± 1.6 (11)	-45.0 ± 0.5 (23)	6.8 ± 0.1 (23)	-86.1 ± 0.5 (23)	4.4 ± 0.1 (23)	6.4 ± 0.3 (21)

The peak Na^+ current density (I_{Na}), time to peak, and time course of inactivation properties presented were determined from analyses of records obtained on depolarizations to -20 mV (HP=-120 mV). All values are means ± SEM. The number of cells analyzed is provided in parentheses. #p<0.05 *versus* $Na_V1.5$-WT; one-way ANOVA followed by the Dunnett's post-hoc test. *p<0.05, ***p<0.001 *versus* $Na_V1.5$-WT; Kruskal-Wallis followed by the Dunn's post-hoc test.

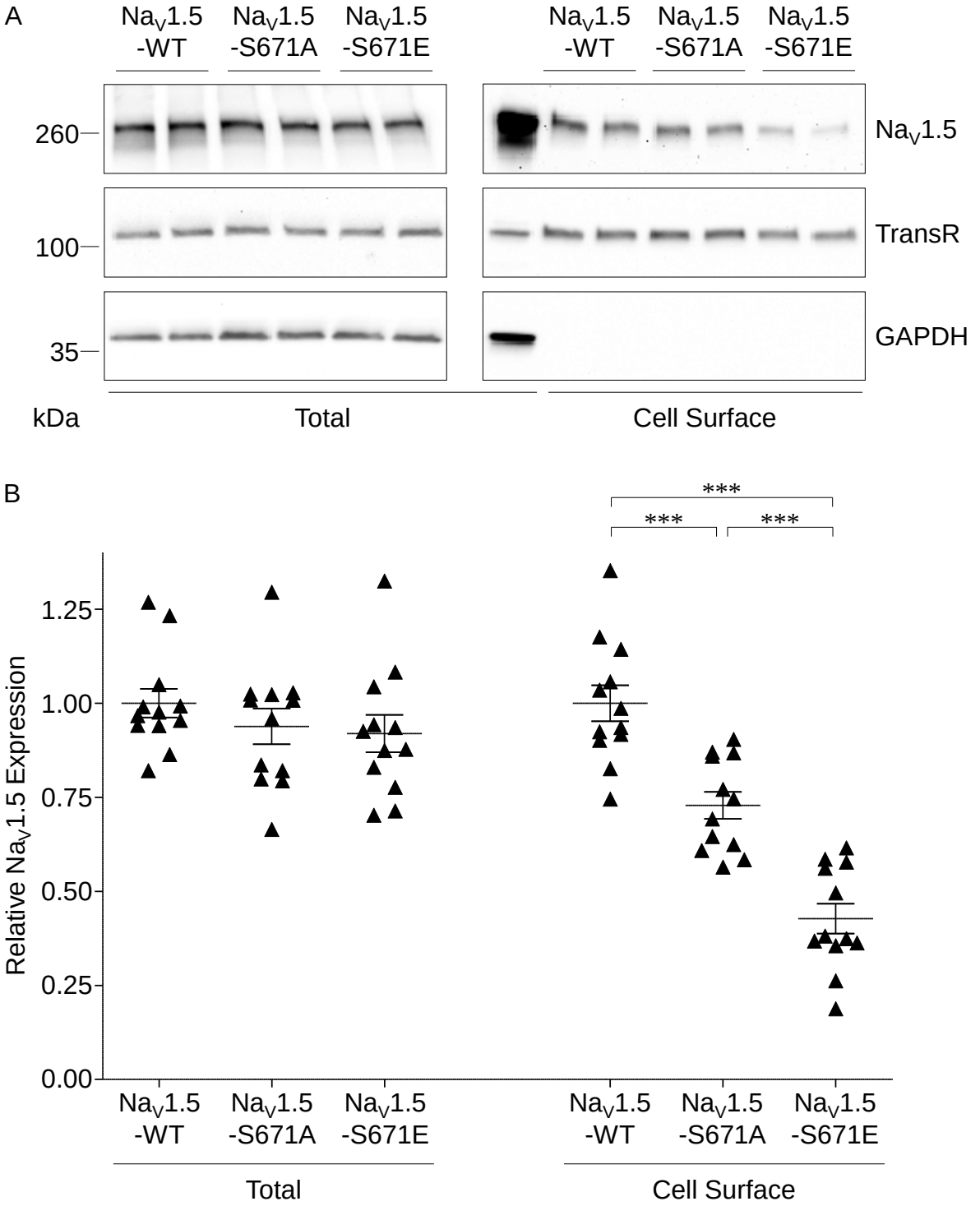

Figure 5.

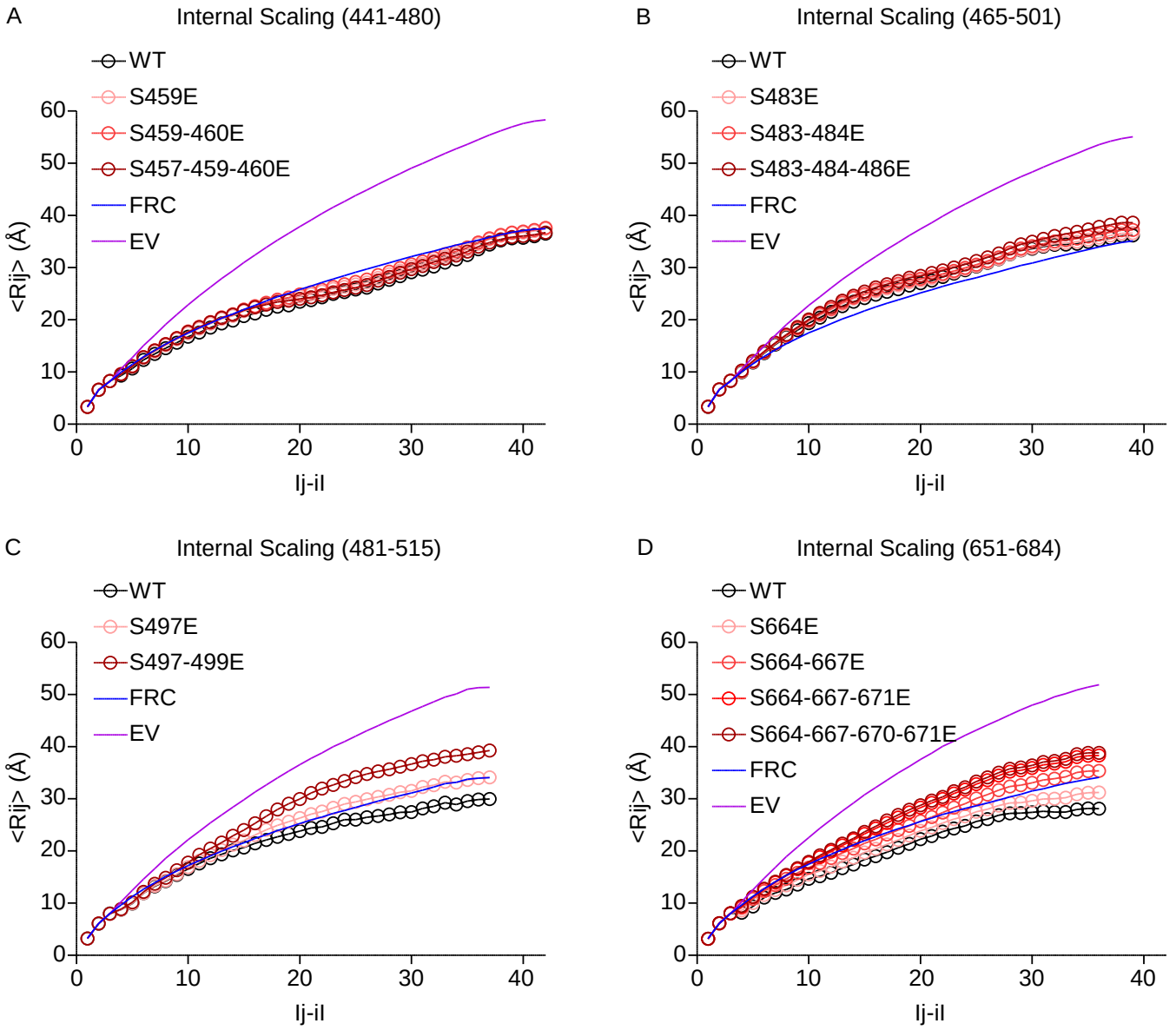

Figure 6.

Scan 6678, m/z=560.2791, z=2, -10lgP=21.64, ppm=0.0 (pS12)

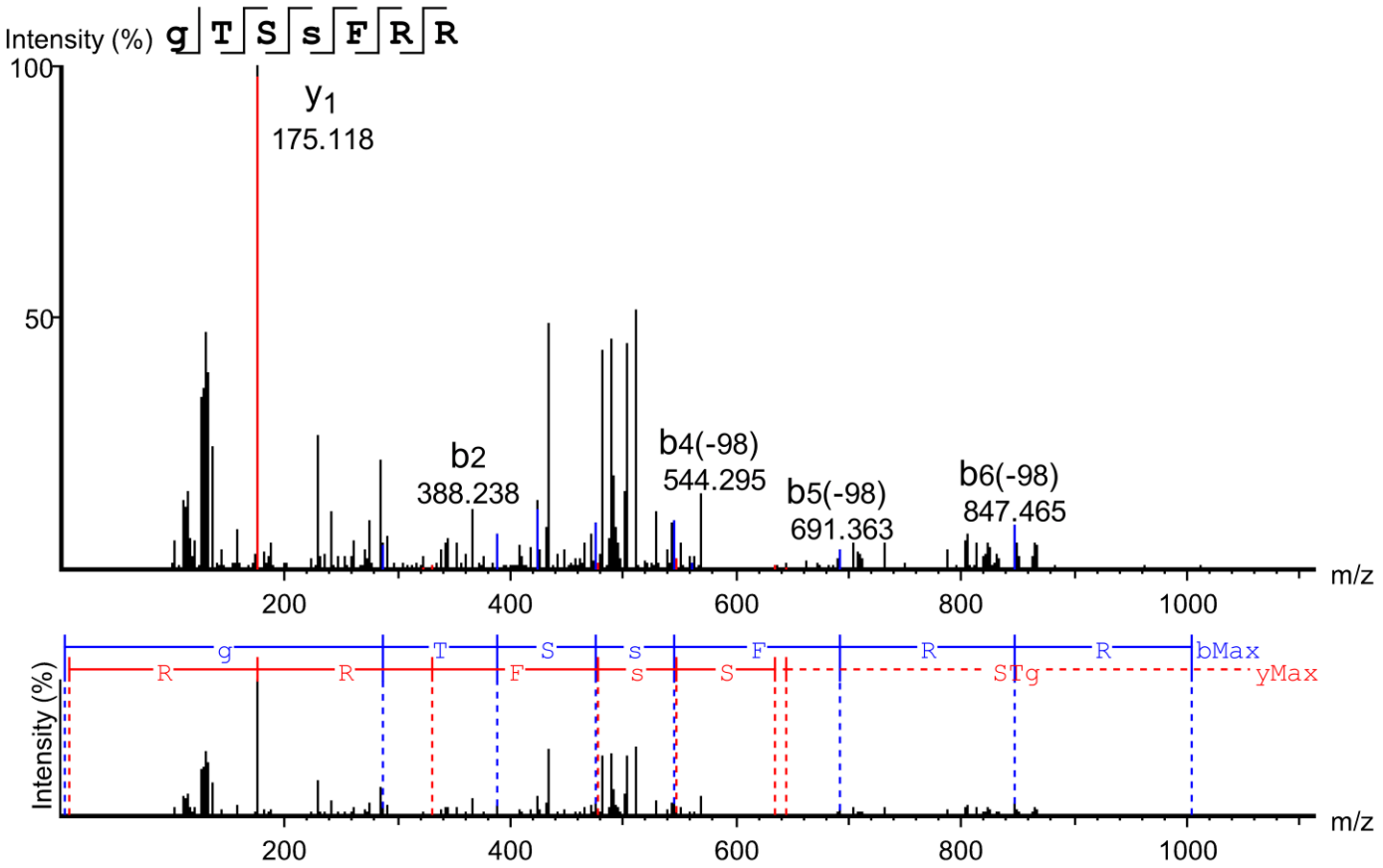

Table 2 - Figure Supplement 1.

Scan 4234, m/z=616.2795, z=2, -10lgP=32.06, ppm=0.1 (pS36)

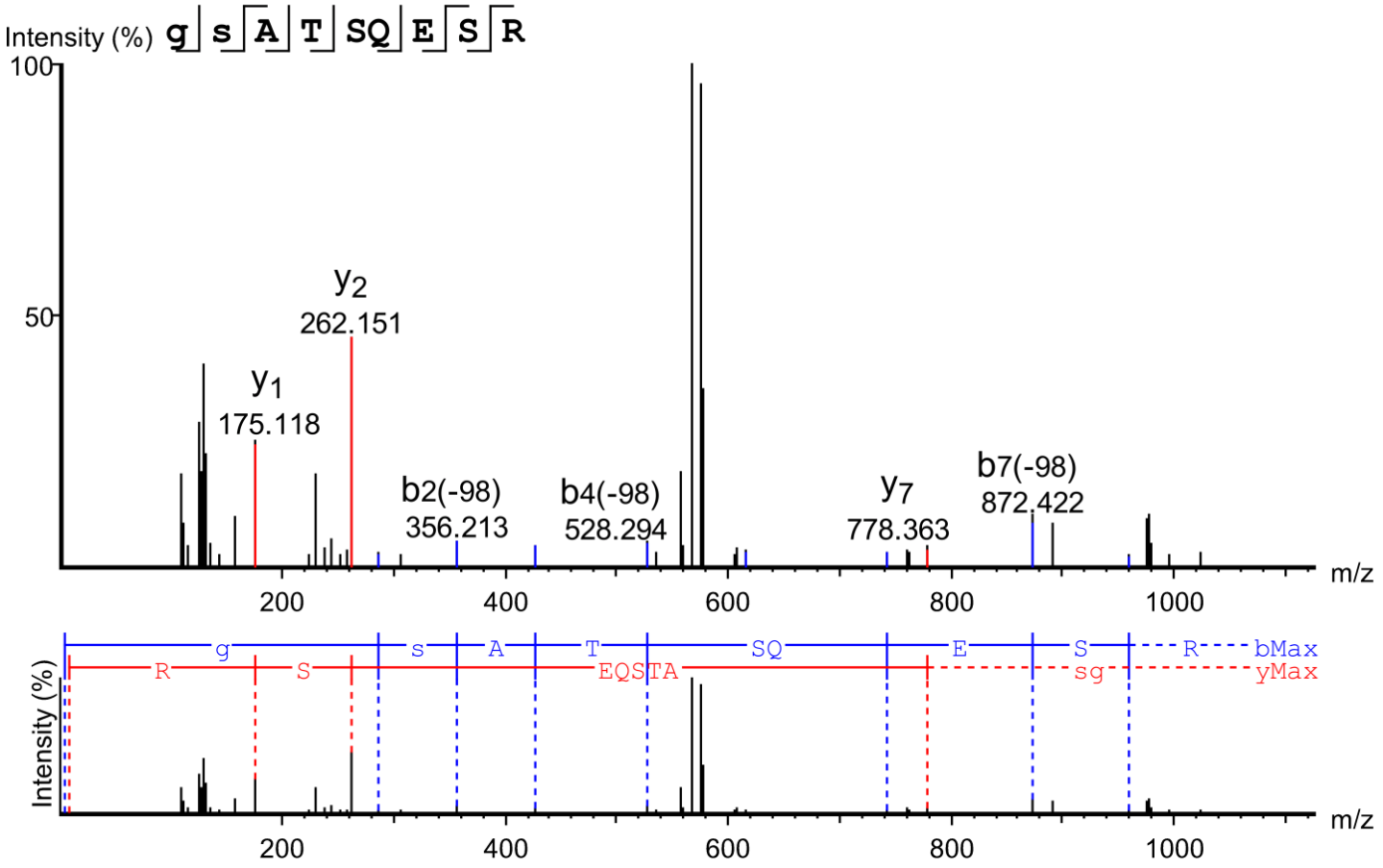

Table 2 - Figure Supplement 1.

Scan 42120, m/z=887.9468, z=4, -10lgP=73.05, ppm=0.6 (pS42)

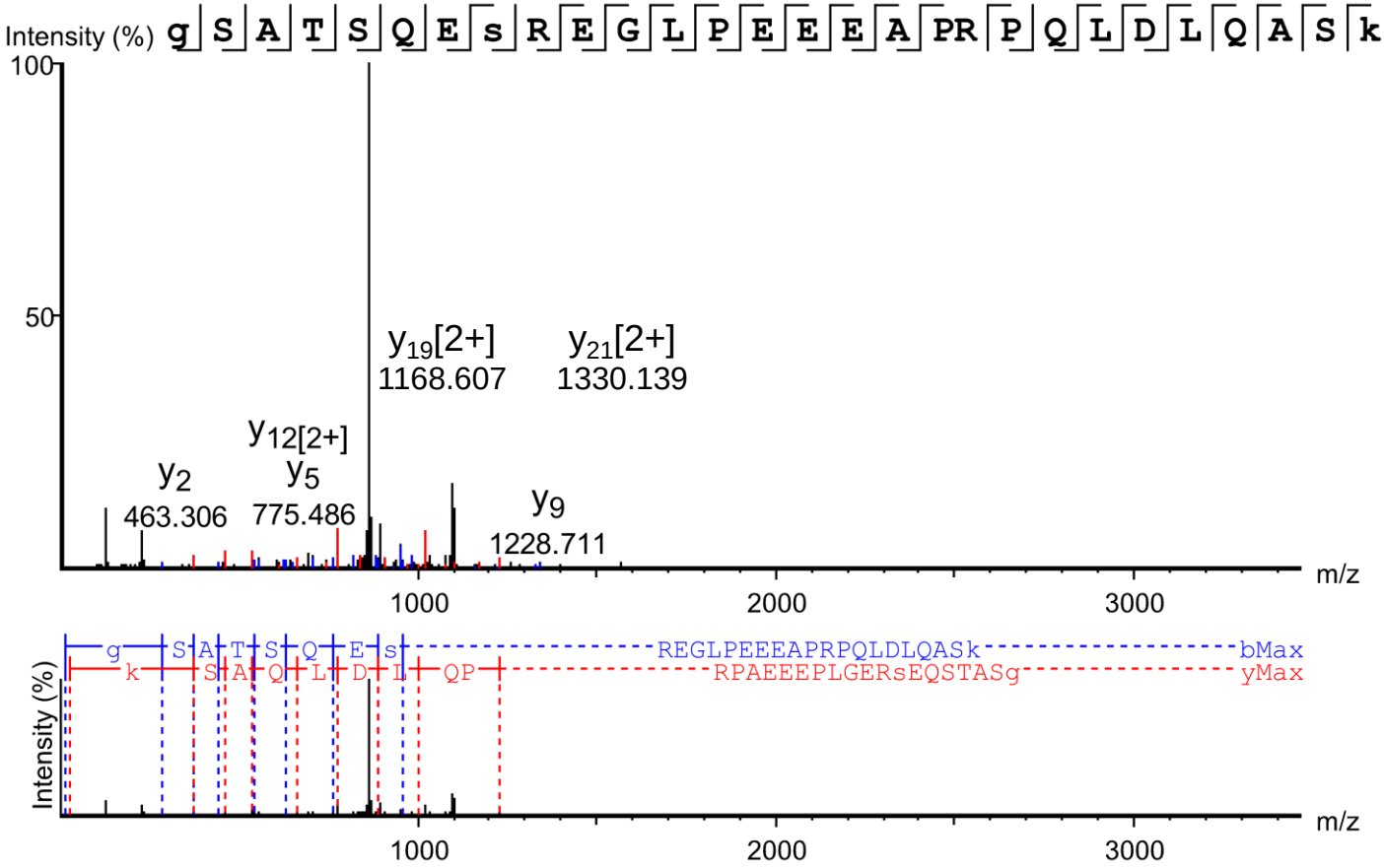

Table 2 - Figure Supplement 1.

Scan 49741, m/z=907.9366, z=4, -10lgP=68.43, ppm=-1.4 (pS39 + pS42)

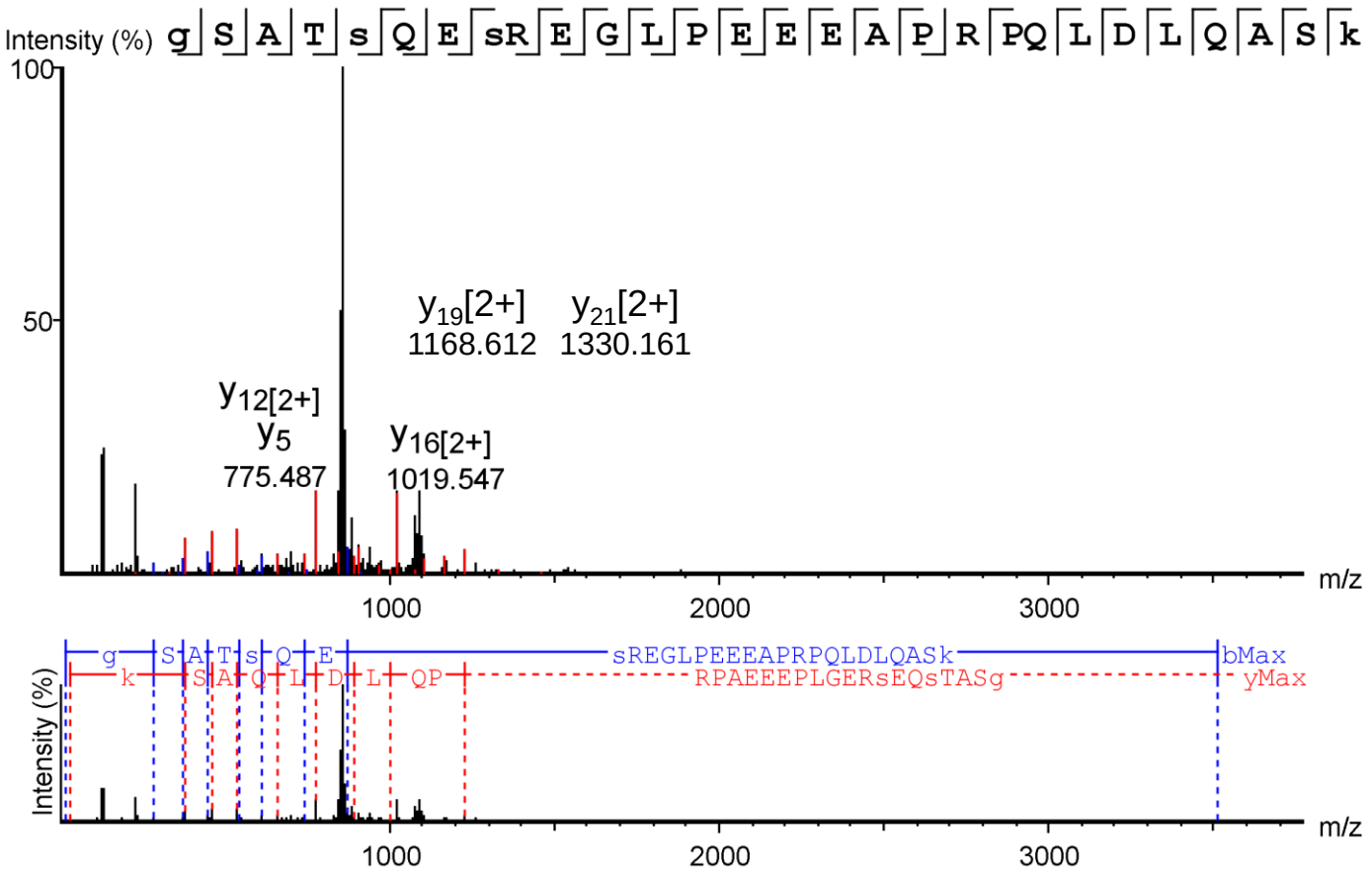

Table 2 - Figure Supplement 1.

Scan 51767, m/z=957.7820, z=3, -10lgP=77.13, ppm=0.1 - pS457 (+ pS459 or pS460)

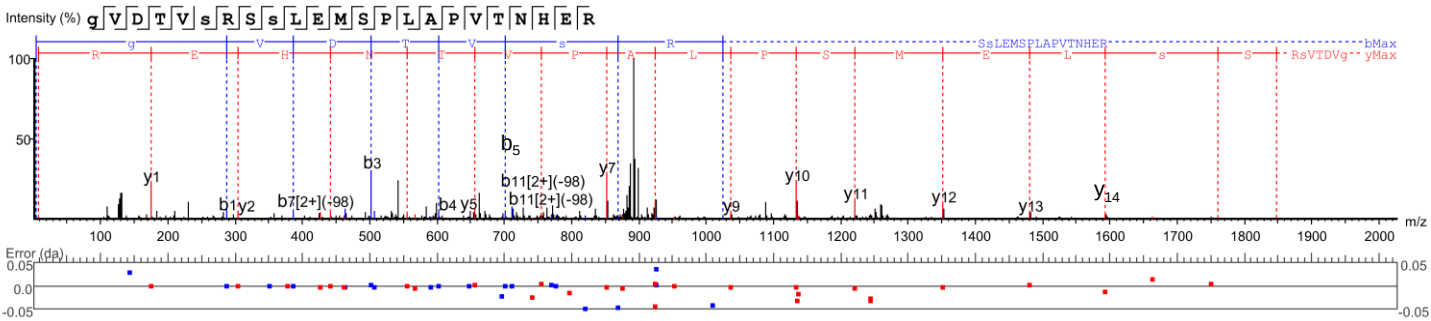

Table 2 - Figure Supplement 1.

Scan 52470, m/z=958.1167, z=3, -10lgP=41.49, ppm=7.1 (pS459 + pS460)

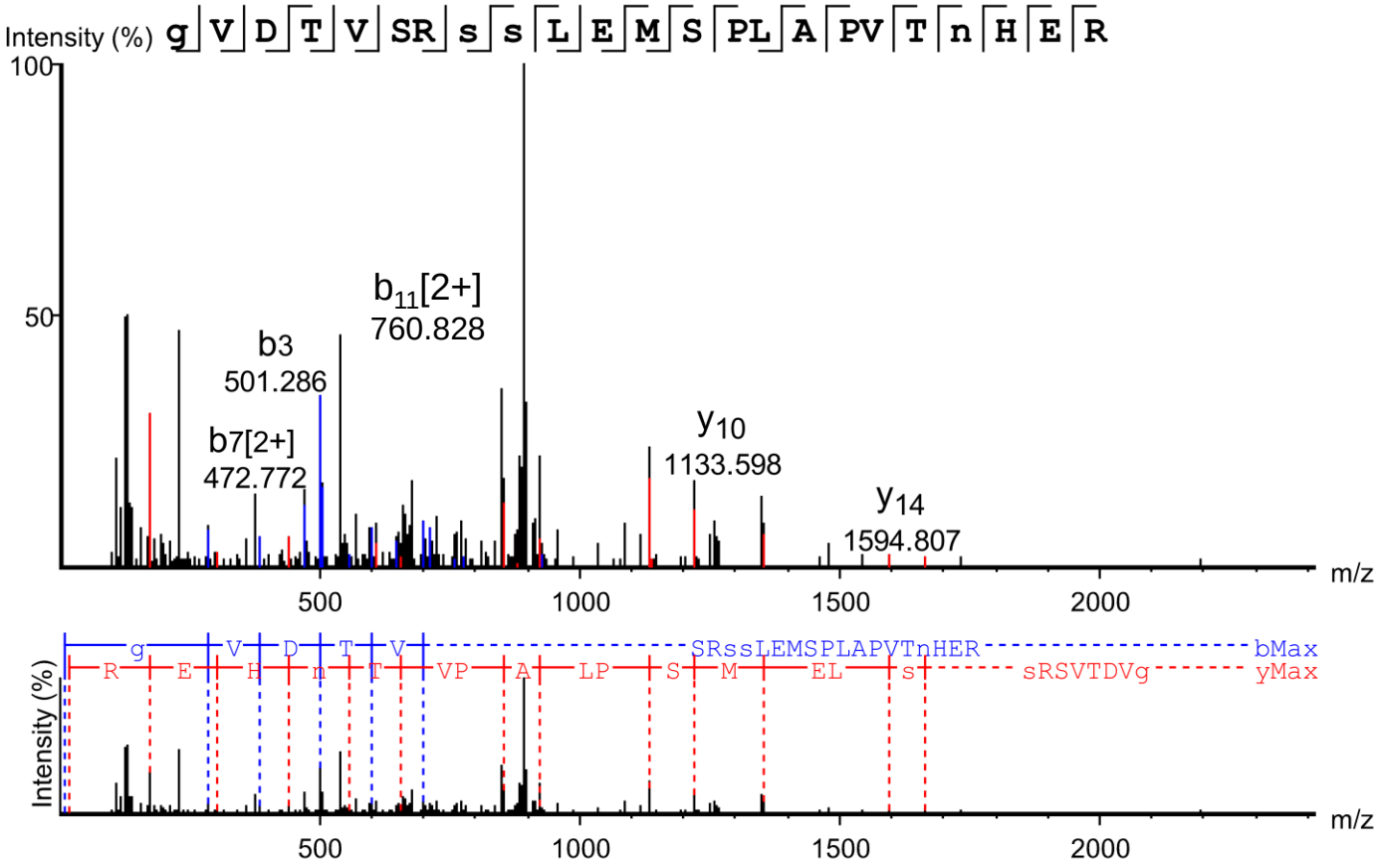

Table 2 - Figure Supplement 1.

Scan 46779, m/z=1039.0032, z=2, -10lgP=61.17, ppm=0.2 (pS460)

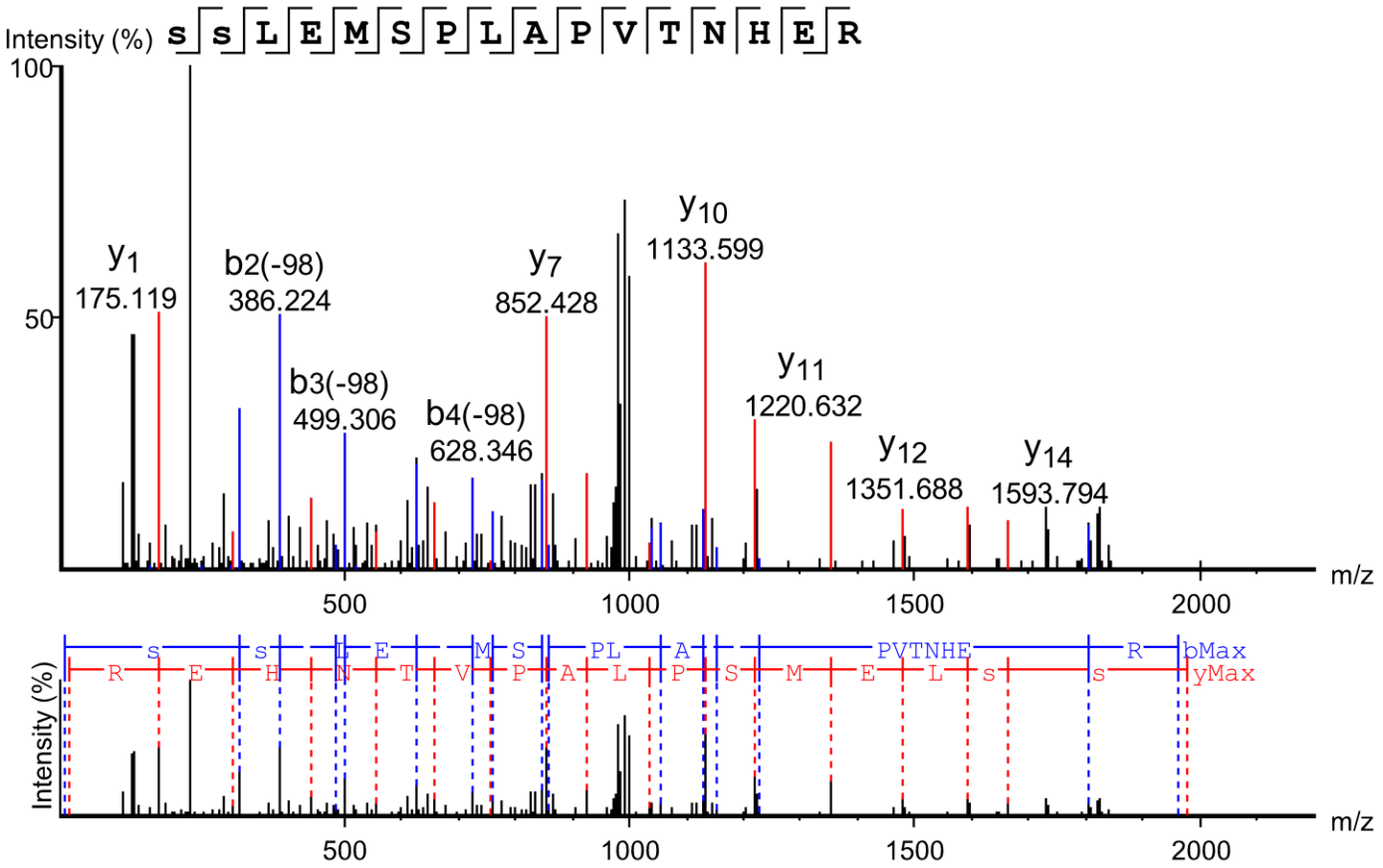

Table 2 - Figure Supplement 1.

Scan 26433, m/z=561.0378, z=4, -10lgP=52.36, ppm=0.7 (pS483)

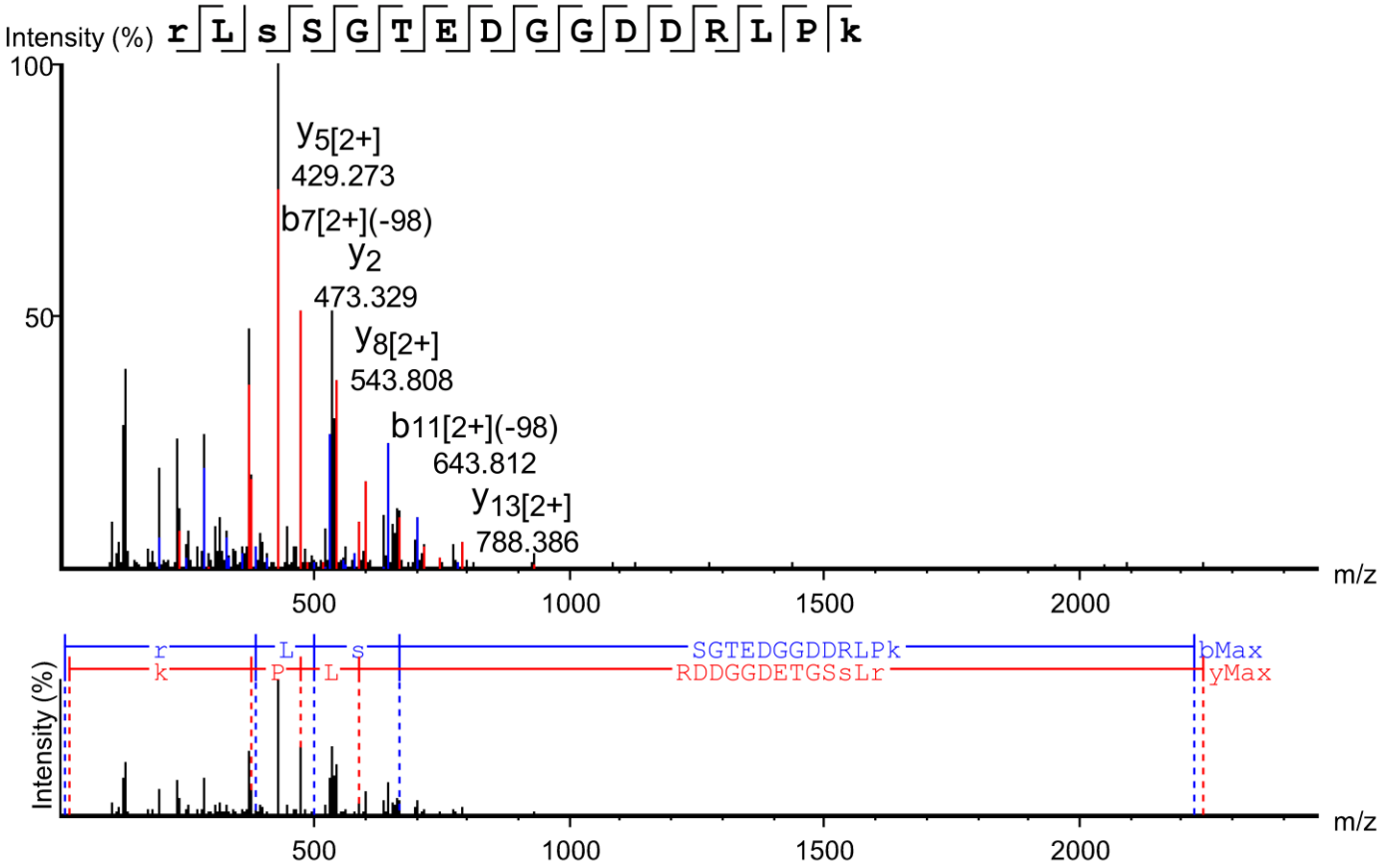

Table 2 - Figure Supplement 1.

Scan 22284, m/z=759.3195, z=2, -10lgP=45.74, ppm=0.0 (pS484)

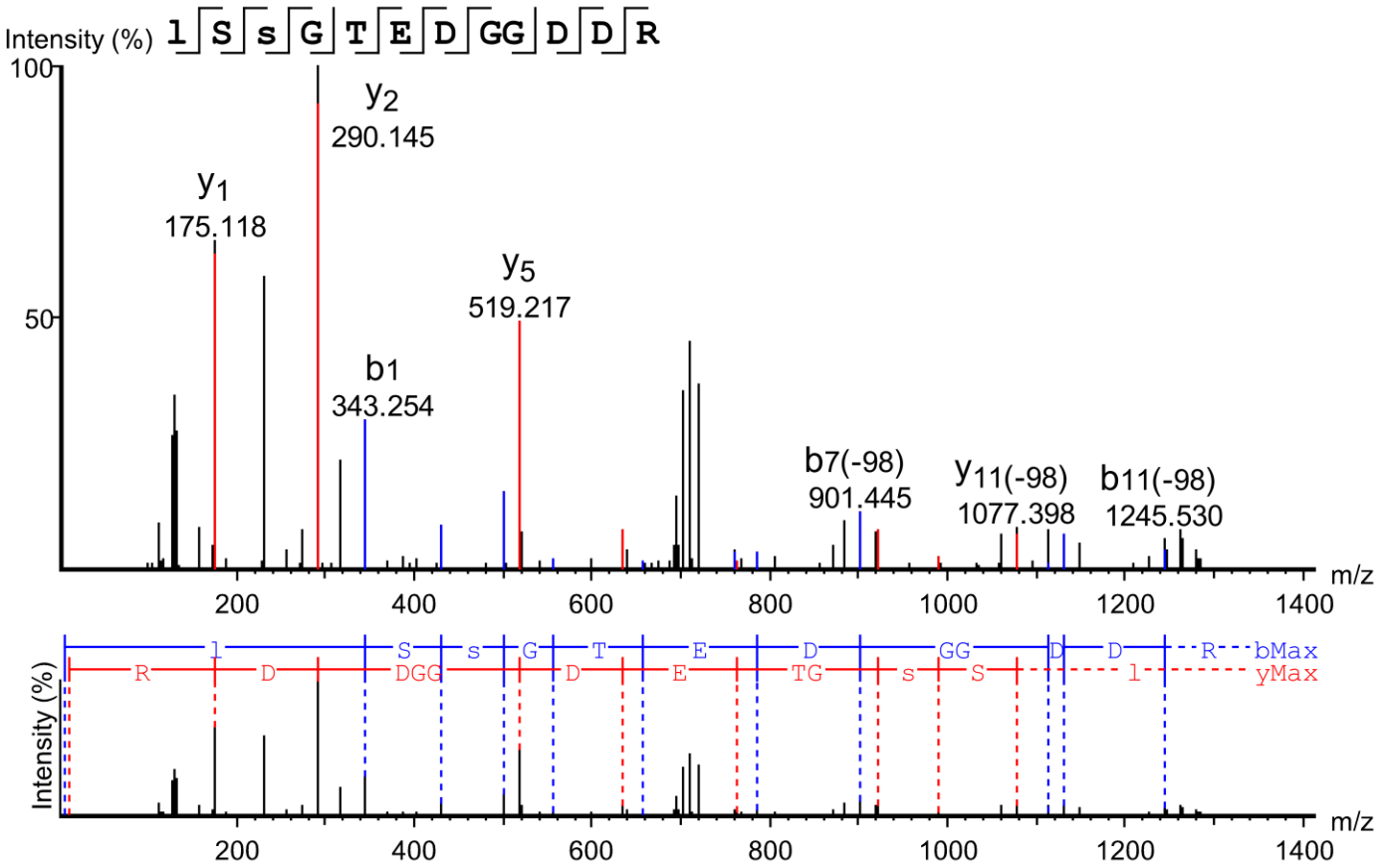

Table 2 - Figure Supplement 1.

Scan 26141, m/z=628.9735, z=3, -10lgP=21.92, ppm=-2.3 (pT486)

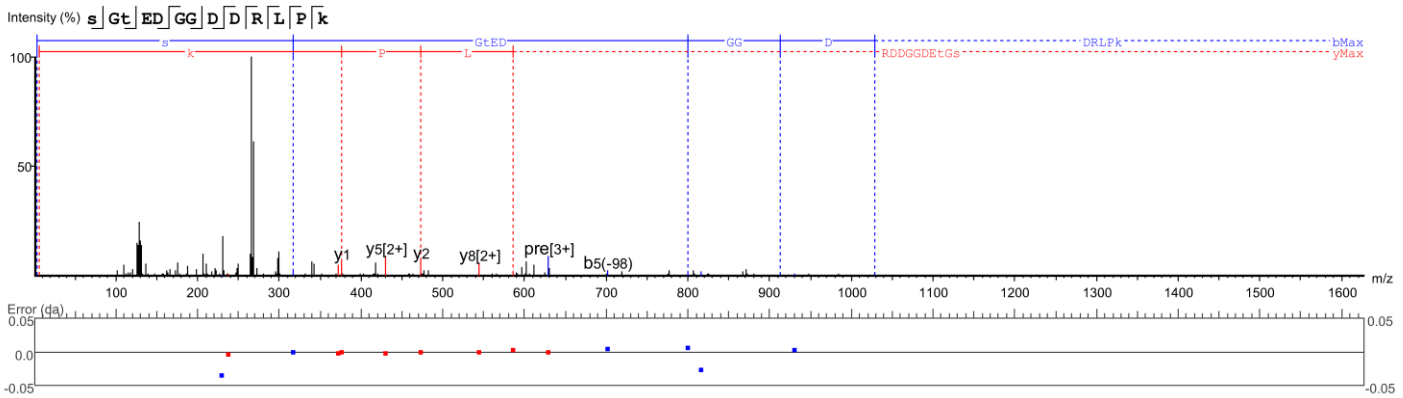

Table 2 - Figure Supplement 1.

Scan 29037, m/z=536.4764, z=5, -10lgP=62.95, ppm=0.5 (pS483 + pS484)

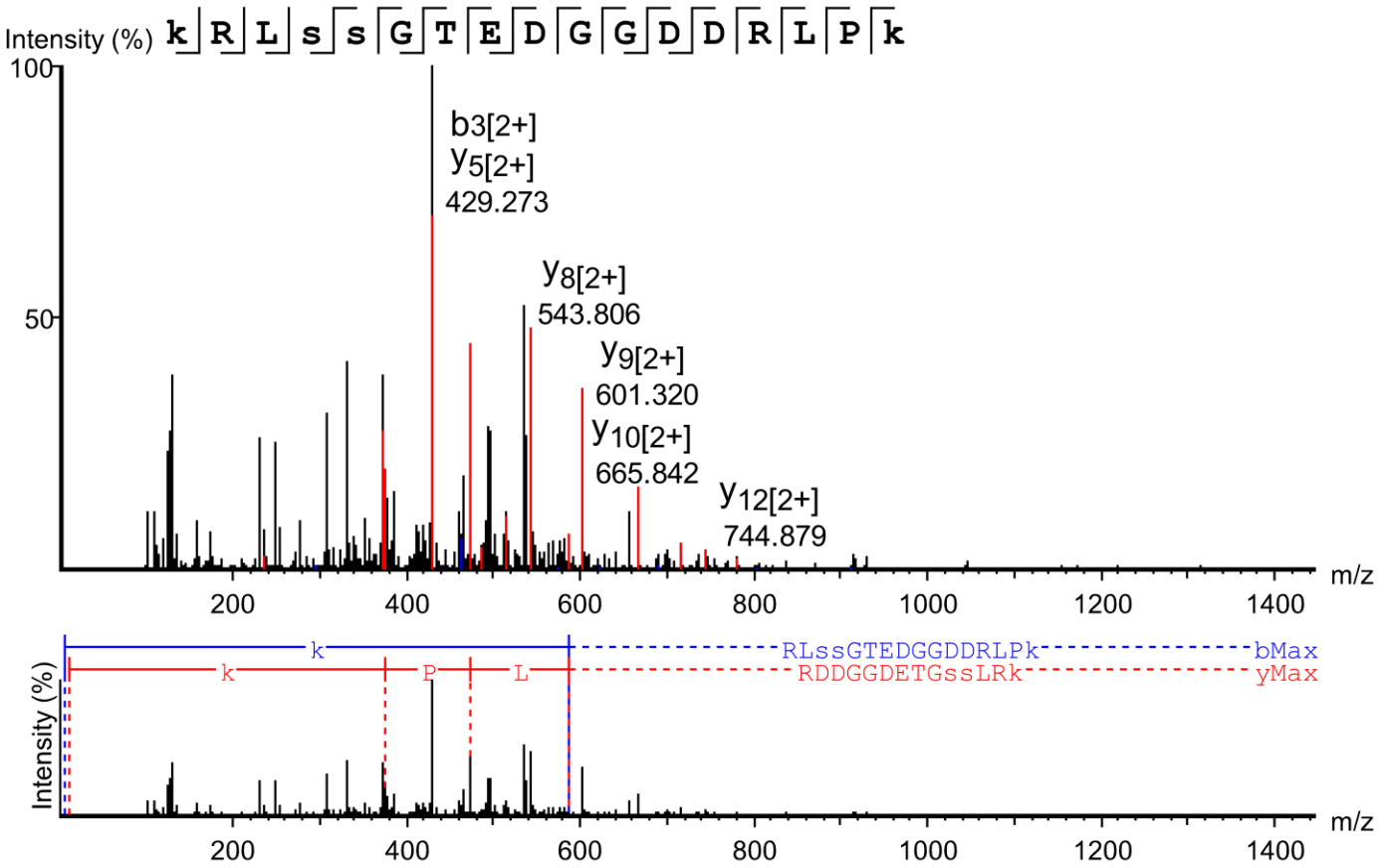

Table 2 - Figure Supplement 1.

Scan 29957, m/z=732.8451, z=4, -10lgP=60.24, ppm=-1.3 (pS497)

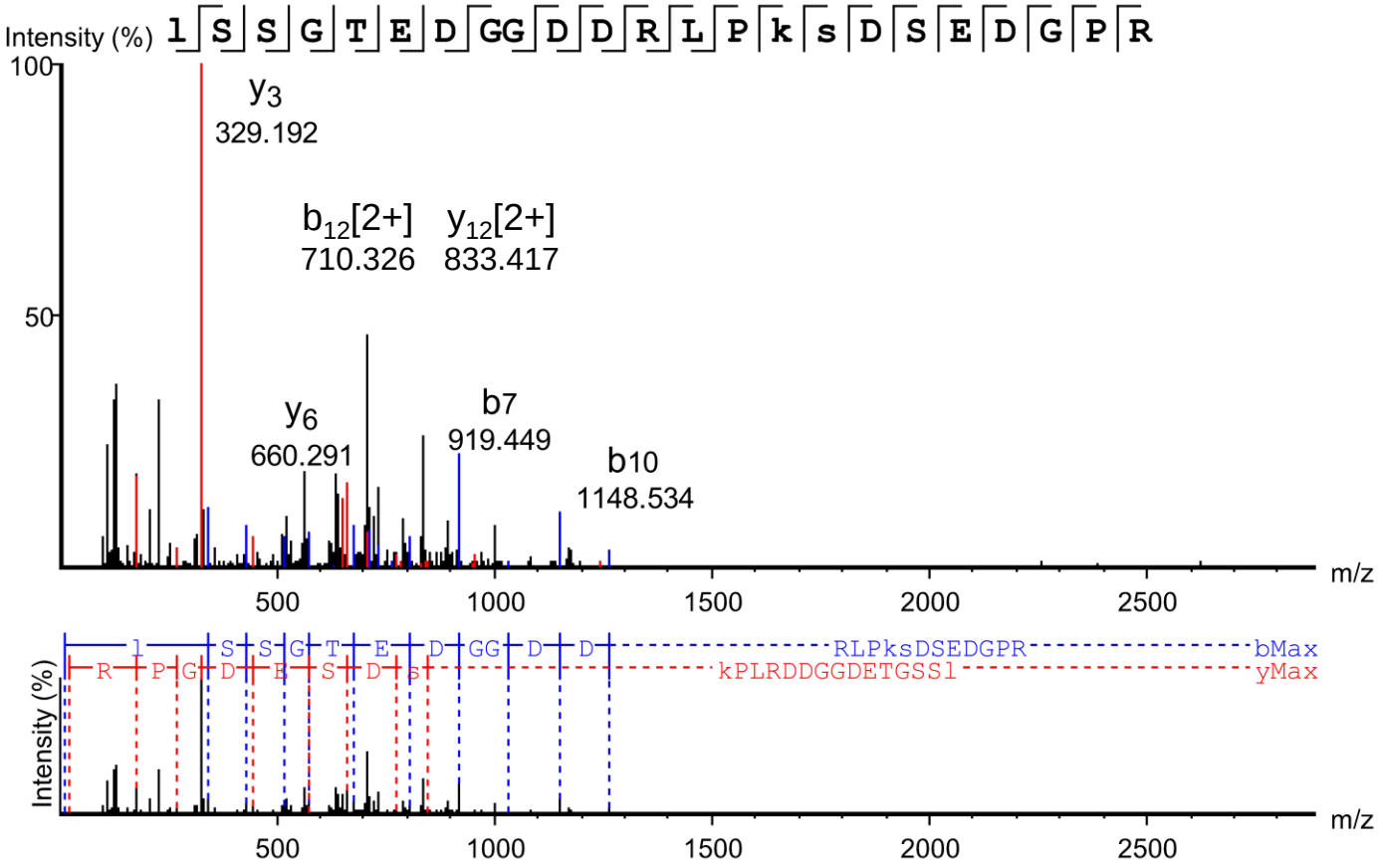

Table 2 - Figure Supplement 1.

Scan 27780, m/z=791.8616, z=4, -10lgP=40.10, ppm=-1.6 (pS483 + pS497)

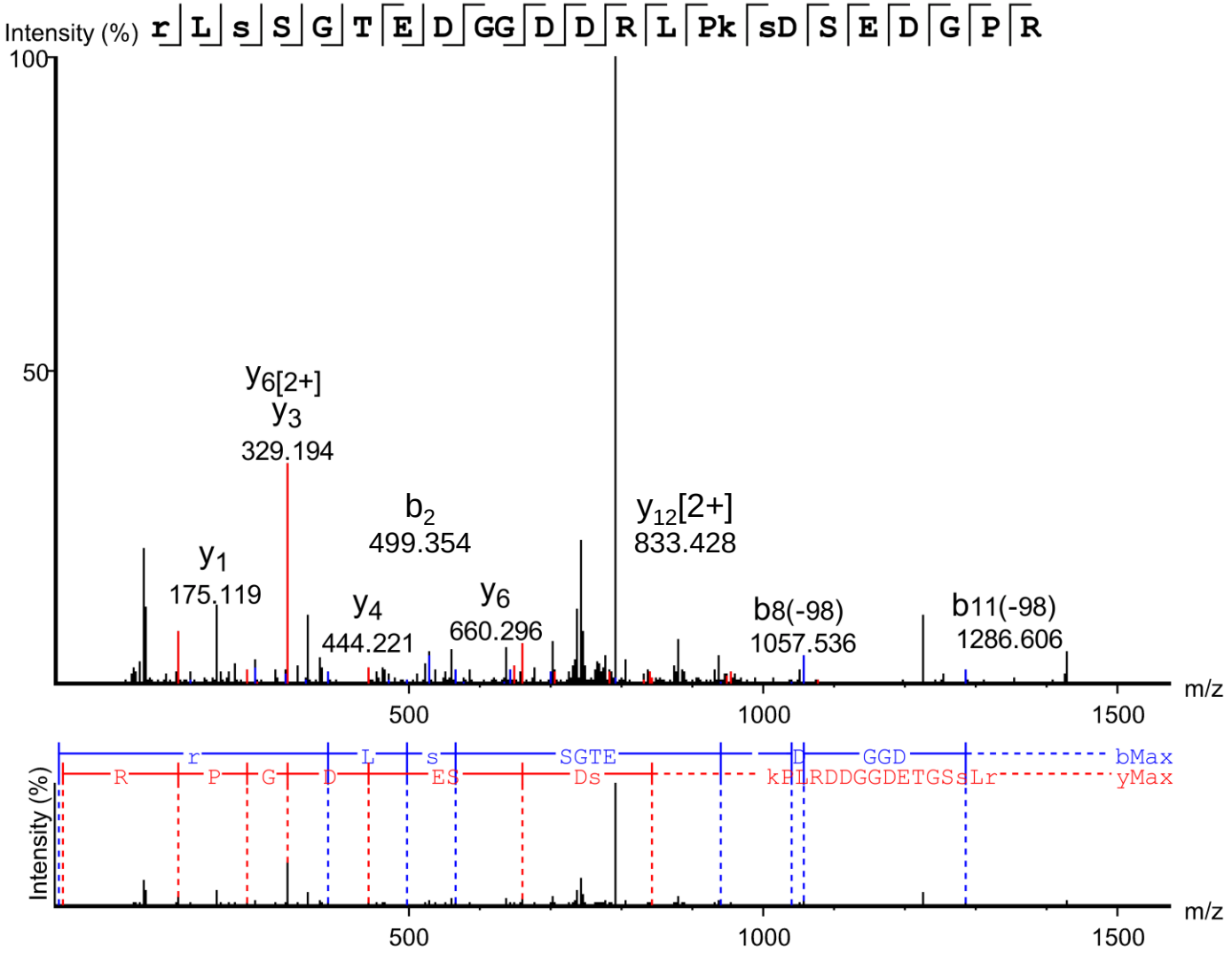

Table 2 - Figure Supplement 1.

Scan 36168, m/z=1003.4476, z=3, -10lgP=54.82, ppm=-0.1 (pS484 + pS497)

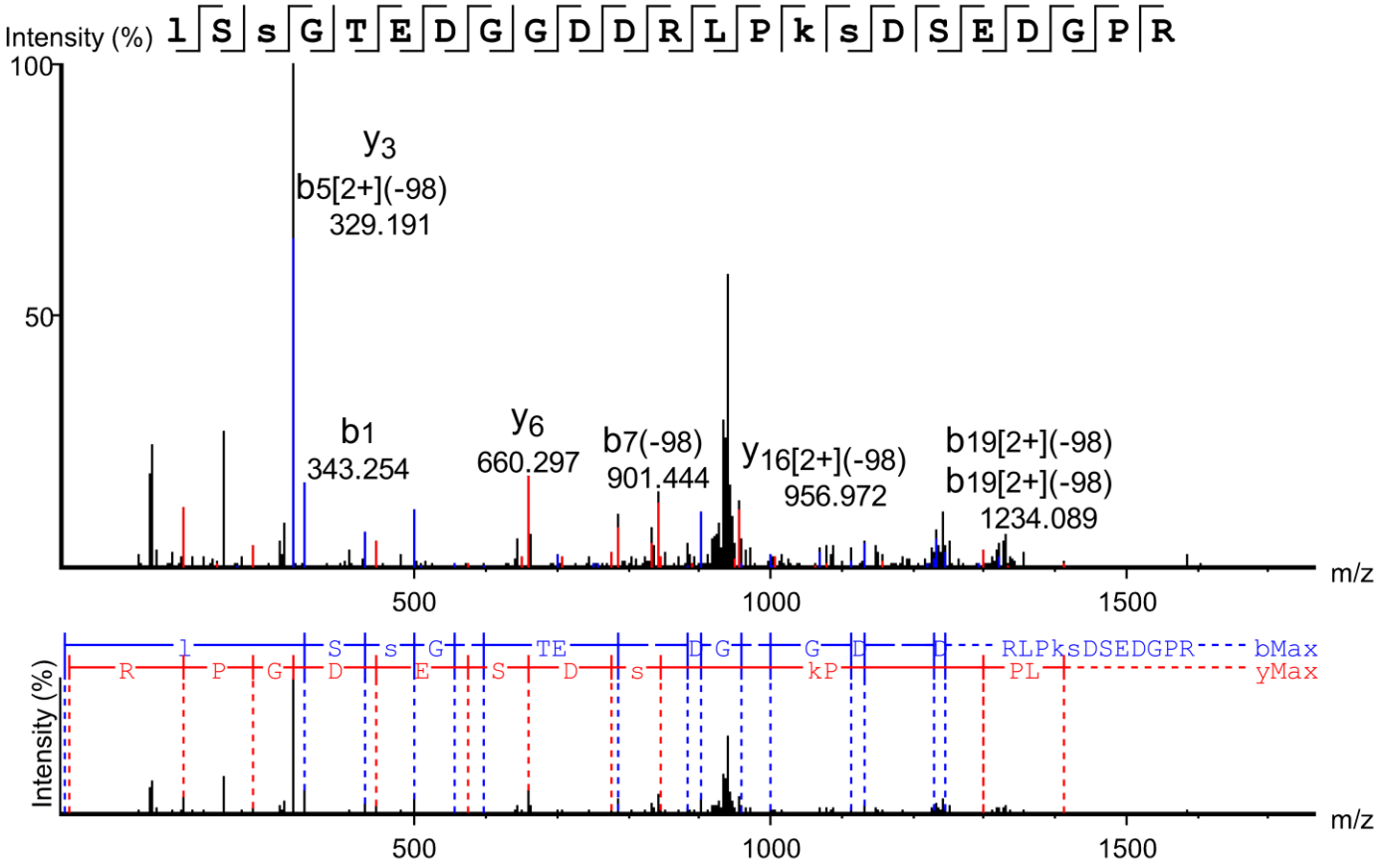

Table 2 - Figure Supplement 1.

Scan 7929, m/z=586.2448, z=2, -10lgP=41.97, ppm=-0.5 (pS499)

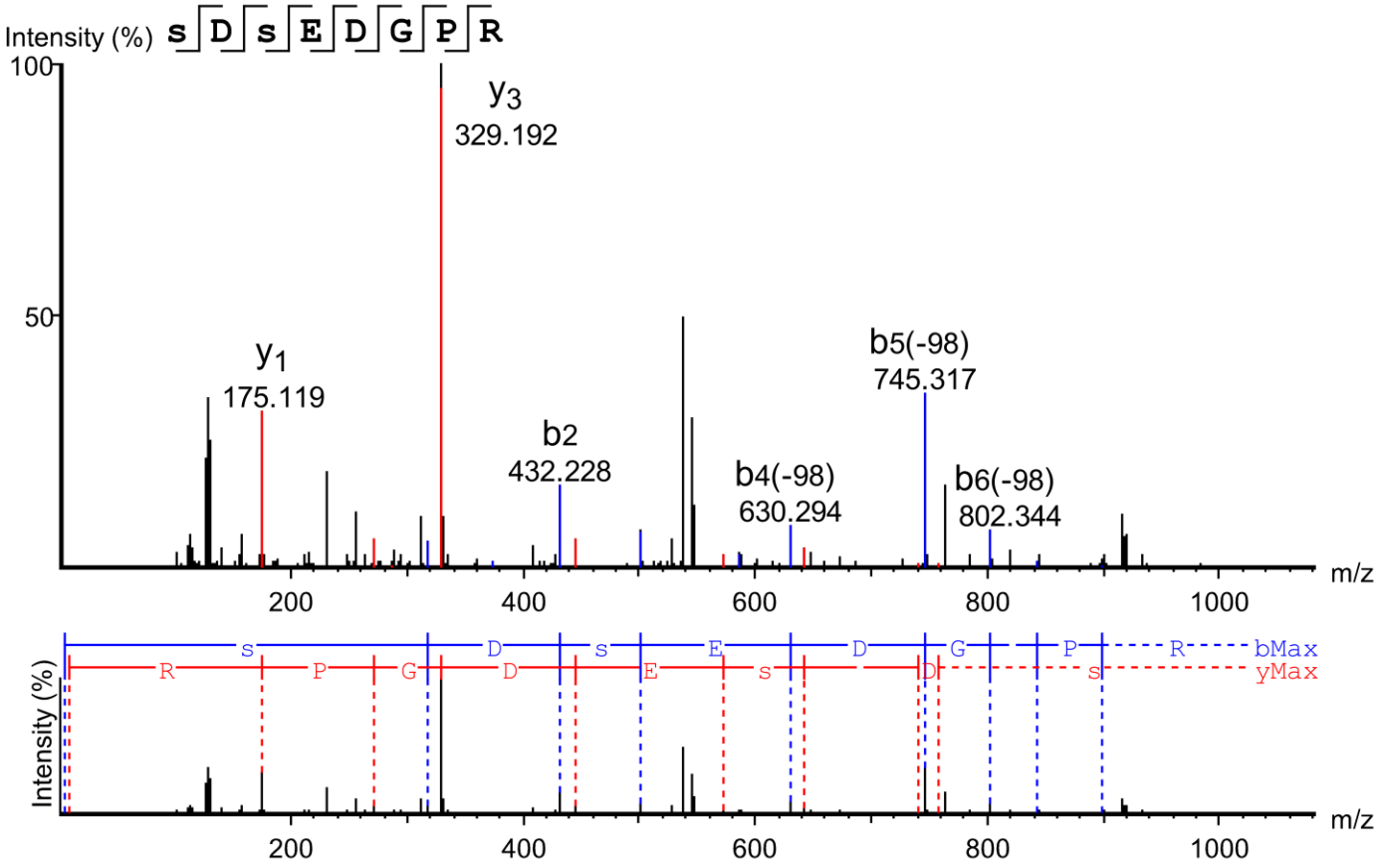

Table 2 - Figure Supplement 1.

Scan 46112, m/z=573.6431, z=3, -10lgP=51.77, ppm=-0.2 (pS510)

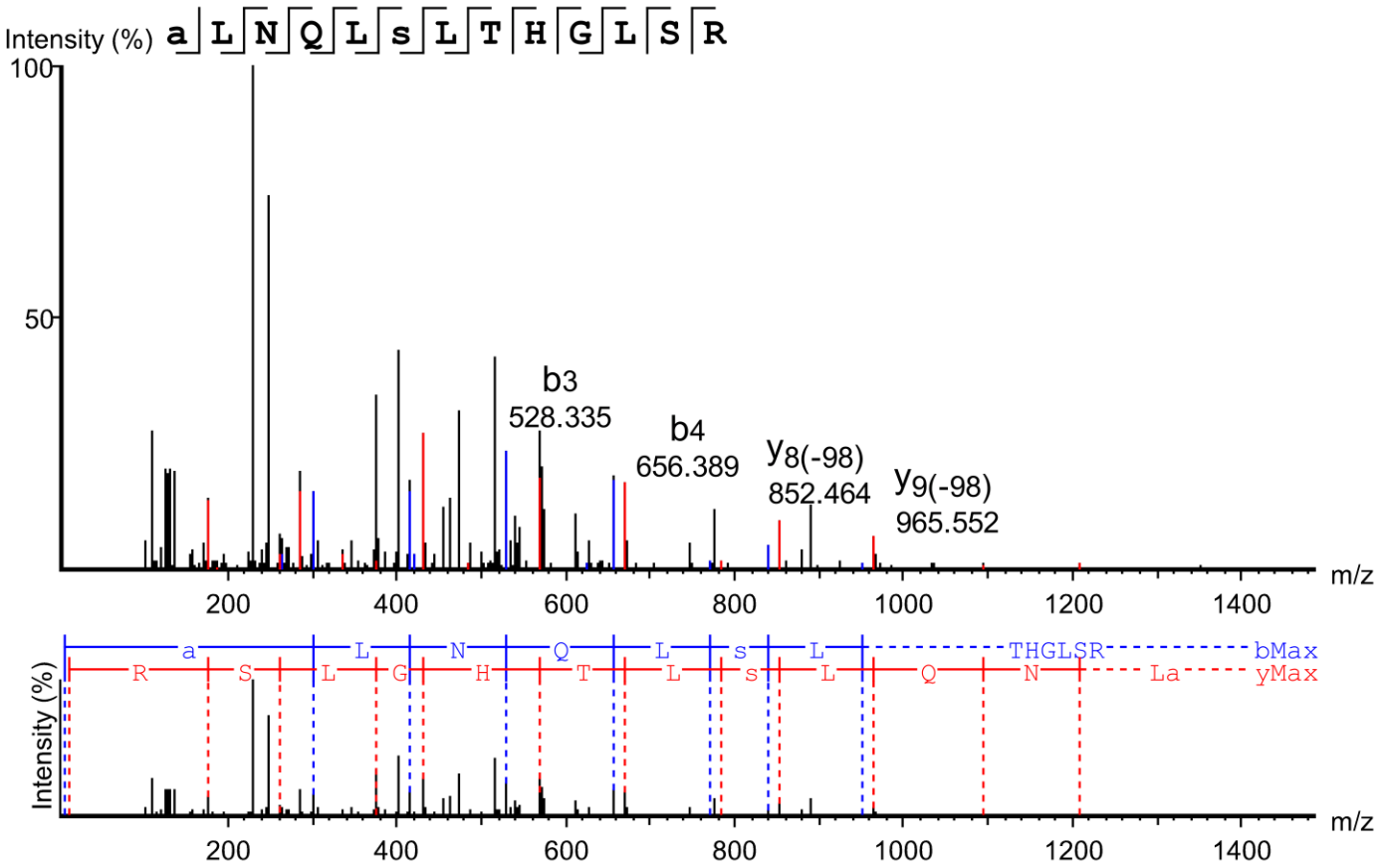

Table 2 - Figure Supplement 1.

Scan 45136, m/z=573.6437, z=3, -10lgP=46.66, ppm=0.7 (pS516)

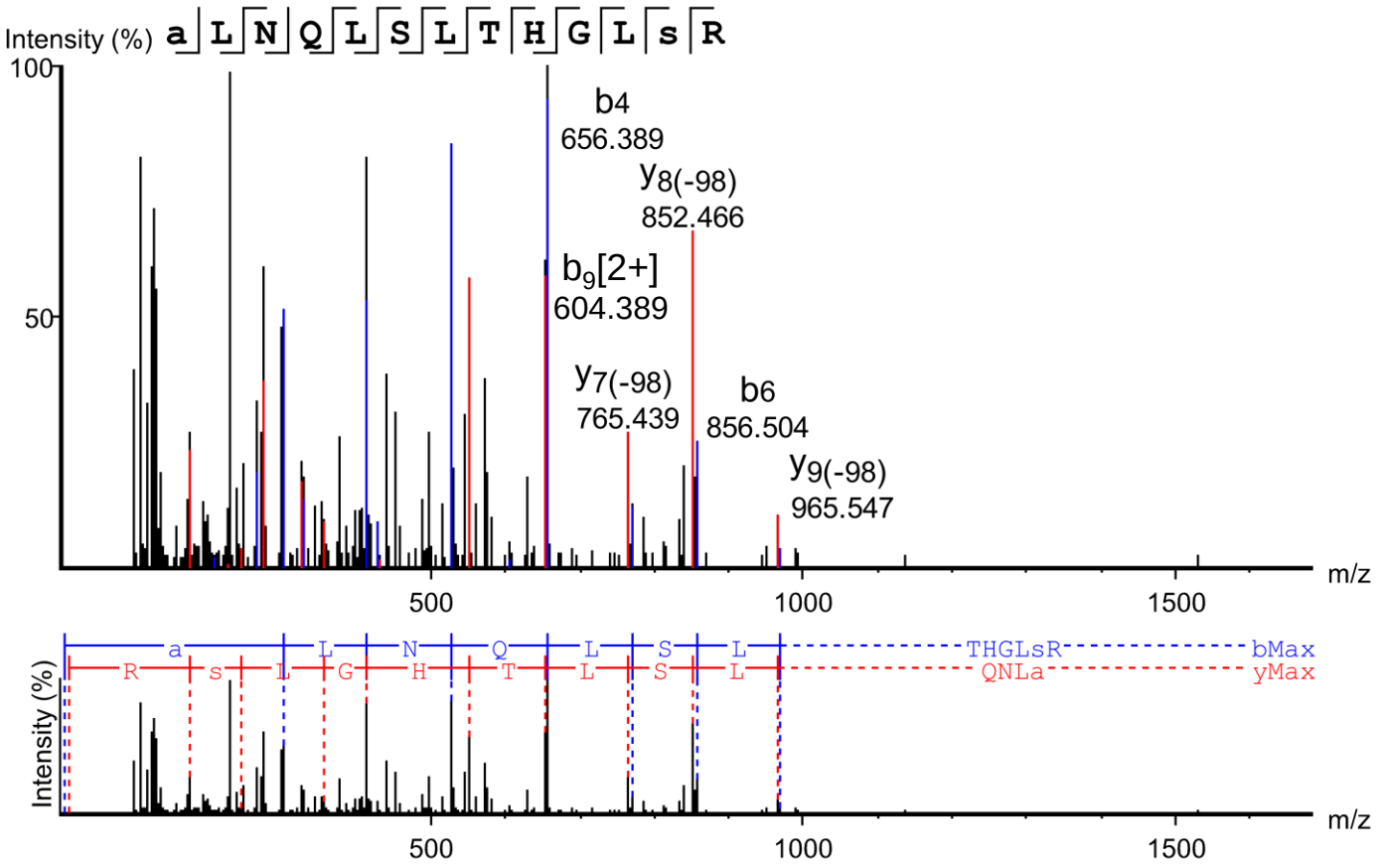

Table 2 - Figure Supplement 1.

Scan 38518, m/z=489.5841, z=3, -10lgP=40.74, ppm=1.7 (pS525)

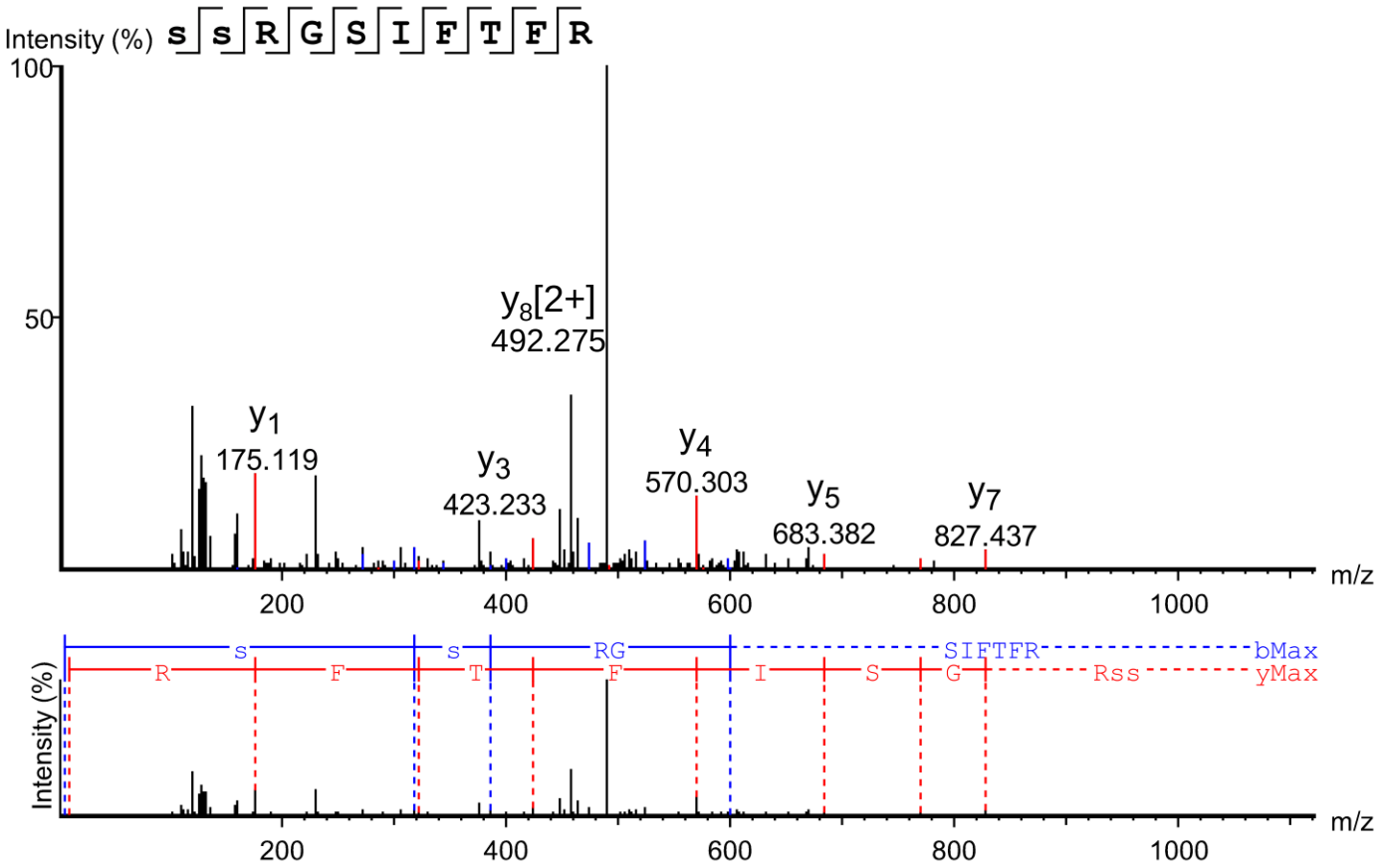

Table 2 - Figure Supplement 1.

Scan 25979, m/z=921.7010, z=3, -10lgP=70.93, ppm=1.2 (pS539)

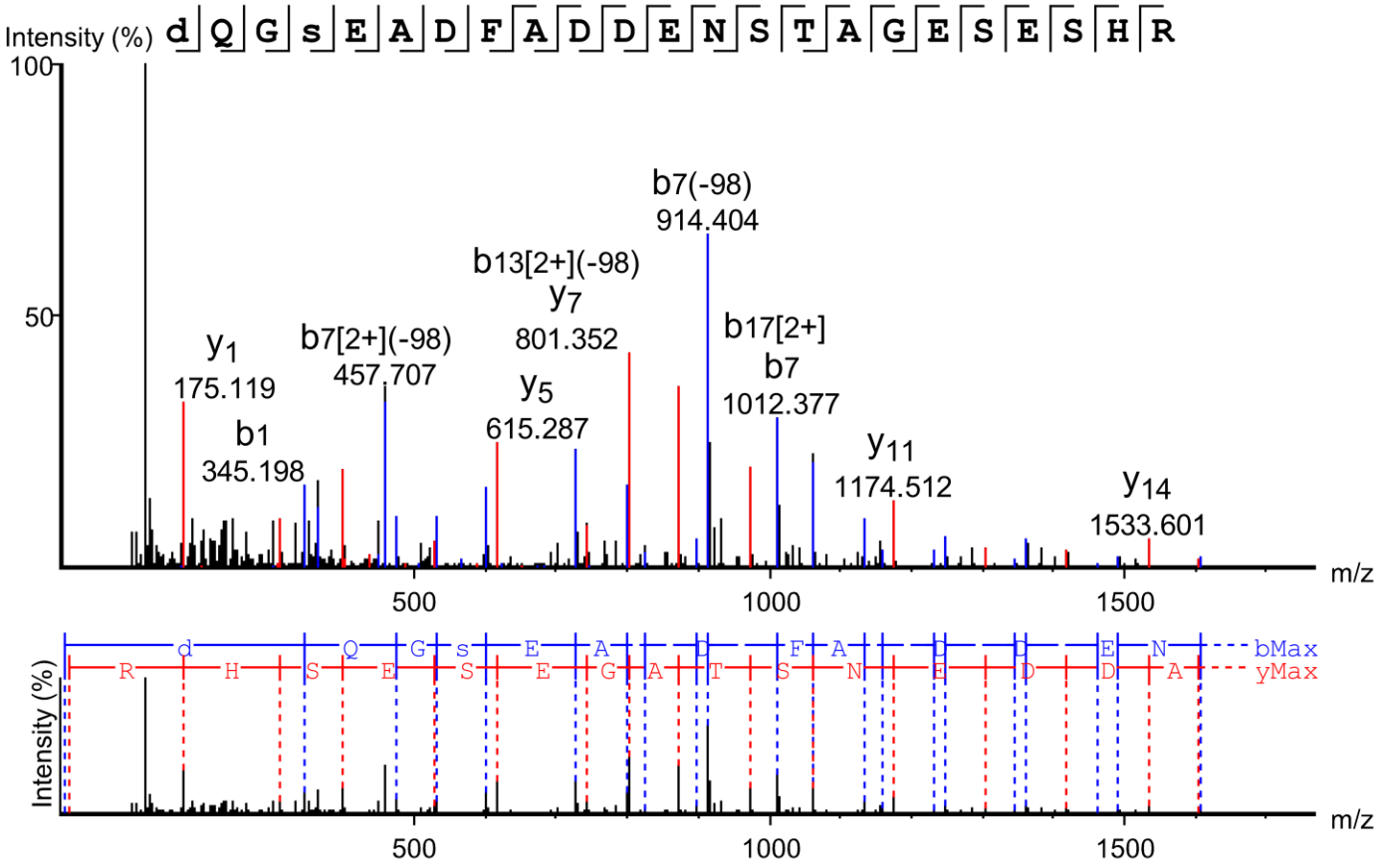

Table 2 - Figure Supplement 1.

Scan 13172, m/z=769.5792, z=4, -10lgP=55.34, ppm=2.5 (pS549)

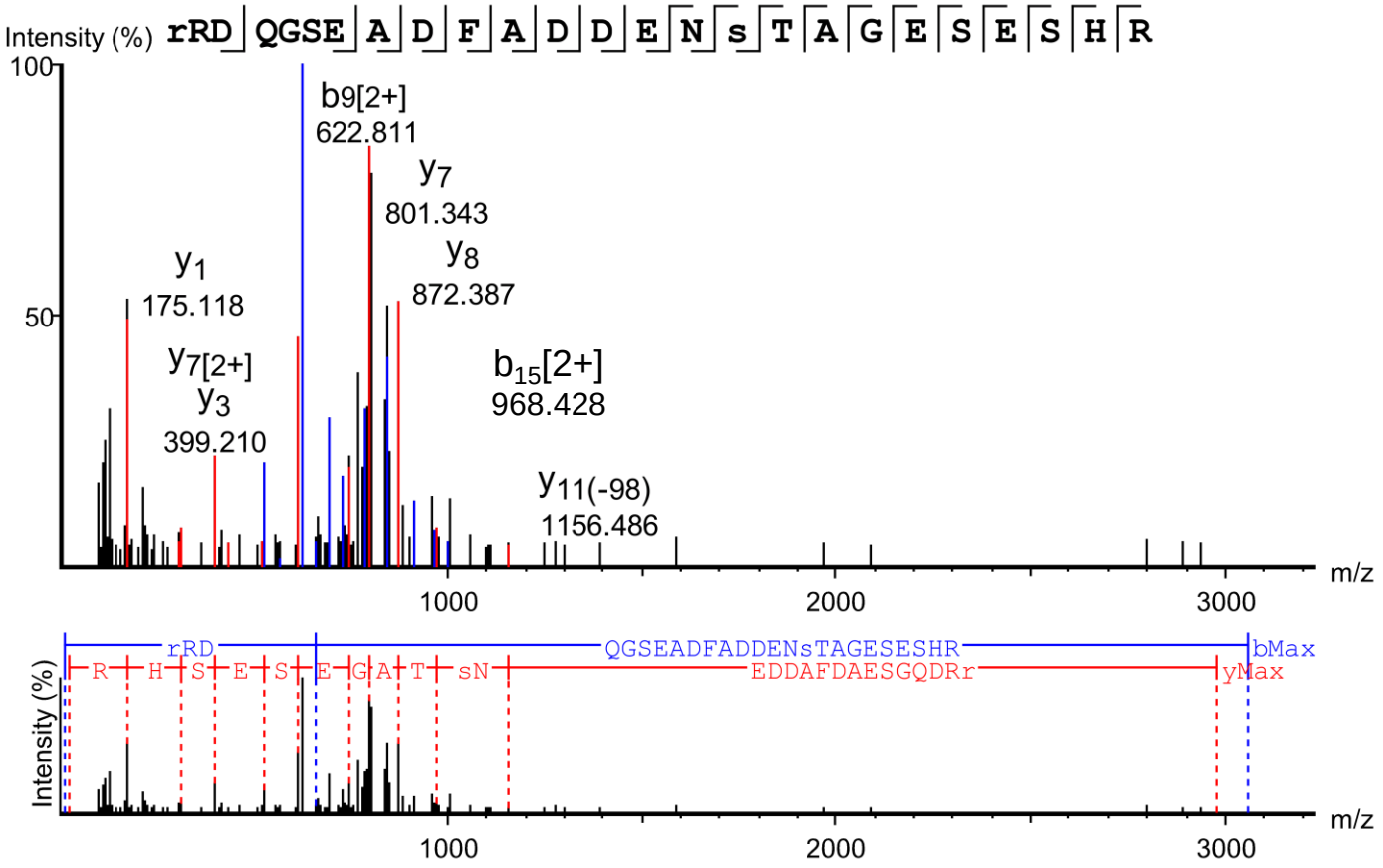

Table 2 - Figure Supplement 1.

Scan 91146, m/z=745.9208, z=2, -10lgP=30.17, ppm=0.6 (pS560)

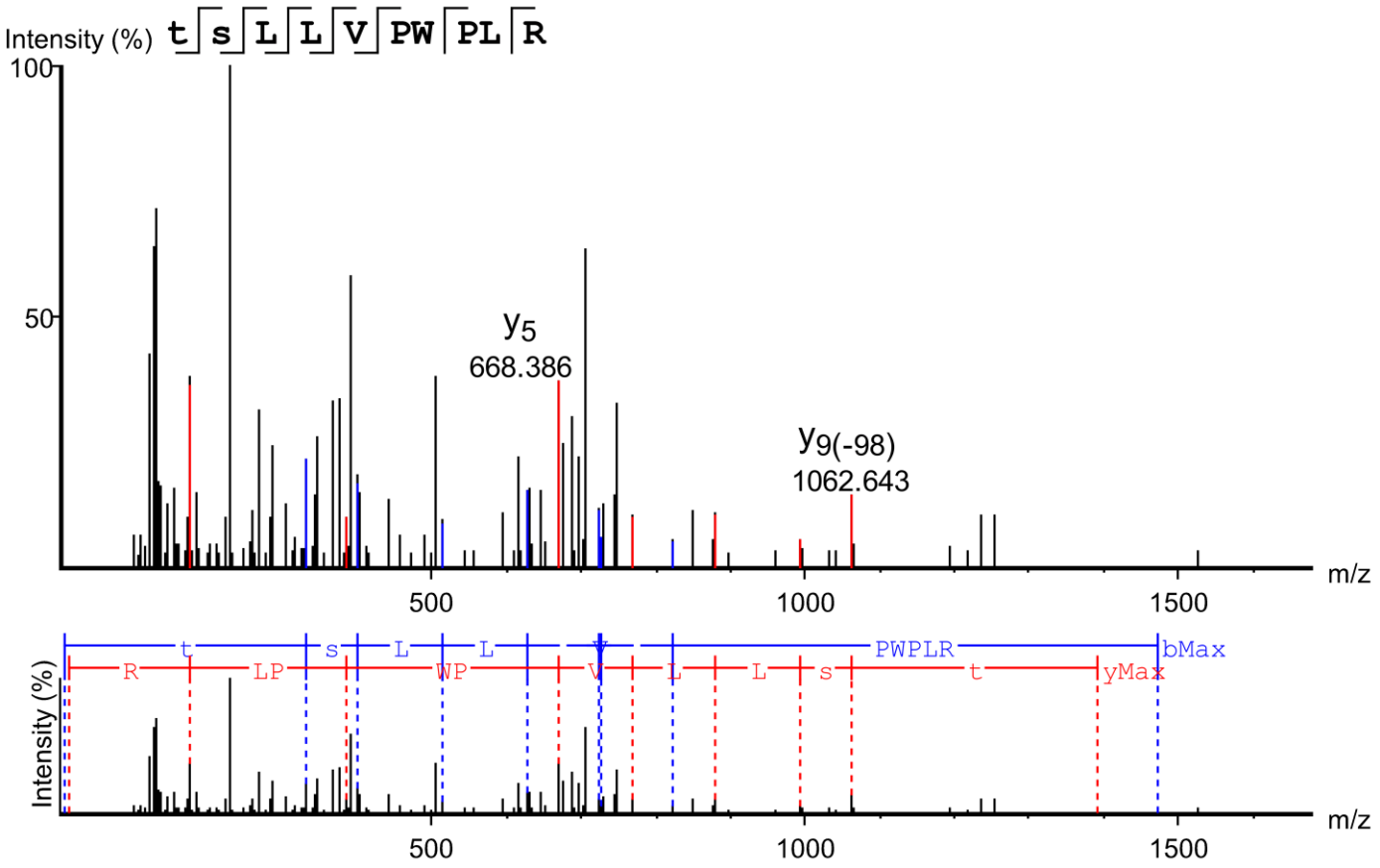

Table 2 - Figure Supplement 1.

Scan 35559, m/z=911.4655, z=3, -10lgP=55.17, ppm=-3.7 (pS571)

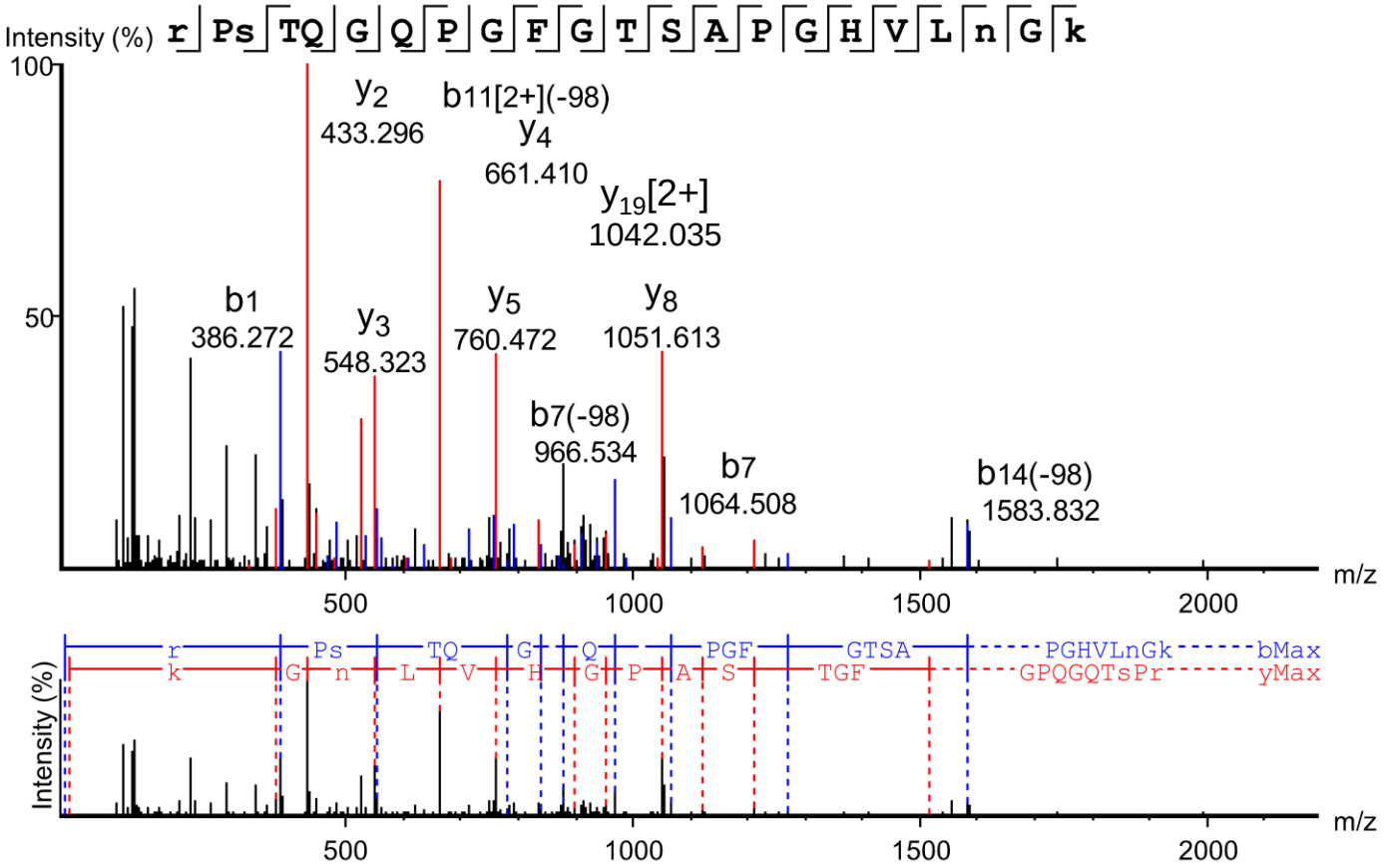

Table 2 - Figure Supplement 1.

Scan 36455, m/z=683.8556, z=4, -10lgP=48.45, ppm=3.1 (pS581)

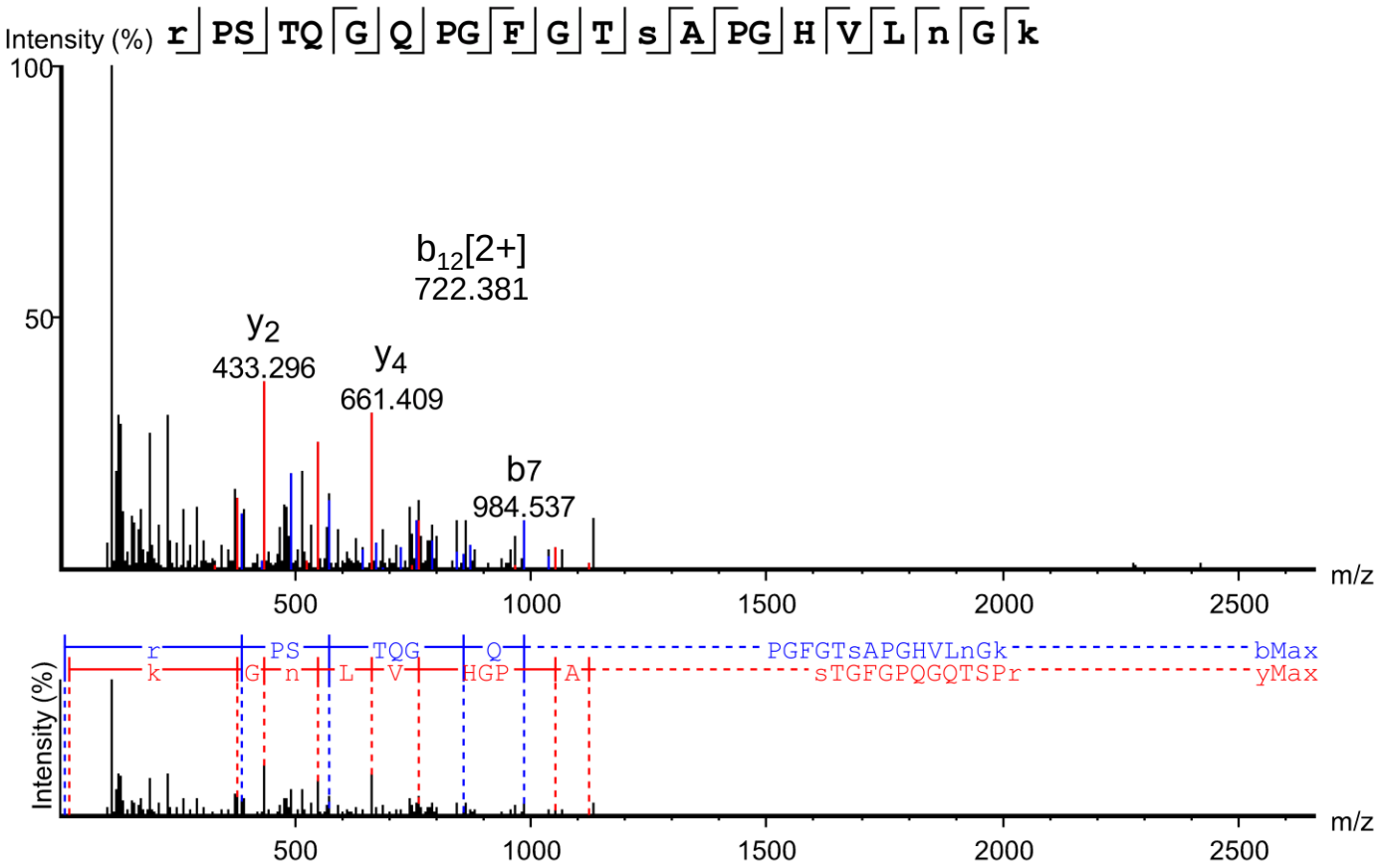

Table 2 - Figure Supplement 1.

Scan 59637, m/z=841.6600, z=4, -10lgP=71.71, ppm=-0.6 (pS593)

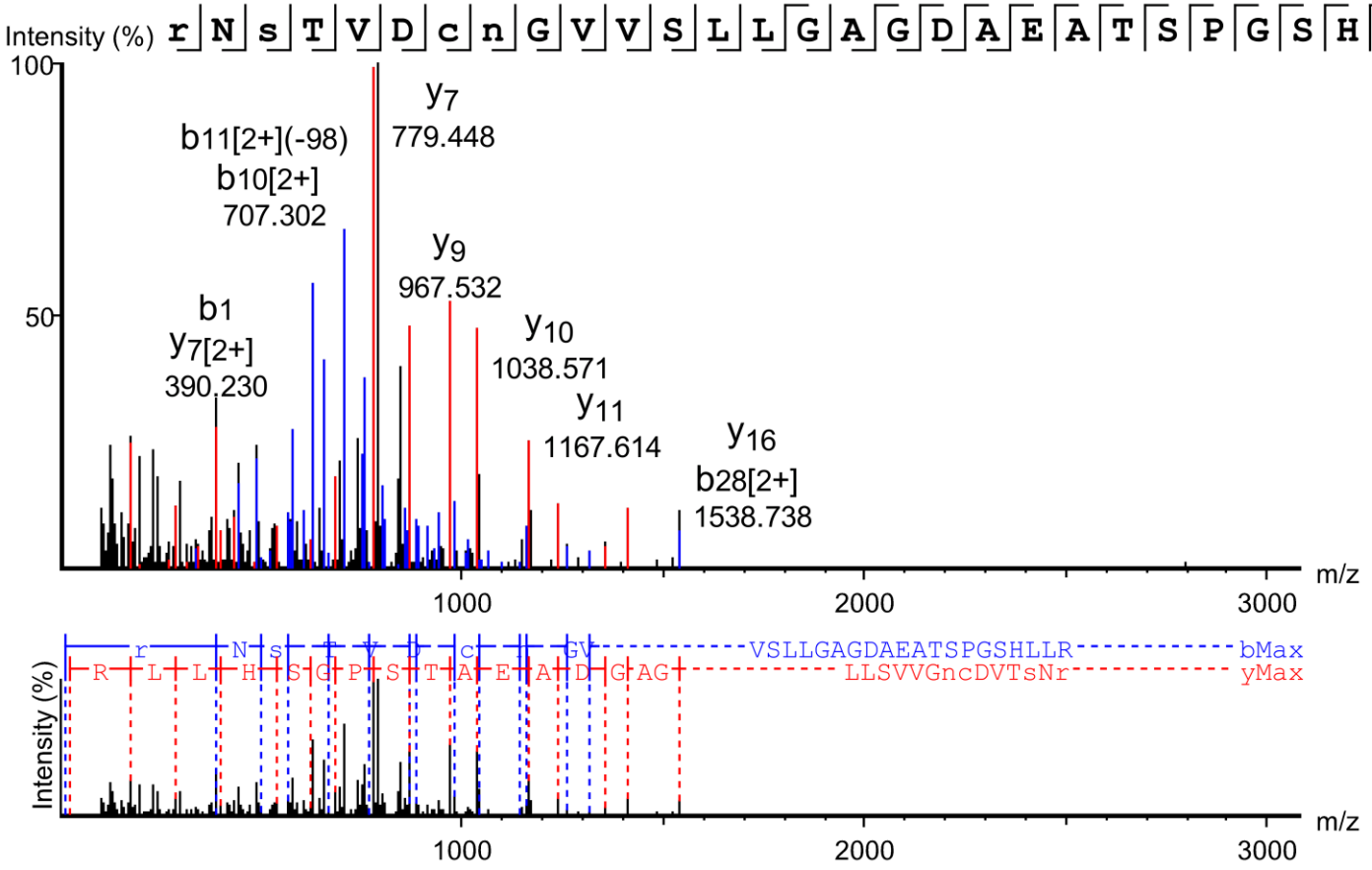

Table 2 - Figure Supplement 1.

Scan 91558, m/z=936.5065, z=3, -10lgP=60.59, ppm=3.3 (pS664)

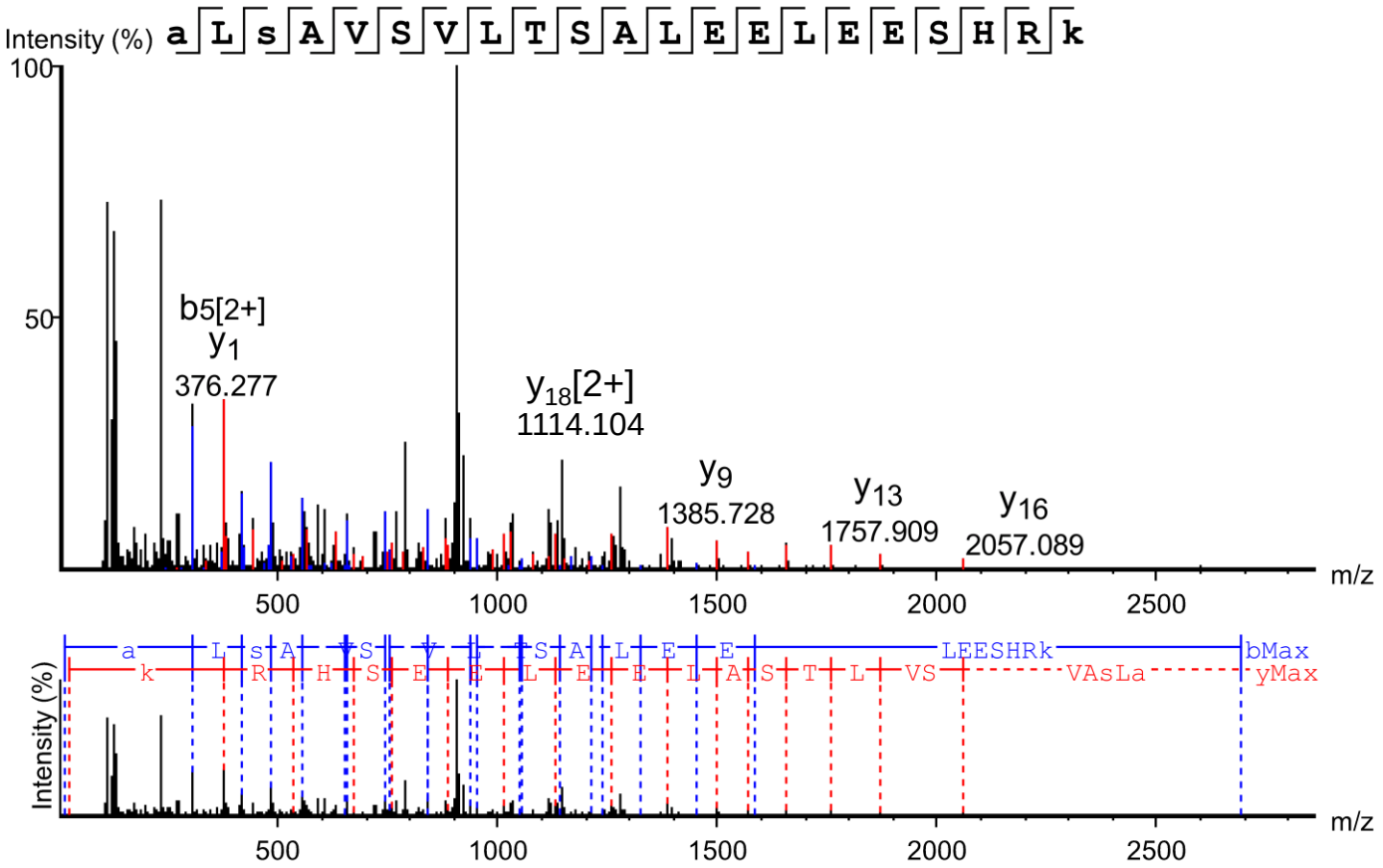

Table 2 - Figure Supplement 1.

Scan 97561, m/z=817.4163, z=3, -10lgP=64.07, ppm=-1.4 (pS667)

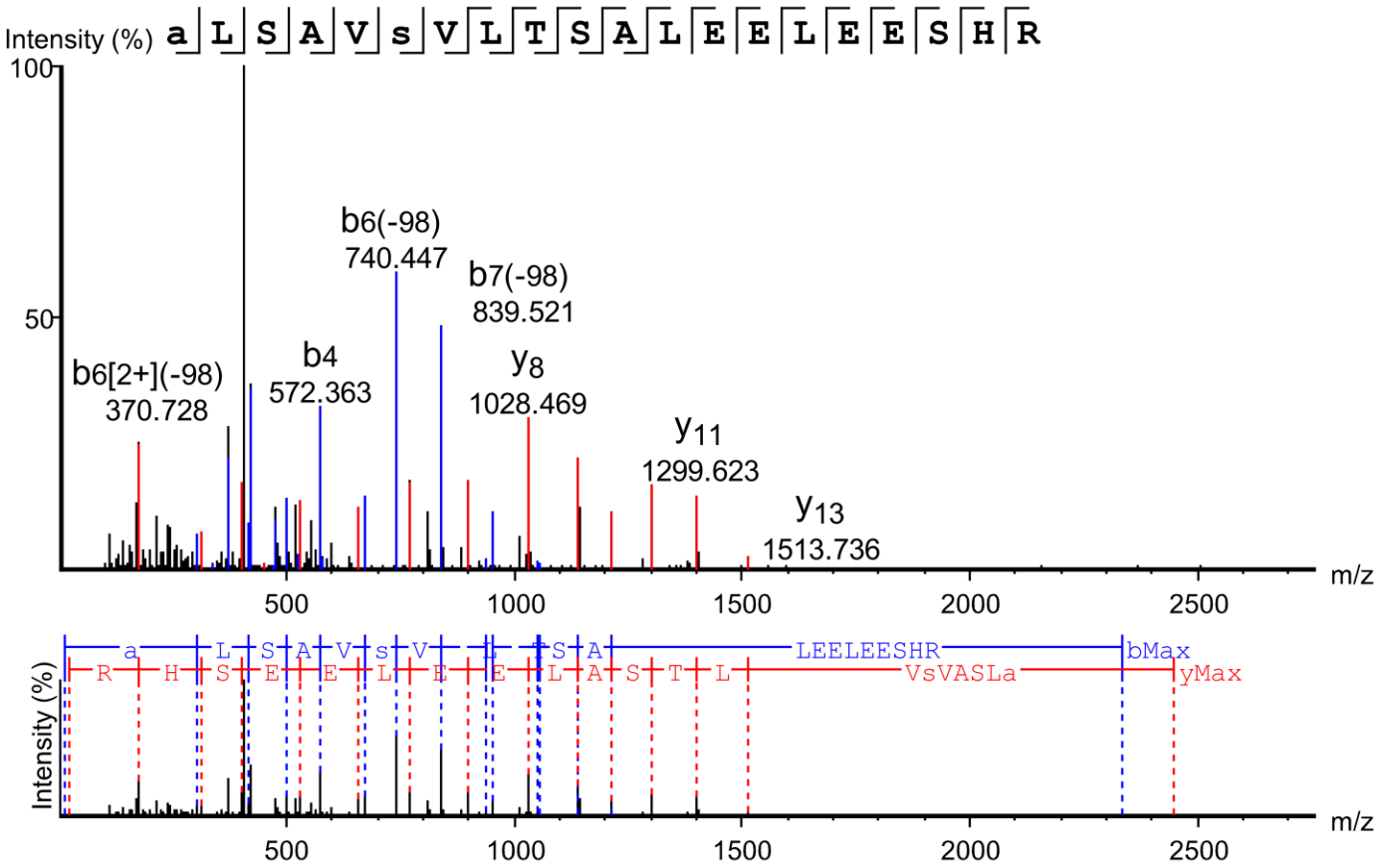

Table 2 - Figure Supplement 1.

Scan 85466, m/z=702.6287, z=4, -10lgP=54.31, ppm=-1.0 (pT670)

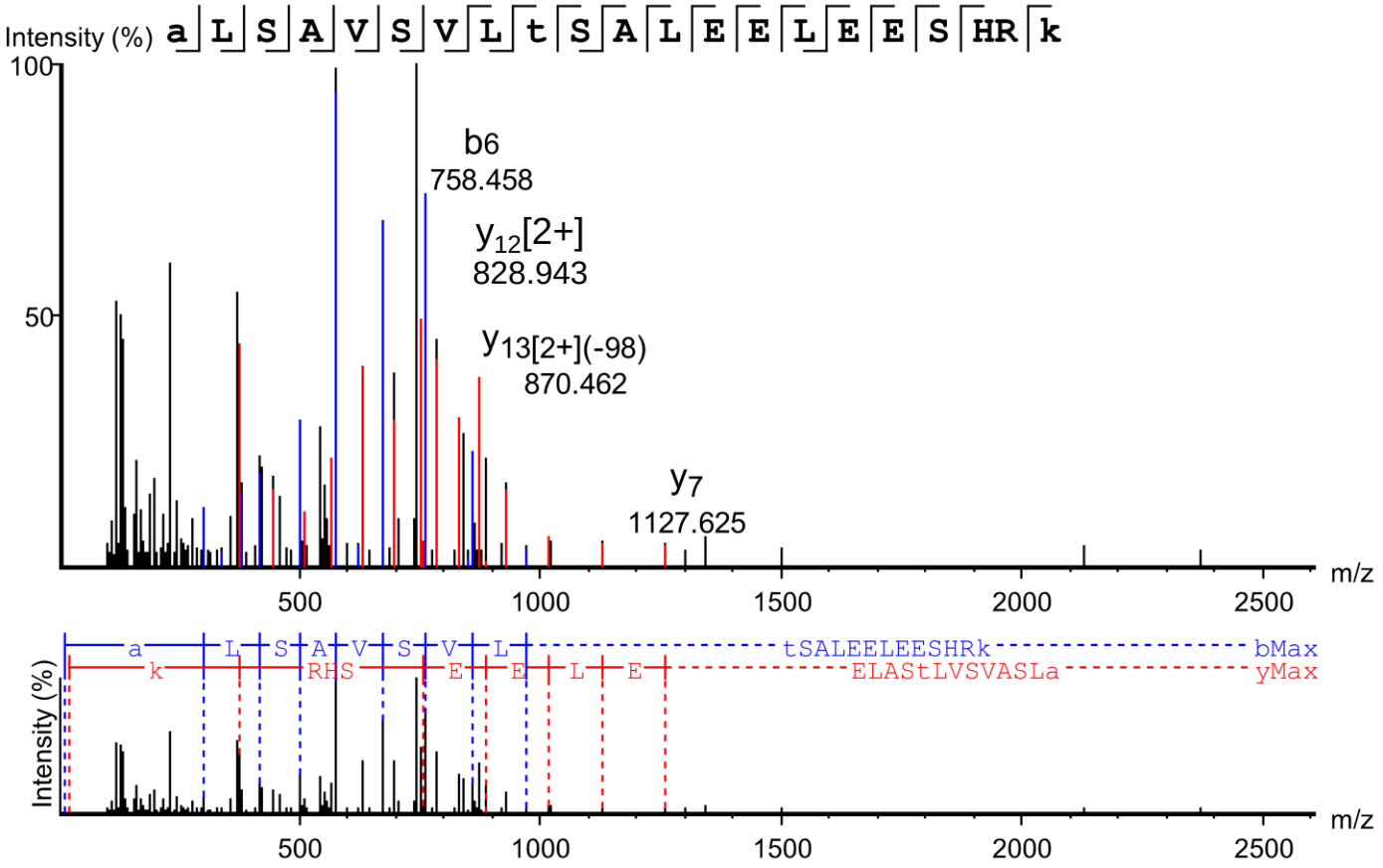

Table 2 - Figure Supplement 1.

Scan 88006, m/z=702.6296, z=4, -10lgP=63.19, ppm=0.3 (pS671)

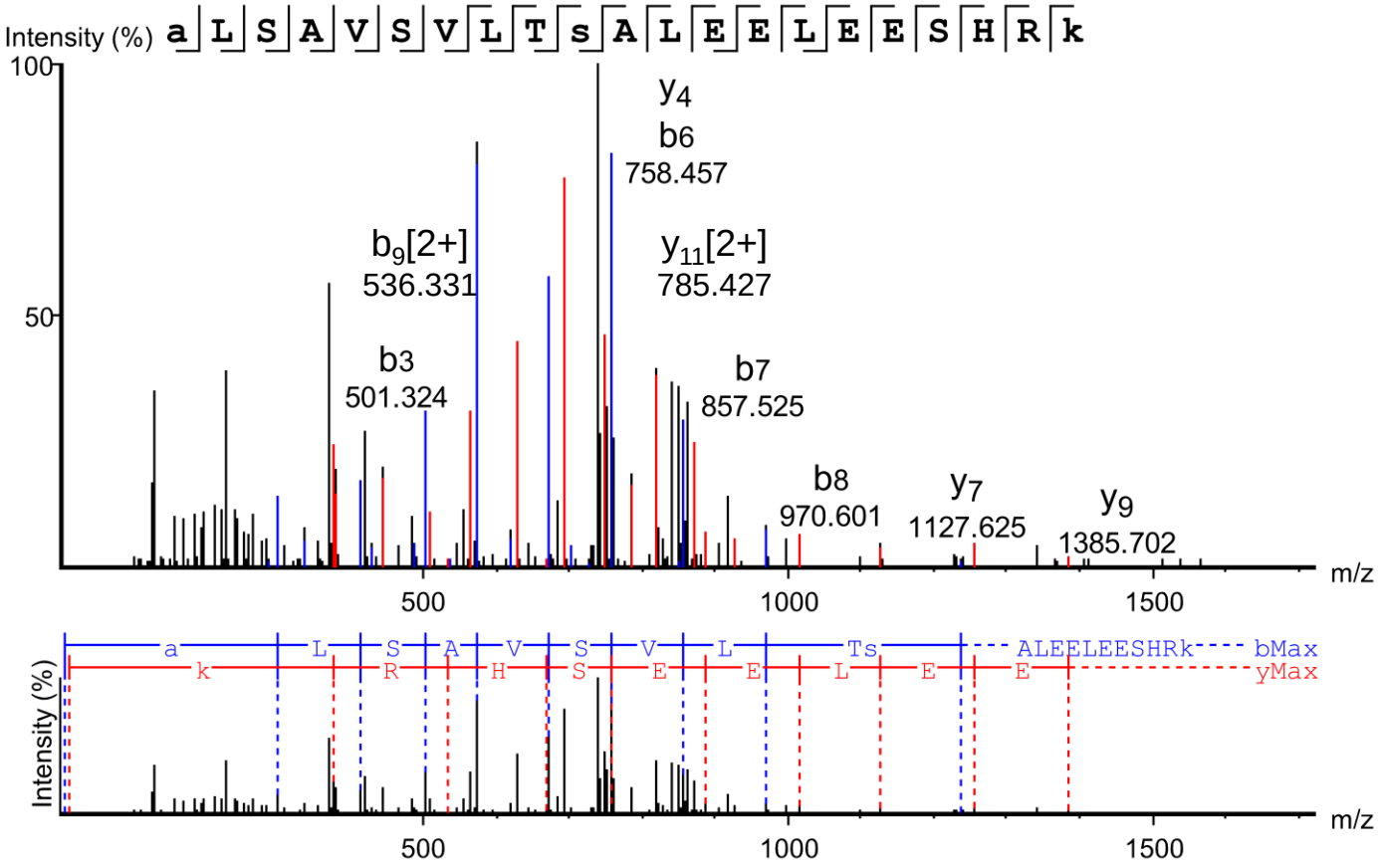

Table 2 - Figure Supplement 1.

Scan 93723, m/z=886.7712, z=3, -10lgP=58.77, ppm=0.1 (pS664 + pS667)

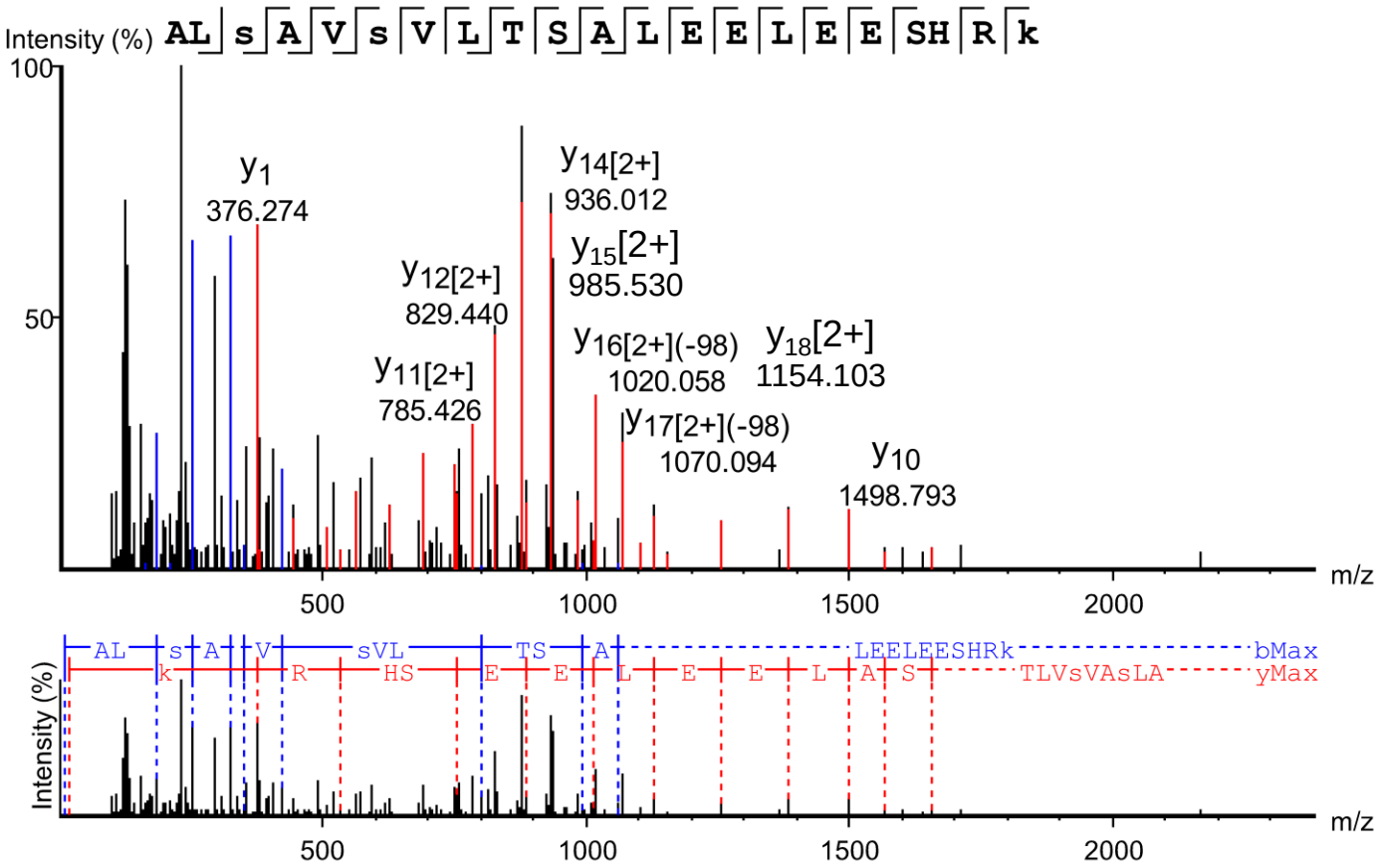

Table 2 - Figure Supplement 1.

Scan 99097, m/z=844.0719, z=3, -10lgP=59.30, ppm=-1.1 (pS664 + pT670)

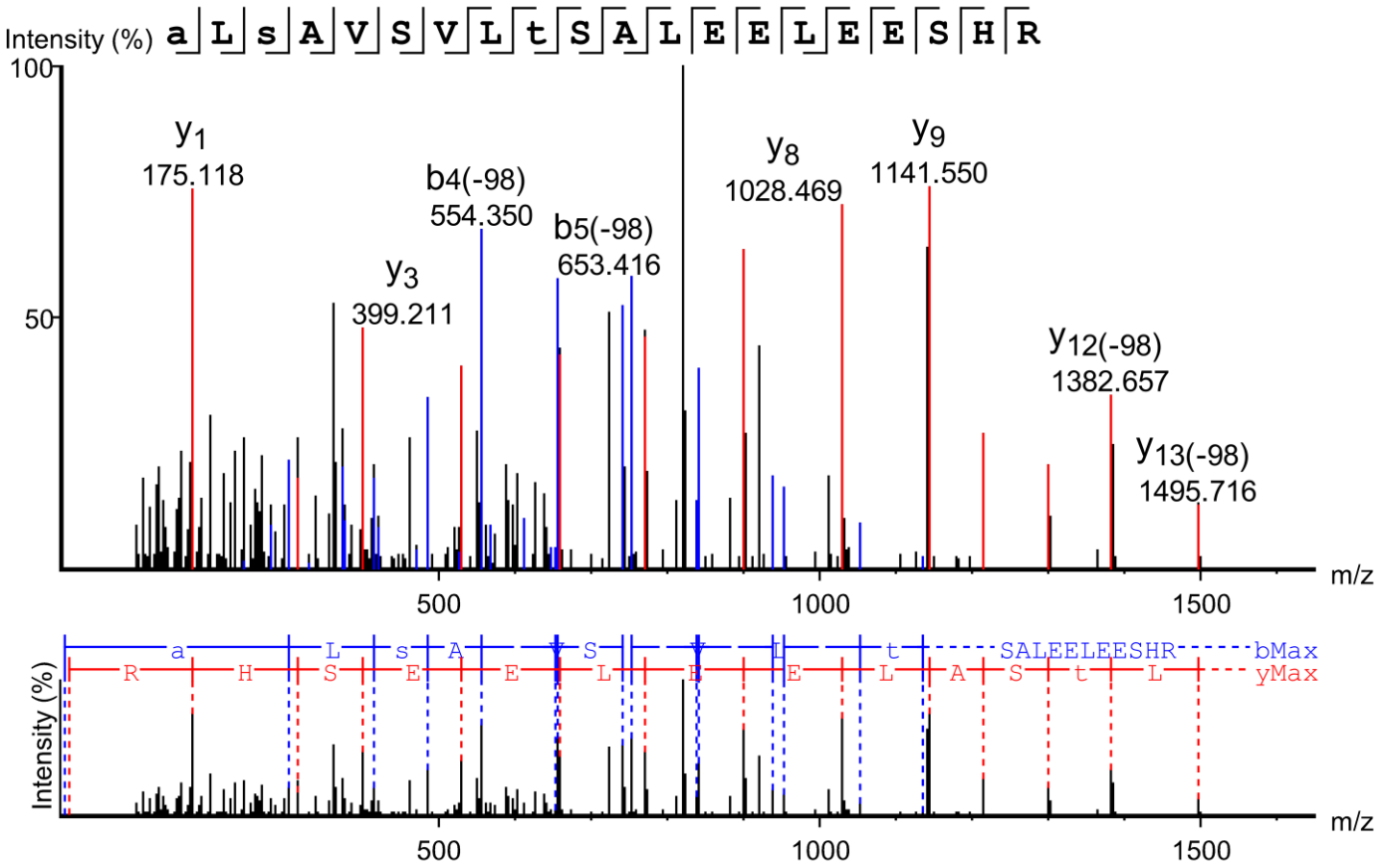

Table 2 - Figure Supplement 1.

Scan 101033, m/z=844.0723, z=3, -10lgP=58.32, ppm=-0.6 (pS664 + pS671)

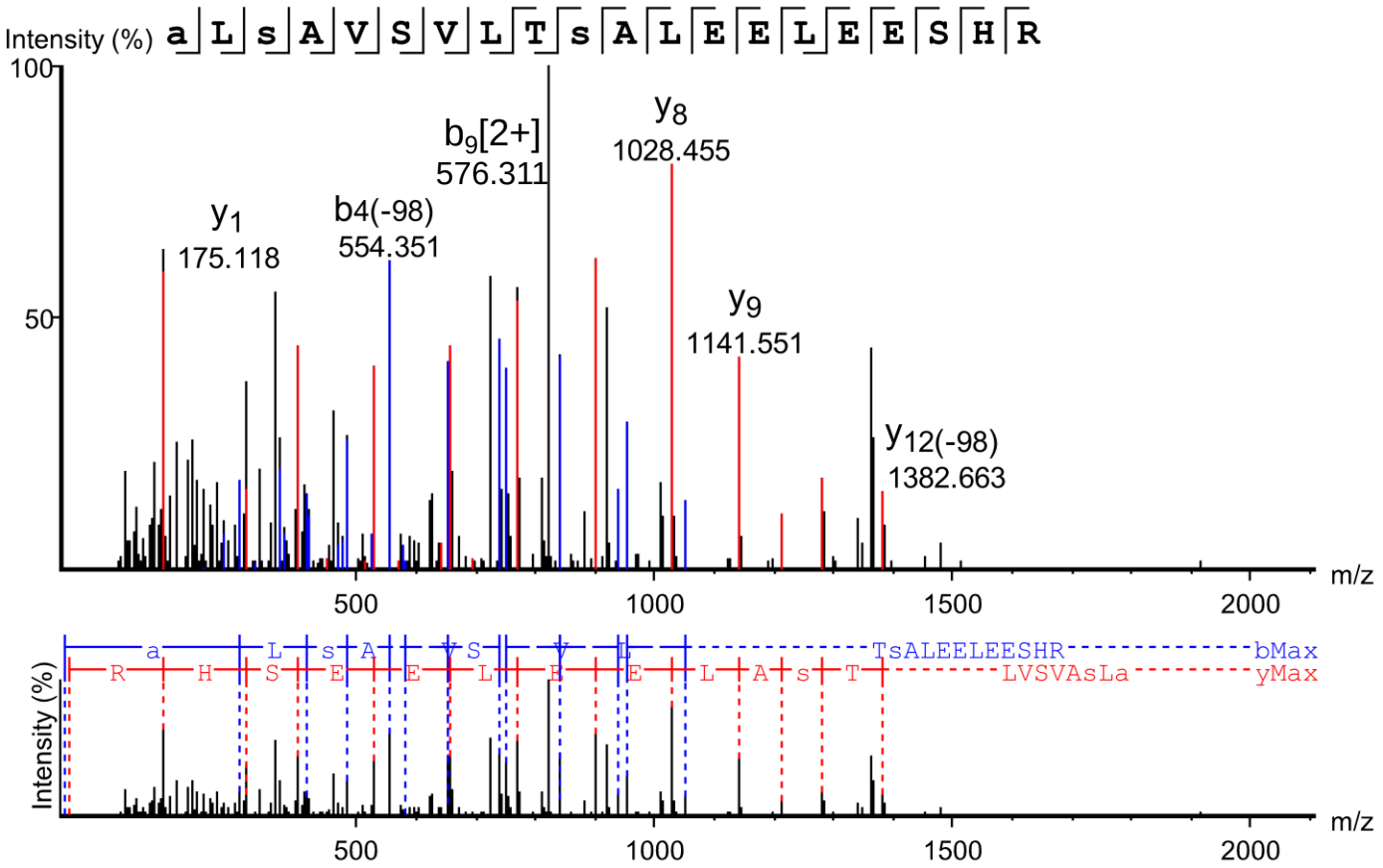

Table 2 - Figure Supplement 1.

Scan 93884, m/z=722.6213, z=4, -10lgP=54.08, ppm=0.5 (pS667 + pT670)

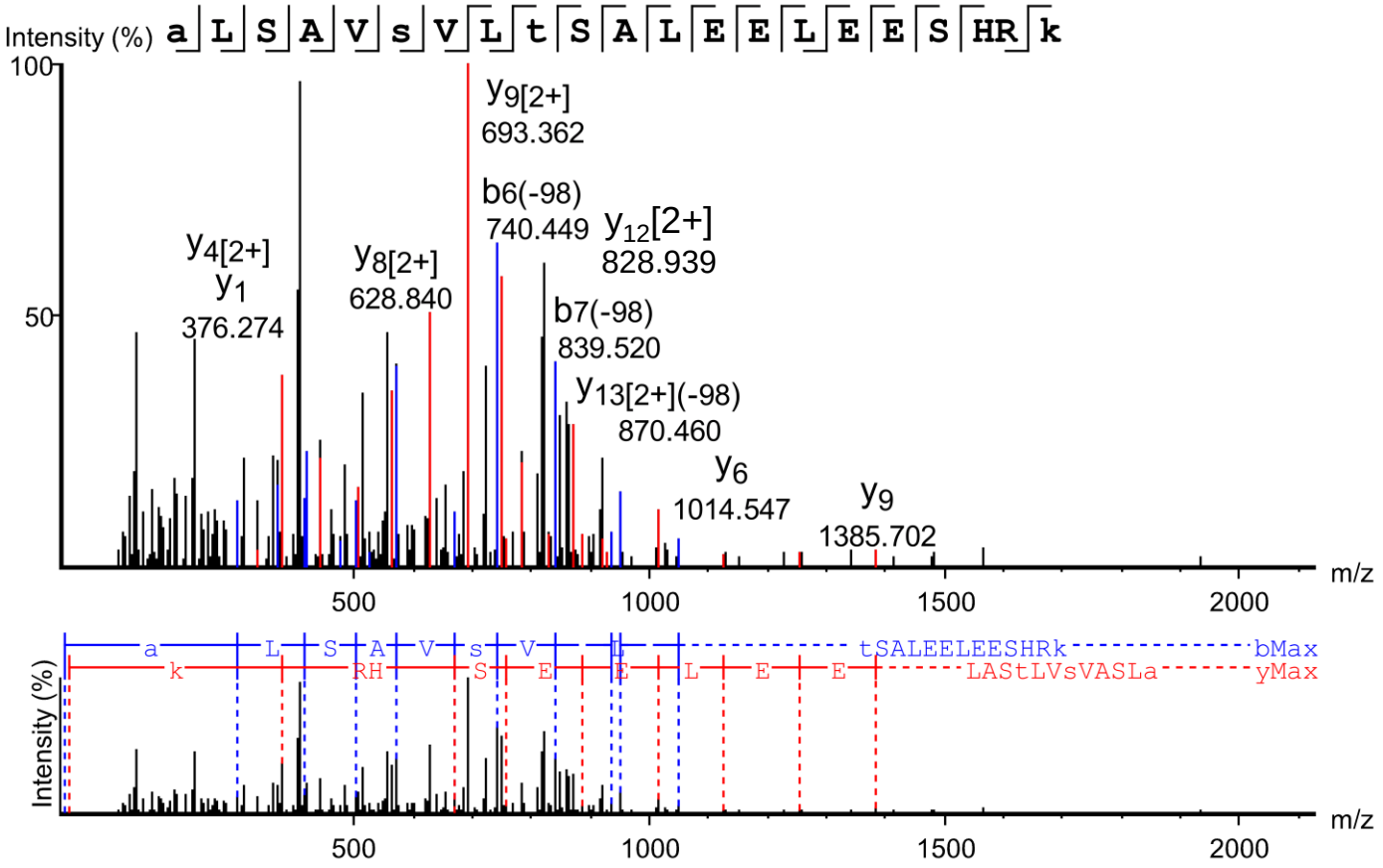

Table 2 - Figure Supplement 1.

Scan 101560, m/z=844.0726, z=3, -10lgP=60.51, ppm=-0.3 (pS667 + pS671)

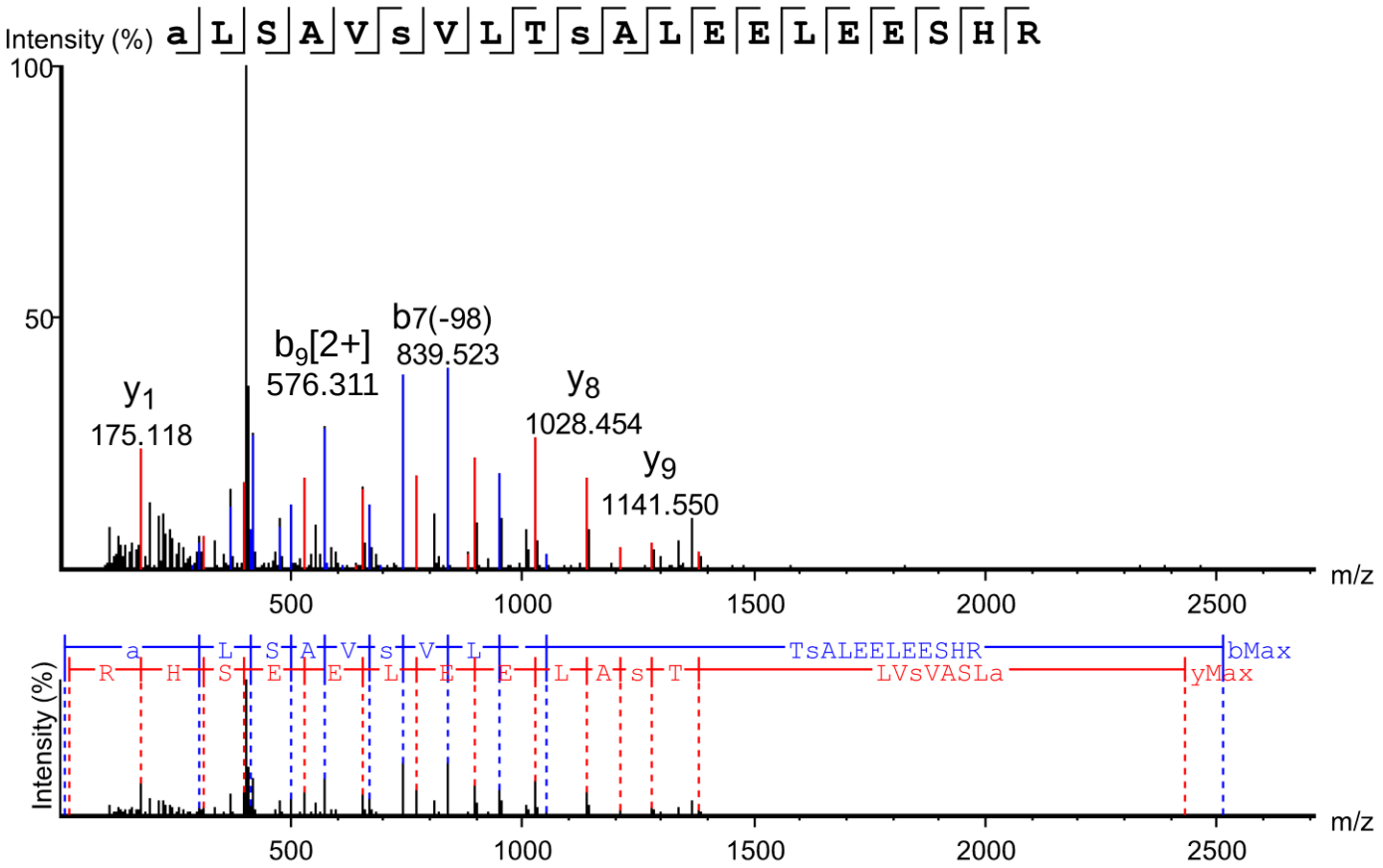

Table 2 - Figure Supplement 1.

Scan 41764, m/z=824.1139, z=3, -10lgP=48.76, ppm=-5.4 (pT999)

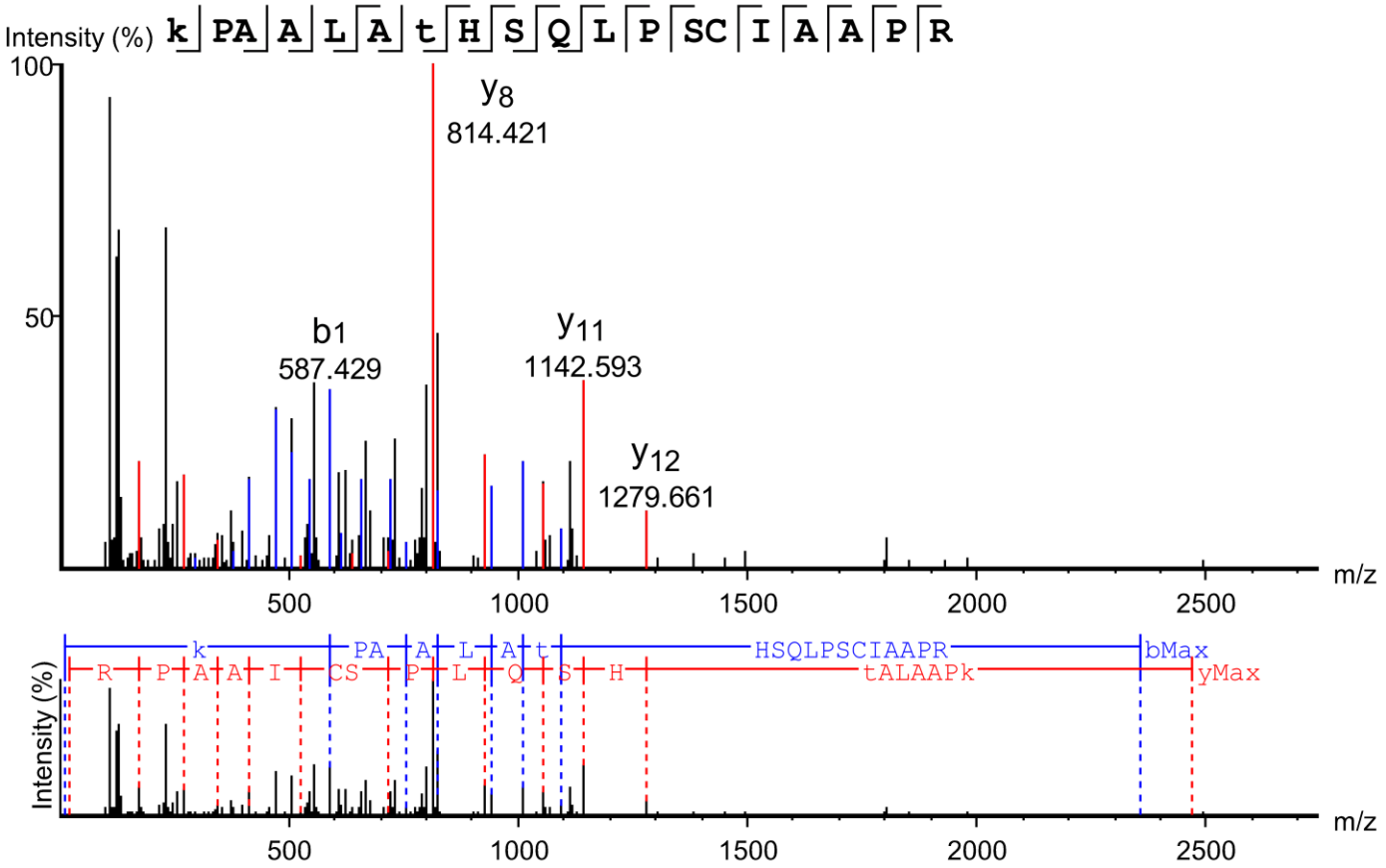

Table 2 - Figure Supplement 1.

Scan 16929, m/z=503.5912, z=3, -10lgP=32.62, ppm=6.4 (pS1001)

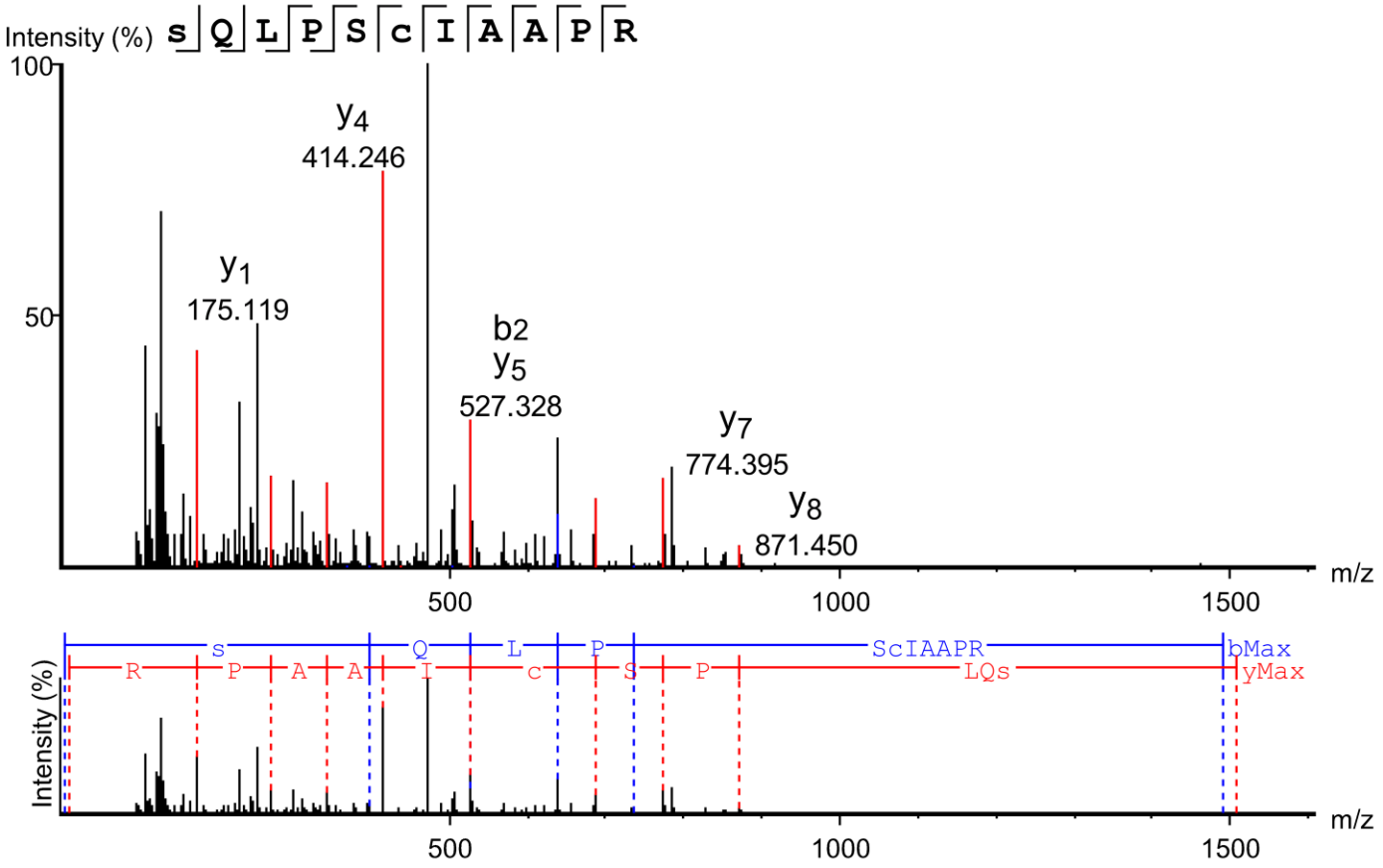

Table 2 - Figure Supplement 1.

Scan 39364, m/z=702.3888, z=6, -10lgP=71.41, ppm=-0.2 (pS1005)

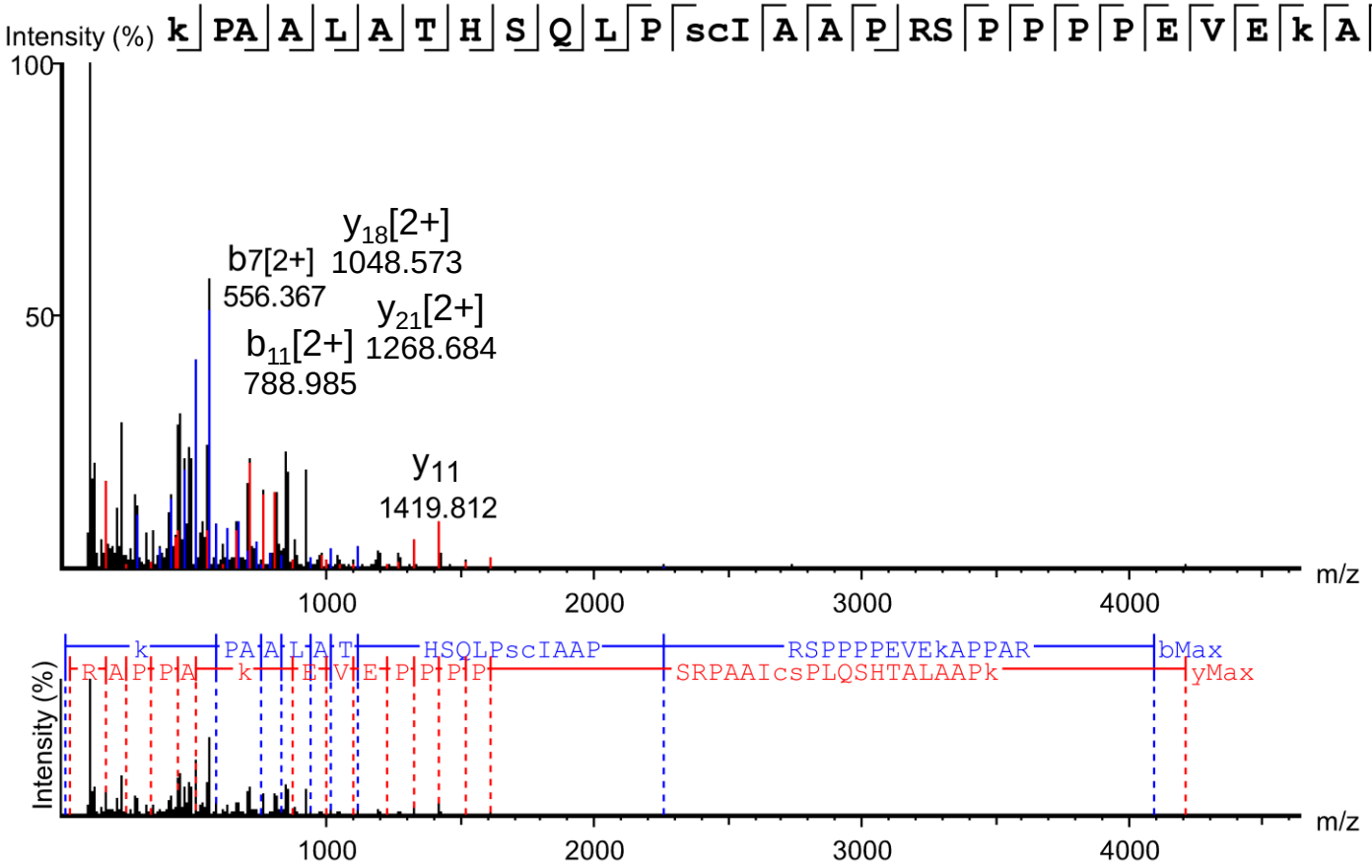

Table 2 - Figure Supplement 1.

Scan 33829, m/z=759.4054, z=2, -10lgP=42.26, ppm=1.3 (pS1012)

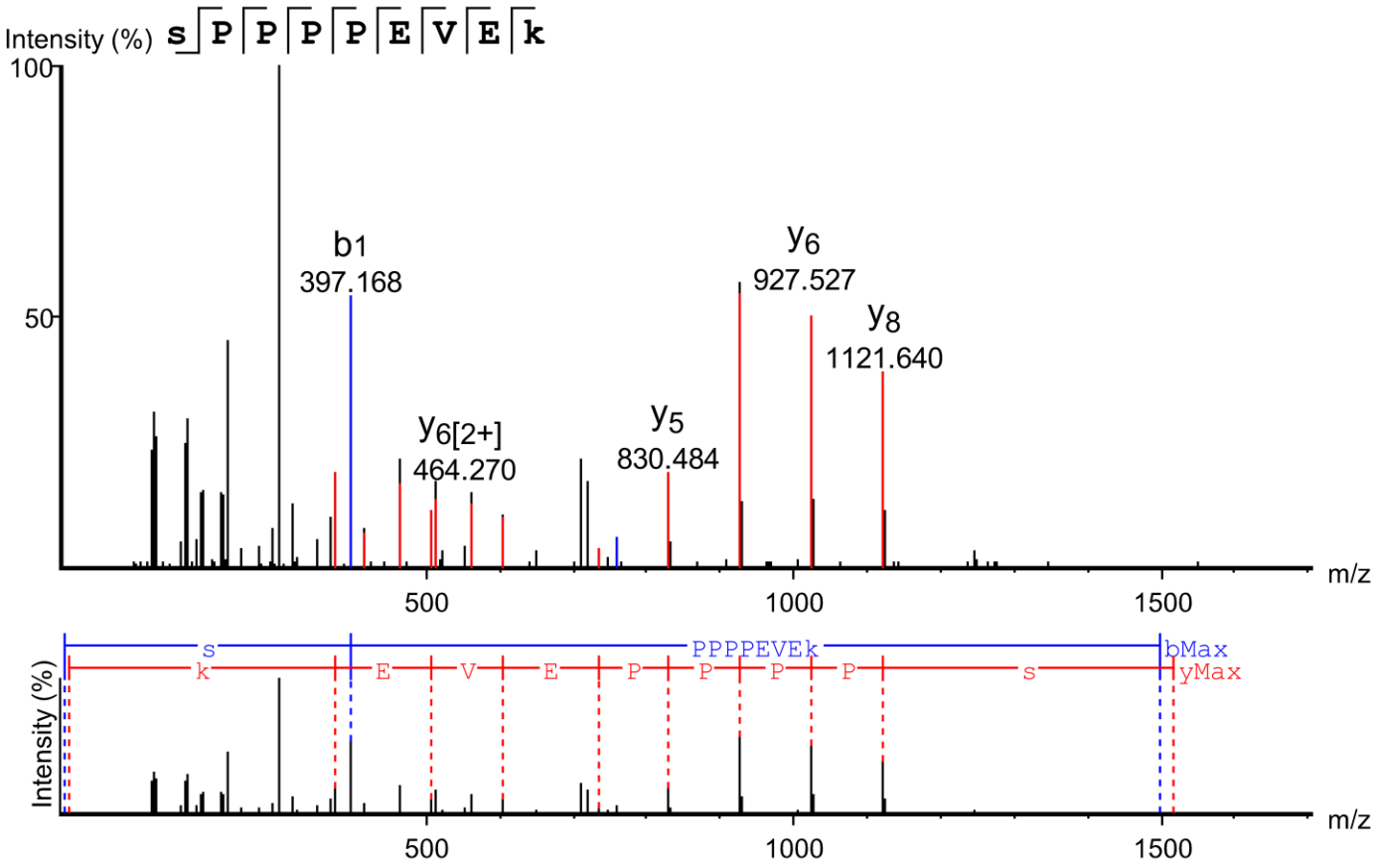

Table 2 - Figure Supplement 1.

Scan 64017, m/z=1230.5586, z=5, -10lgP=57.25, ppm=0.8 (pS1056 and/or T1058)

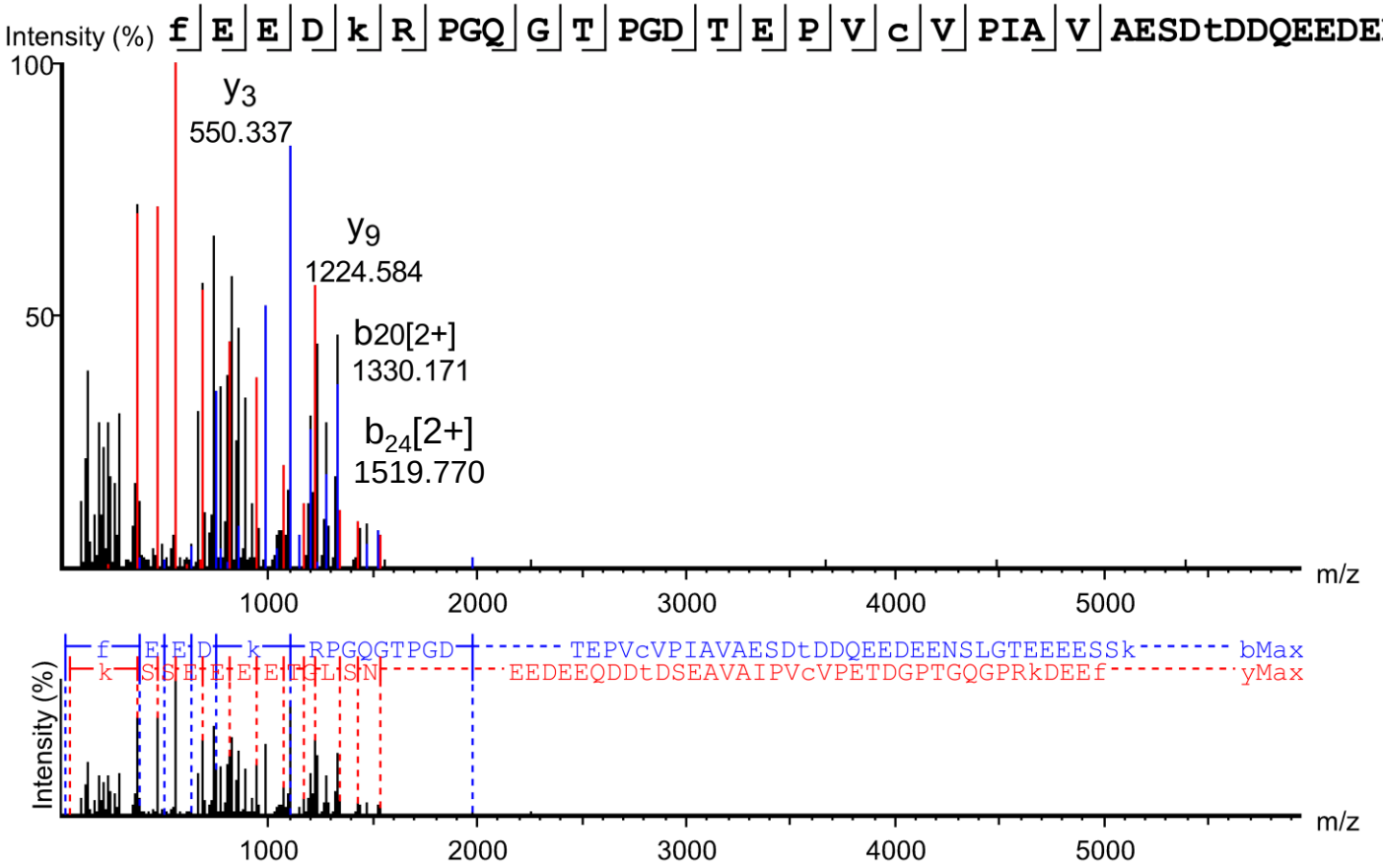

Table 2 - Figure Supplement 1.

Scan 53783, m/z=1070.1316, z=3, -10lgP=64.34, ppm=-3.2 (pT1105)

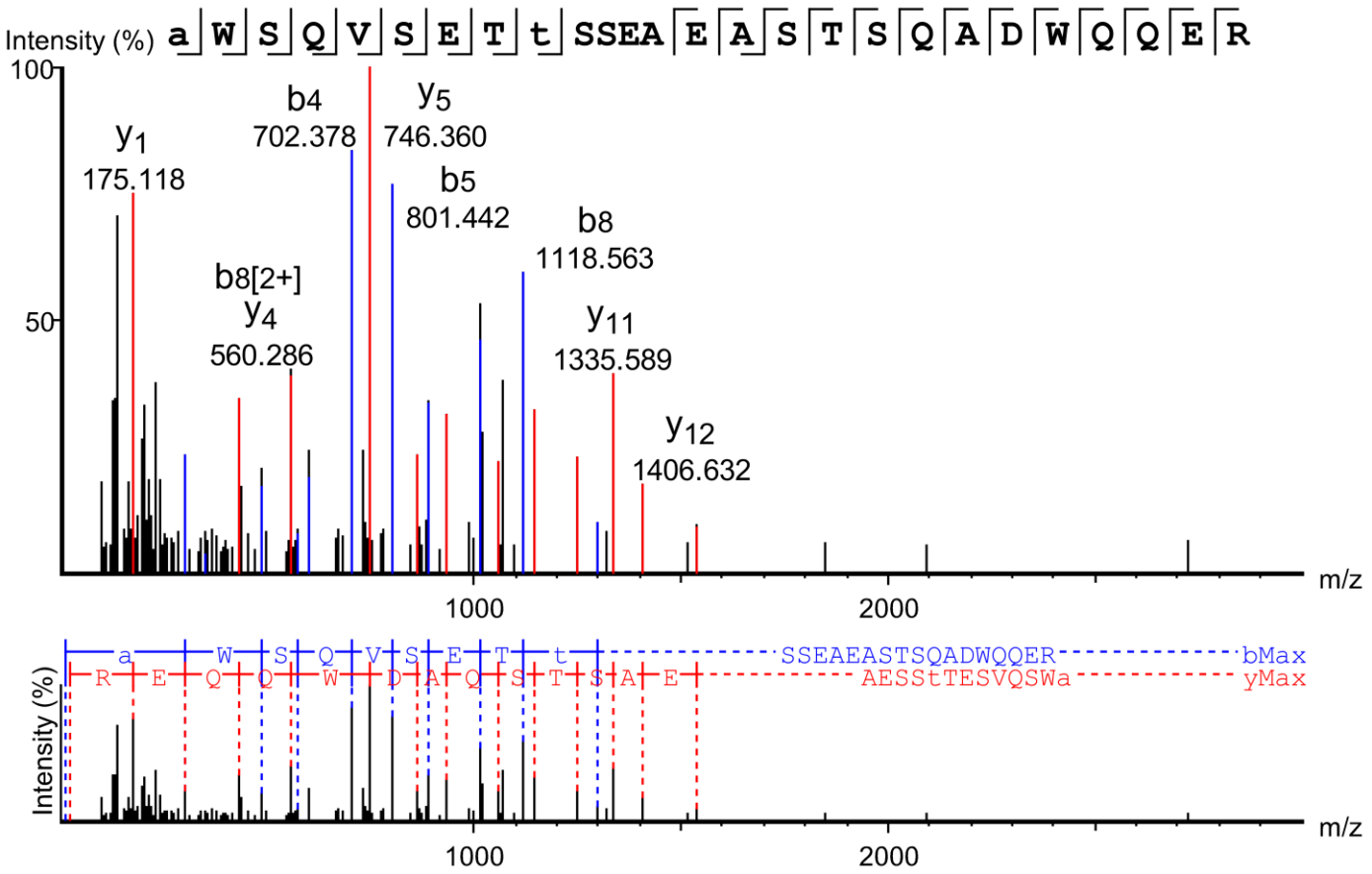

Table 2 - Figure Supplement 1.

Scan 54409, m/z=1070.1345, z=3, -10lgP=69.89, ppm=-0.5 (pS1107)

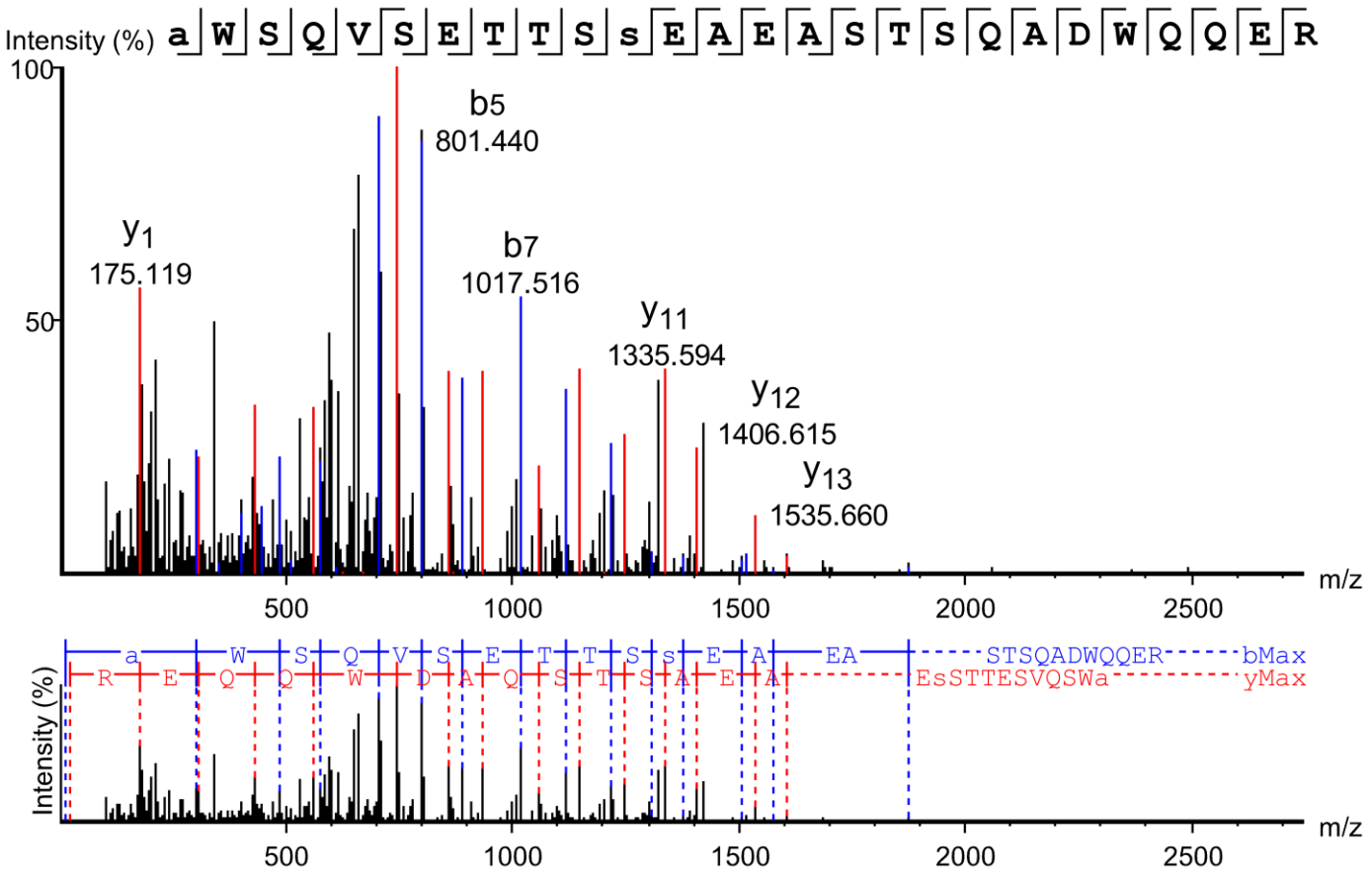

Table 2 - Figure Supplement 1.

Scan 92771, m/z=1312.5819, z=4, -10lgP=44.70, ppm=3.2 (pS1138)

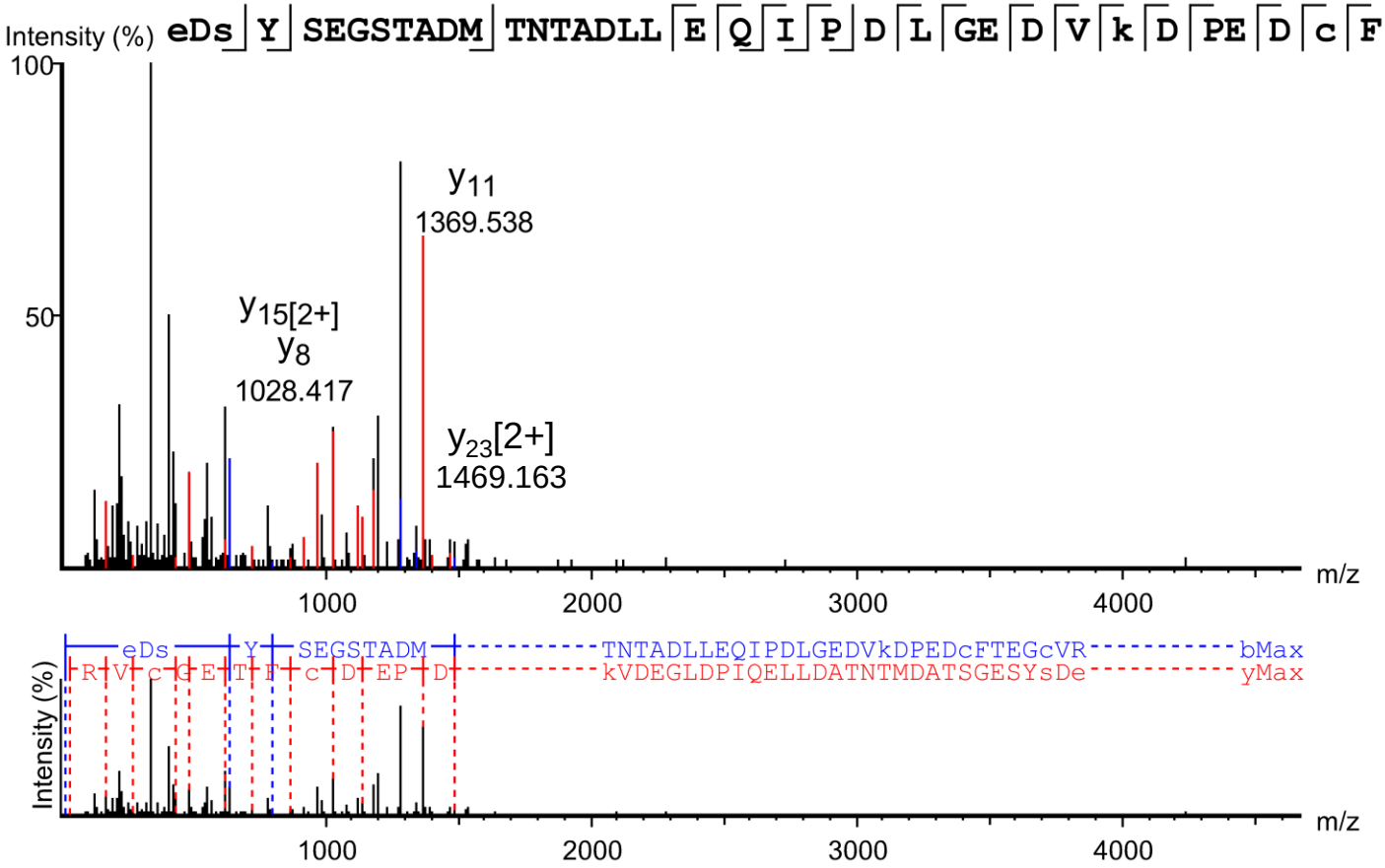

Table 2 - Figure Supplement 1.

Scan 101916, m/z=903.4511, z=3, -10lgP=54.76, ppm=-1.2 (pT1809)

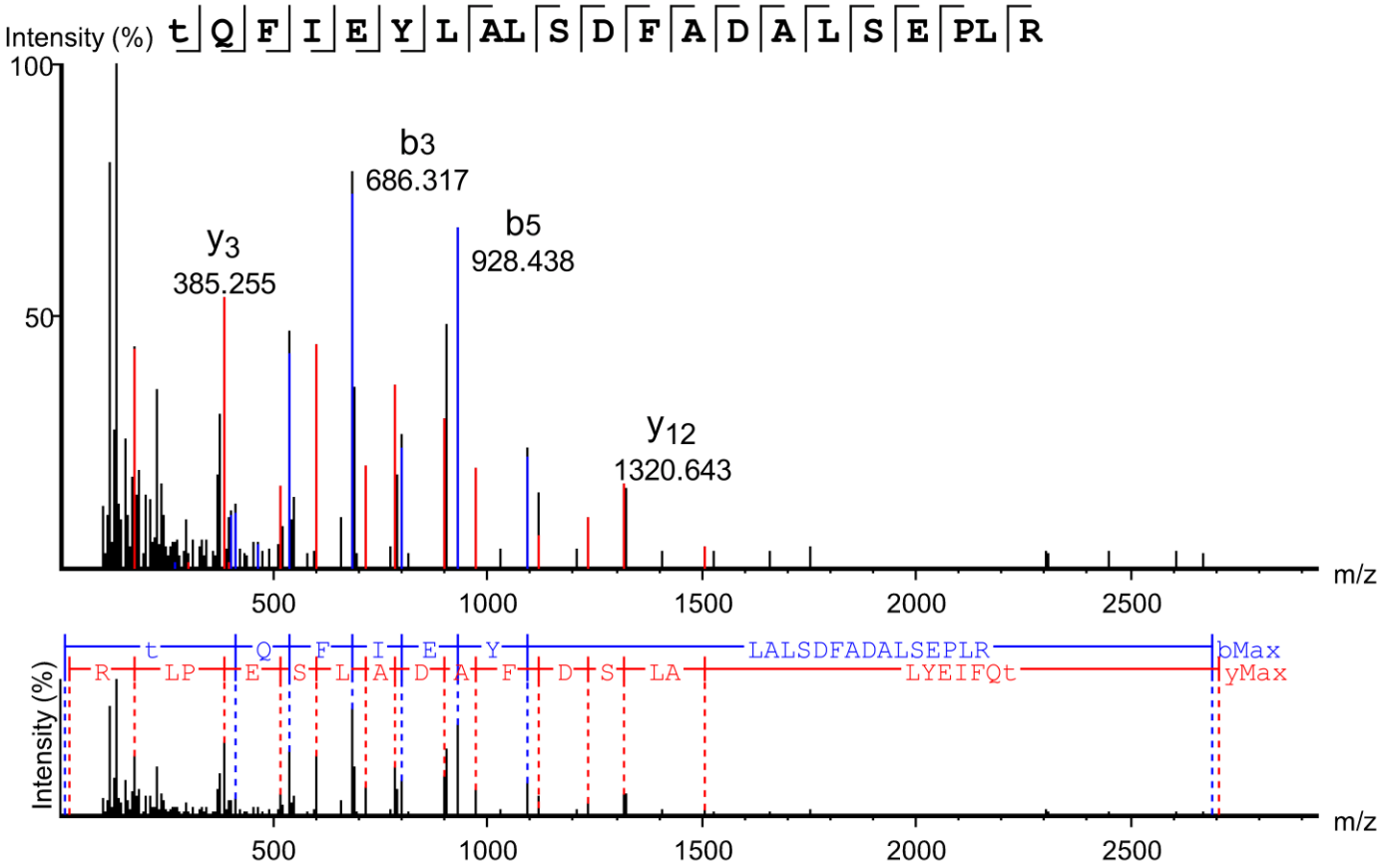

Table 2 - Figure Supplement 1.

Scan 24603, m/z=978.4300, z=2, -10lgP=60.07, ppm=-0.9 (pS1937)

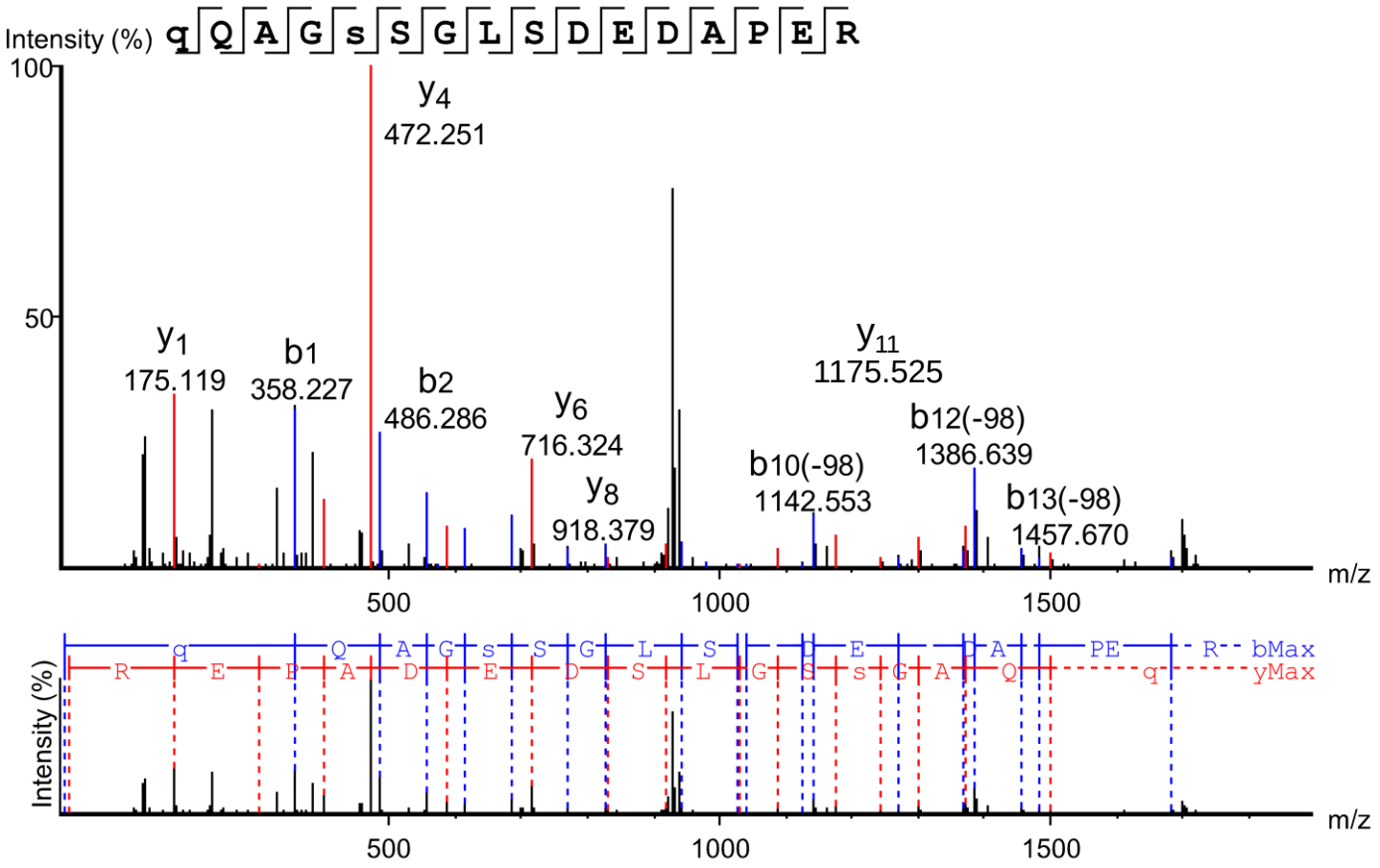

Table 2 - Figure Supplement 1.

Scan 67128, m/z=885.7517, z=3, -10lgP=50.34, ppm=0.7 (pS1964)

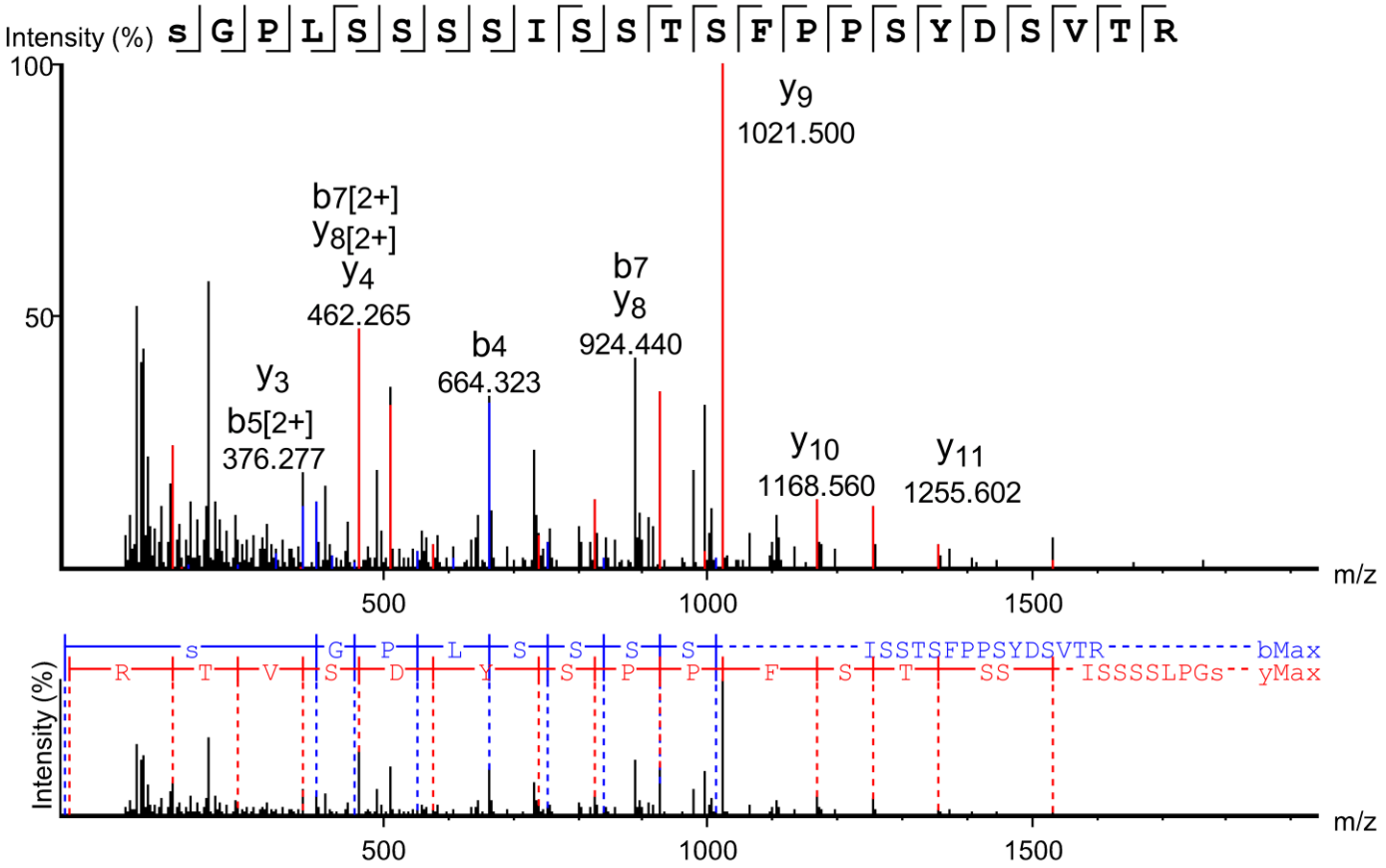

Table 2 - Figure Supplement 1.

Scan 67492, m/z=885.7529, z=3, -10lgP=56.87, ppm=2.1 (pS1969)

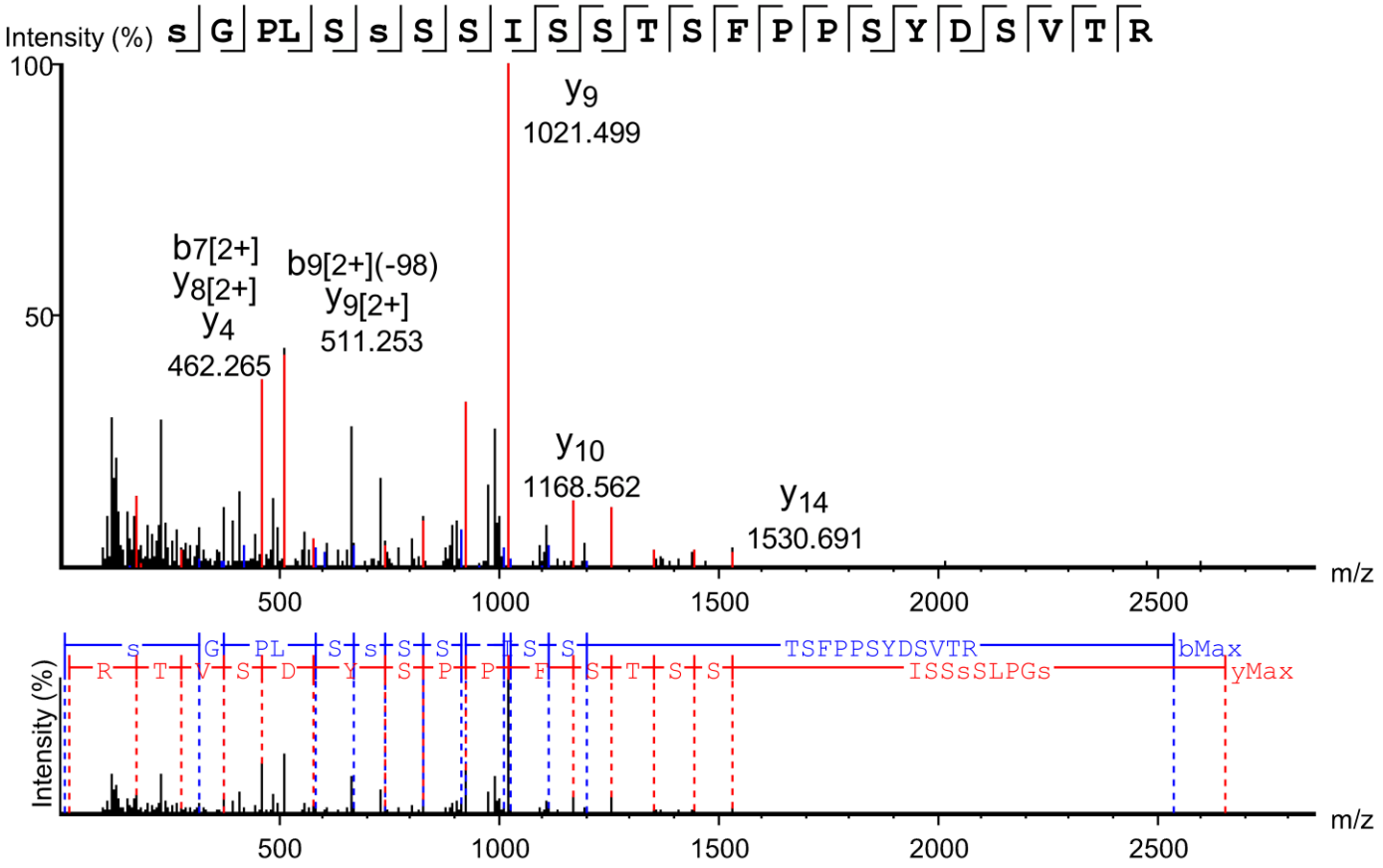

Table 2 - Figure Supplement 1.

Scan 49853, m/z=937.7873, z=3, -10lgP=48.49, ppm=2.7 (pS1971)

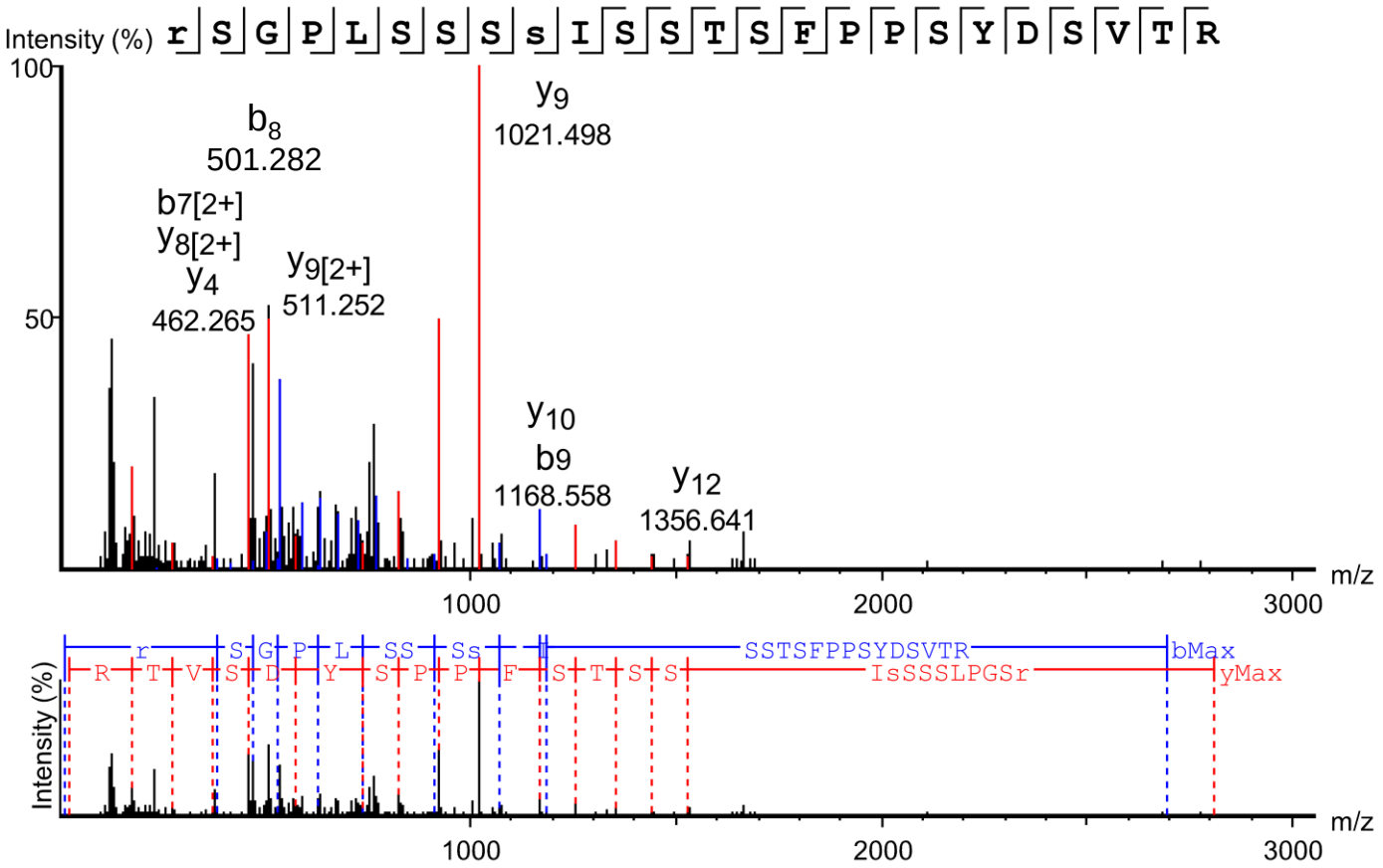

Table 2 - Figure Supplement 1.

Scan 64573, m/z=885.7498, z=3, -10lgP=61.75, ppm=-1.4 (pS1973)

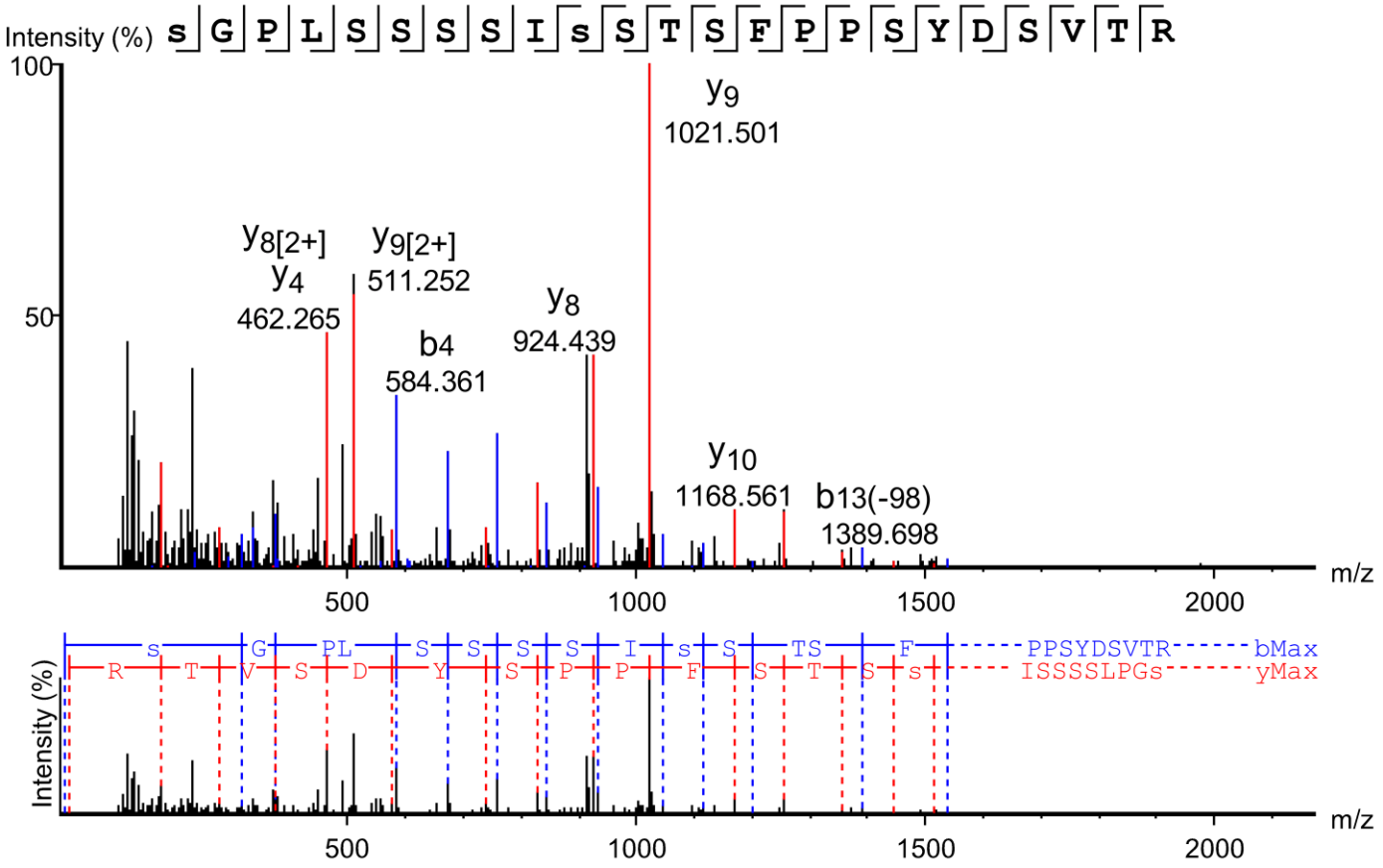

Table 2 - Figure Supplement 1.

Scan 64993, m/z=885.7498, z=3, -10lgP=61.81, ppm=-1.5 (pS1974)

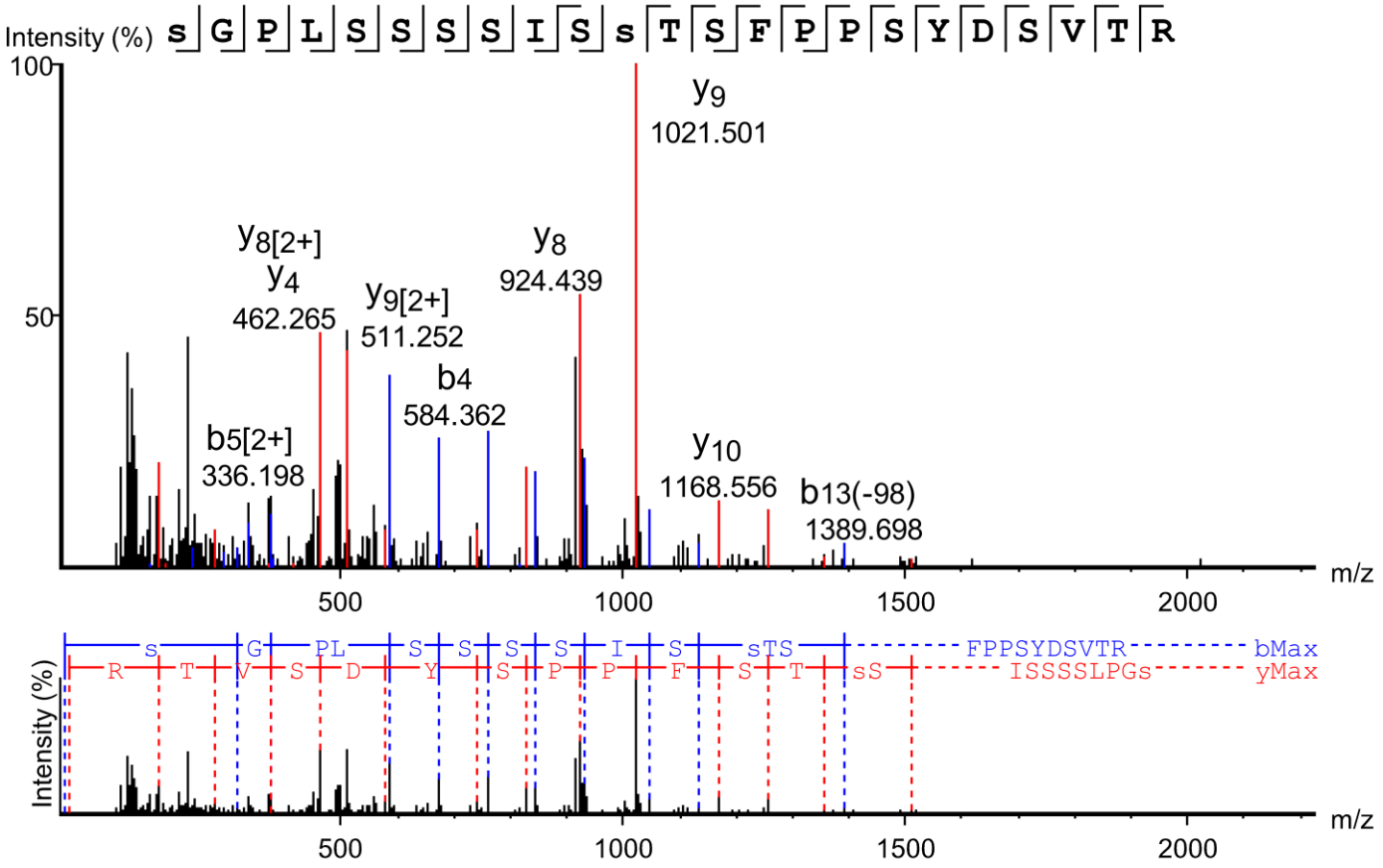

Table 2 - Figure Supplement 1.

Scan 31030, m/z=641.3244, z=2, -10lgP=37.66, ppm=1.1 (pS1989)

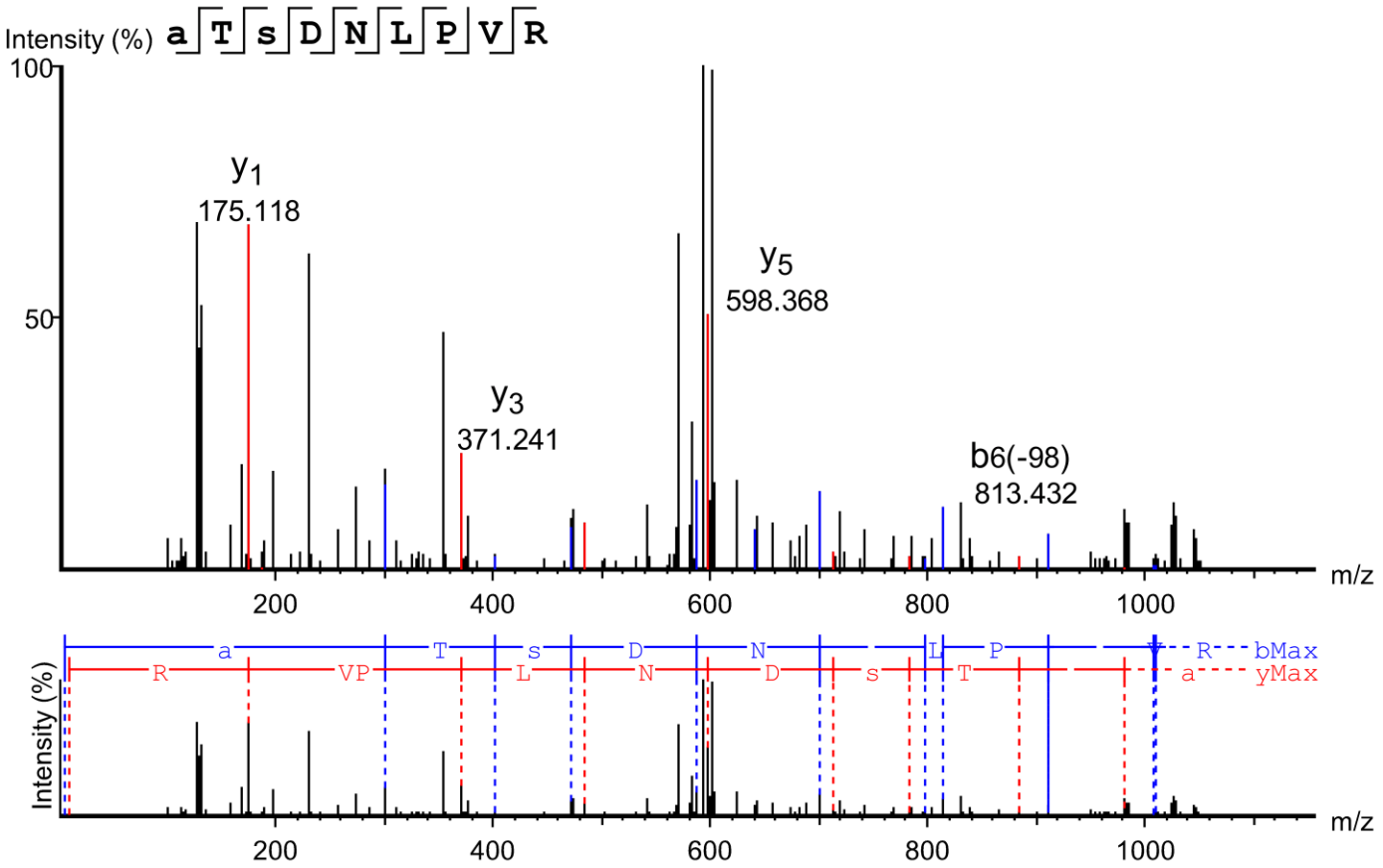

Table 2 - Figure Supplement 1.

Scan 41663, m/z=675.9753, z=3, -10lgP=38.78, ppm=-0.1 (pS2011)

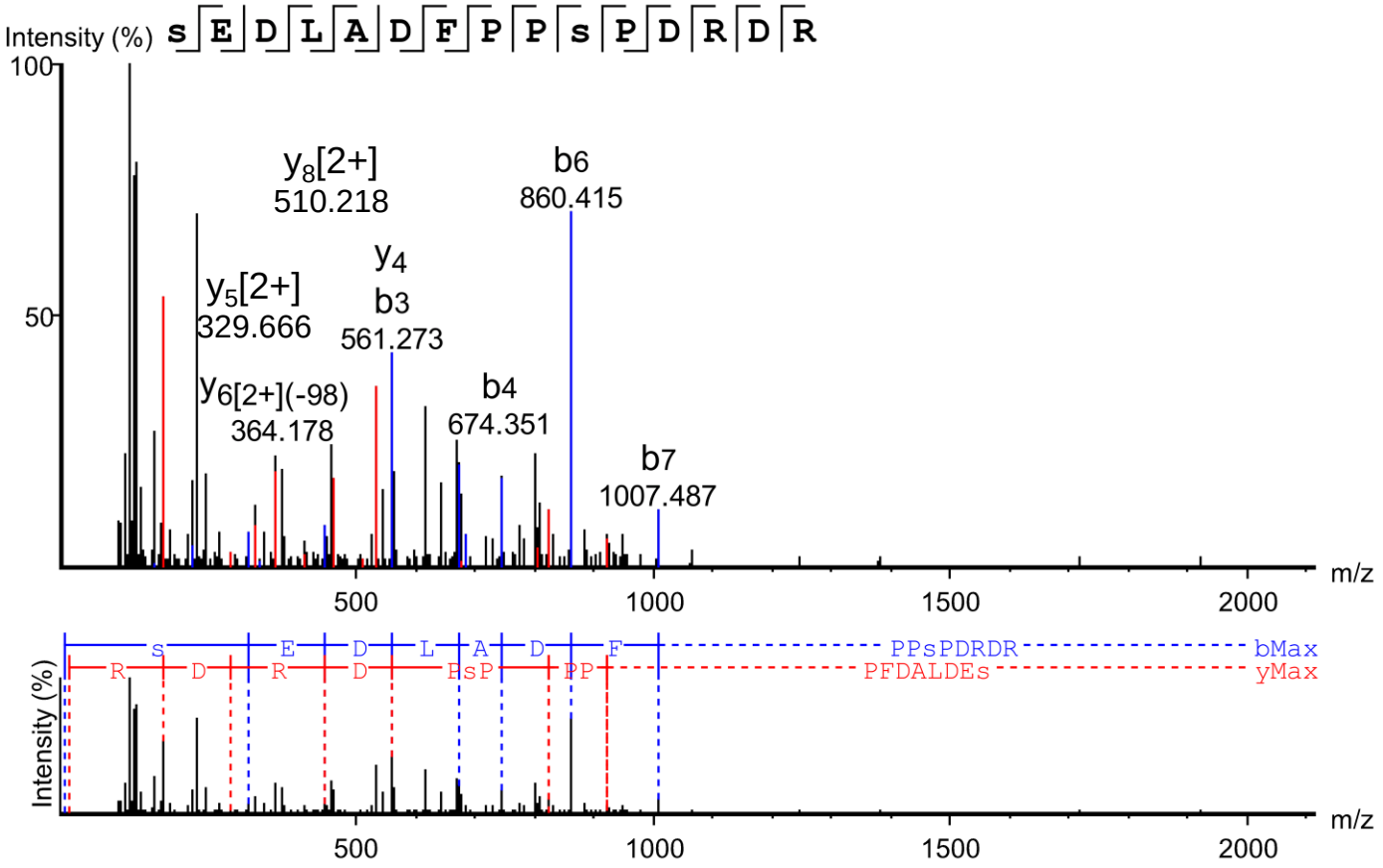

Table 2 - Figure Supplement 1.

Scan 75683, m/z=861.8894, z=4, -10lgP=48.05, ppm=3.0 ($Na_V1.4$; pS522 + pS525)

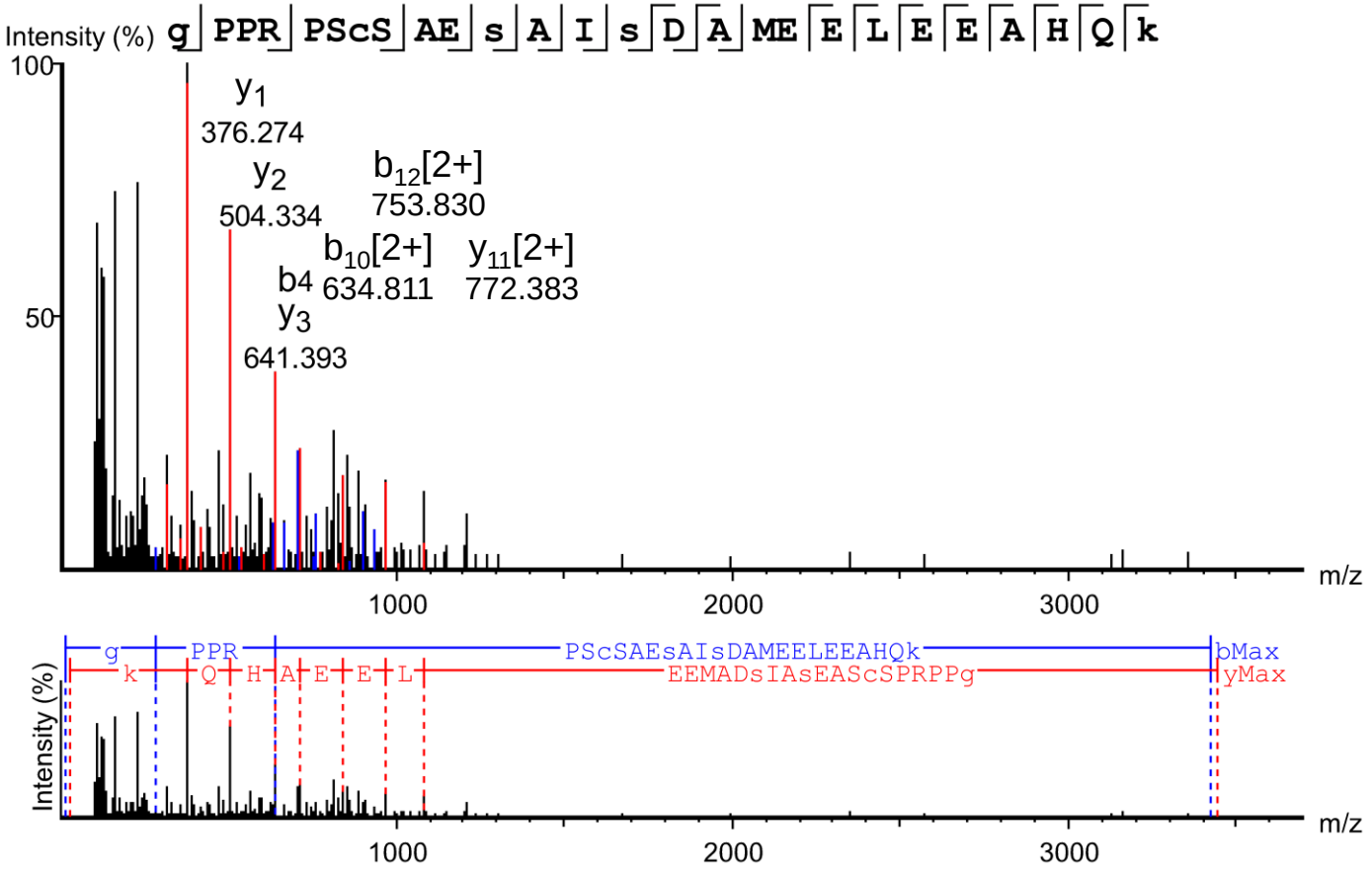

Table 2 - Figure Supplement 1.

Scan 64345, m/z=841.8929, z=4, -10lgP=60.31, ppm=-2.8 ($Na_V1.4$; pS525)

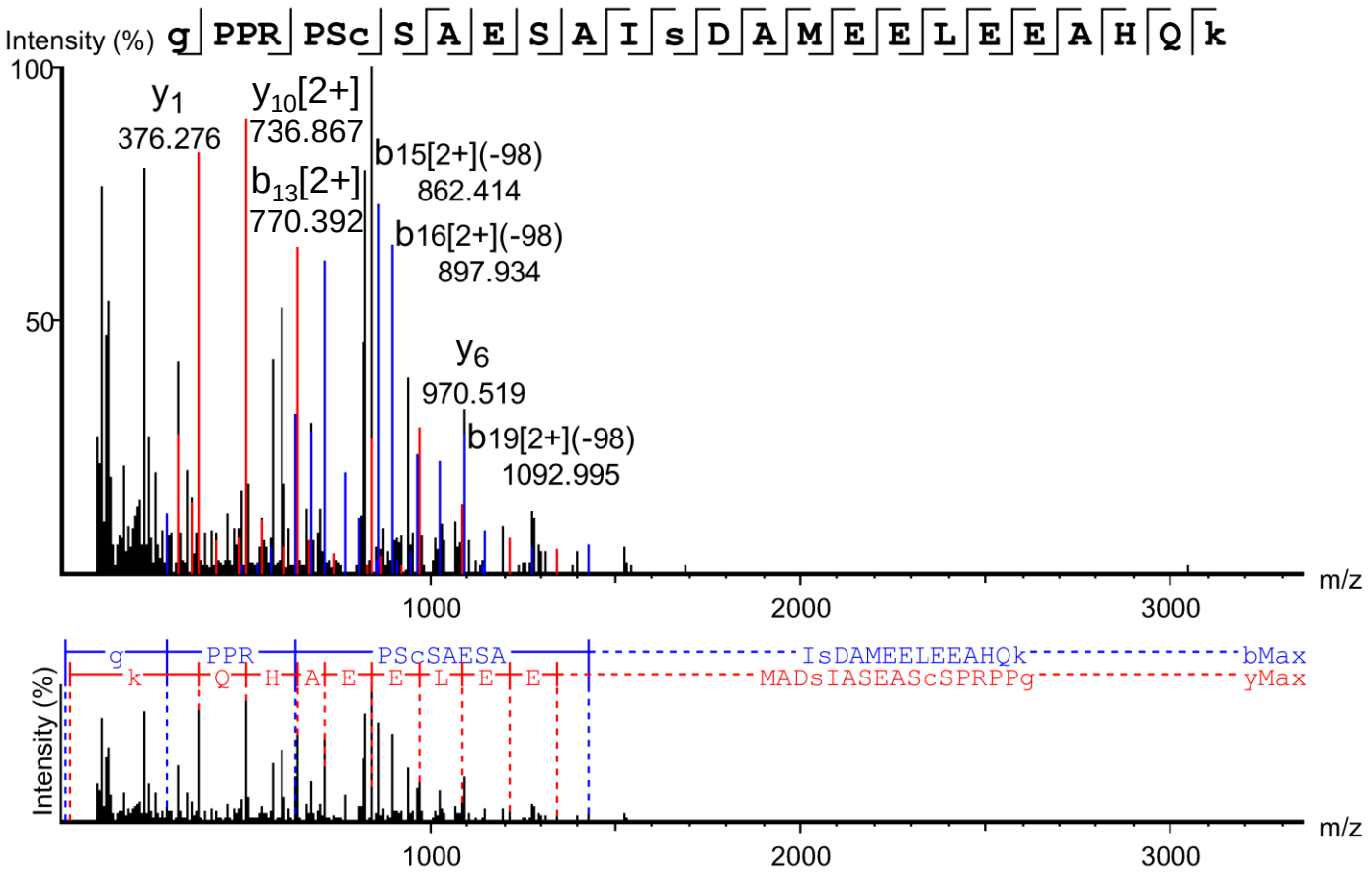

Table 2 - Figure Supplement 1.

Scan 91385, m/z=1486.9480, z=4, -10lgP=54.20, ppm=1.1 ($Na_V1.4$; pS900)

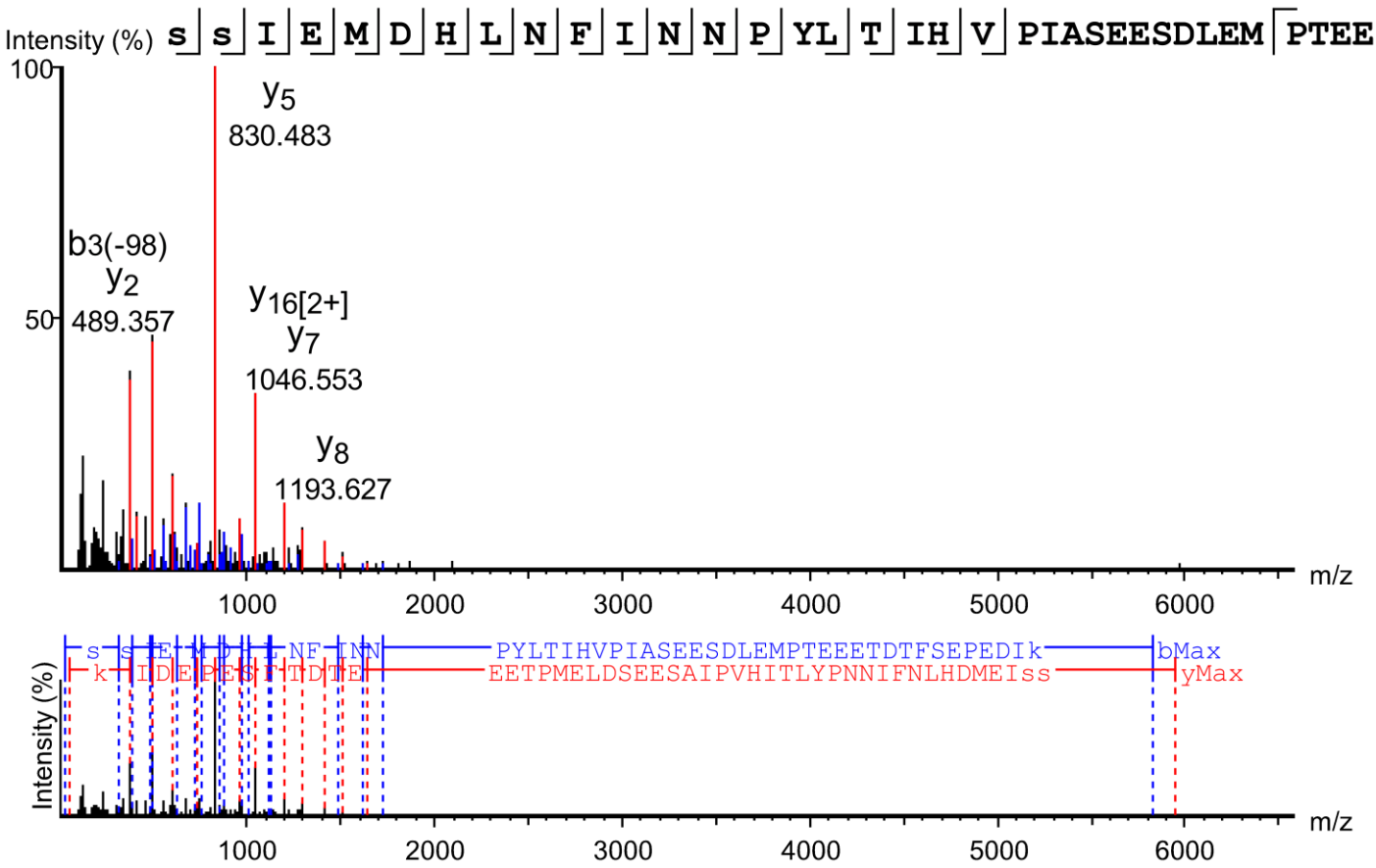

Table 2 - Figure Supplement 1.

Scan 49121, m/z=927.4735, z=6, -10lgP=52.01, ppm=1.1 ($Na_V1.4$; pS1819)

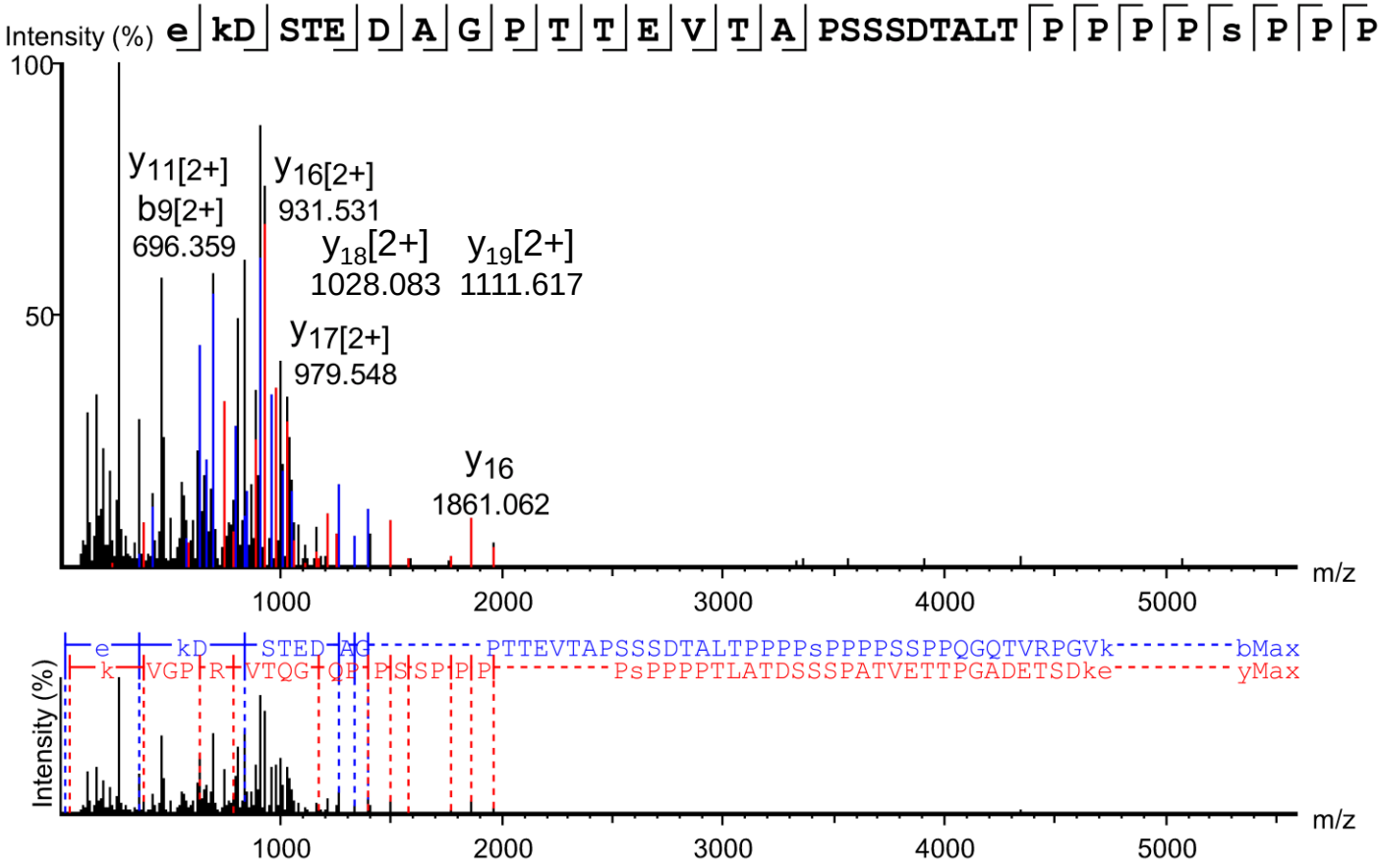

Table 2 - Figure Supplement 1.

Scan 99924, m/z=817.3834, z=3, -10lgP=63.96, ppm=-1.6 ($Na_V1.3$; pS658)

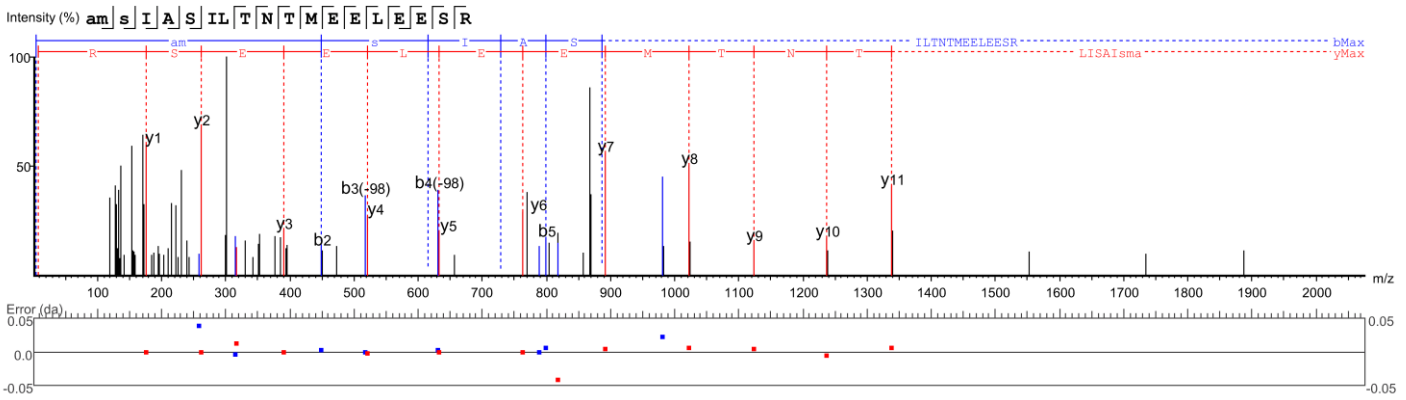

Table 2 - Figure Supplement 1.